Direct Contact Membrane Distillation:

Analysis and application

Ho Yan Wu

St. Anne’s College

A thesis submitted for the degree of *Doctor of Philosophy*

Department of Engineering Science, University of Oxford

Trinity Term 2015

Direct Contact Membrane Distillation: Analysis and application

Ho Yan Wu, St. Anne's College, Trinity Term 2015

A thesis submitted for the degree of Doctor of Philosophy at the University of Oxford

Abstract

This work investigates different aspects of direct contact membrane distillation (DCMD), from a microscopic study of membrane structure of an electrospun membrane and mass transfer mechanism across DCMD membranes, to the macroscopic picture of DCMD's design and technological viability in small-scale, localized desalination for the use in arid regions with a supply of brackish water.

Experiments were carried out to investigate the effect of membrane thickness upon transmembrane flux in DCMD. Polyvinylidene fluoride (PVDF) electrospun nanofibrous membranes (ENMs), consolidated with a heatpress process, as thin as 27 microns were fabricated and tested in a DCMD cell. A transmembrane flux as high as 60 L/h m^2 was observed. A structural deviation factor considering tortuosity, which reflected the variation of structure with thickness, was introduced. The model was found to fit the data very well except for the thinner membranes operated in a system with high inlet feed temperature. Additionally an analytical model was created to estimate the optimal membrane thickness for DCMD operations. It is found that the value of optimal thickness increases with reduced heat transfer coefficients; decreased feed inlet temperature; increased membrane permeability; and increased salinity. Even for 10% NaCl the predicted optimum was 11 microns which was too thin for experimental confirmation.

Two approaches were taken to the sizing of DCMD modules. A modified effectiveness – number of heat transfer units (E-NTU) method is introduced for designing uniform flow modules. The model enables good estimation, which is within 6%. The E-

NTU method is recommended for preliminary design for larger systems. A discretization model of a DCMD hollow fibre module with random packing was constructed using MATLAB. The influence on module performance of various design features, including flow configuration, fibre size, packing density and were evaluated. Four performance indicators were used to assess the performance: transmembrane flux, module production rate, thermal efficiency and overall energy efficiency. The assessments suggest a module with a packing density of about 0.5 offers the best thermal and energy efficiency. Whilst smaller diameter fibres create a moderately higher pressure drop, the extra membrane area packed into the module enhances the production rate. Moreover although transmembrane flux always decreases with a longer module, the overall module production rate justifies a bigger module in a practical desalination system. Prior to DCMD module design consideration, a reassessment of the conventional method suggested that the sum of resistance approach engages in some double counting when combining the Knudsen diffusion coefficient and the molecular diffusion coefficient. A new expression which accounts for the physical influence between molecular-molecular interactions and Knudsen diffusion is introduced.

This thesis concludes with a flowsheet design of a DCMD desalination system that can provide 500L of potable water per day, which is sufficient for a large family living in a remote arid region. The results from the MATLAB model were incorporated into the Aspen Plus using both direct and indirect methods. Considerations were given to the recycle and cooling streams and a design which avoided the need for refrigeration was found.

I dedicate this piece of work to:

My parents,

who love and support me through everything so far;

my paternal grandparents in Heaven,

who loved and spoiled me to bits,

for I am the best and only grandchild they were blessed with.

Acknowledgements

This could easily take up the space of a whole chapter. I am keeping this short so that those who are shortlisted would feel more special.

First and foremost, thanks be to God who has blessed me with all the amazing things and people in my life, the opportunity to work on such a meaningful D.Phil, and the amazing time I have spent in my favourite city.

Without my supervisor Professor Robert W. Field, my D.Phil would not have happened. I would probably be working as an environmental or engineering consultant somewhere in East Asia, staying away from a Dr. title. He introduced me to membrane technologies and to this project. I cannot be more grateful and thankful for his massive help, support, patience and kind encouragements throughout the past 3.5 yr.

I would like to acknowledge various funding bodies: NUS environmental Research Institute, Singapore Peking Oxford Research Enterprise (SPORE) for the PhD scholarship; St Anne's College and European Membrane Society for numerous travel awards to attend conferences; and most importantly, my supportive parents who have showered me with endless love and prayers ever since Day -250 in my life, and who still help me to make ends meet when I spend on silly things.

I would also like to express my gratitude to Professor Rong Wang from Singapore Membrane Technology Centre and students in her research group, especially Liao Yuan, Tian Miao, Guizi and Chun Heng. Professor Wang has welcomed me to her research group which enabled me to carry out the experiments with the best available equipment.

Many thanks to all my dear friends and officemates for being there when I was annoyed with the progress of my work. To name a dozen: Agnes for the maths support

and always cheering me up with lame things and promised meals; Lina, Rachelle and Yester for the constant reminder that I need to finish soon to join the real world; Aggie and Jocky for the great company and making me feel young when friends from undergraduates have deserted me in Oxford; Fengbin and Deborah without whom my time in Singapore would be unbearable; Mairin and Karoline for welcoming me to their homes for Christmas; Kenny for friendship, mentorship, encouragements and for proofreading my thesis; Richard for the countless MATLAB advices and debugging; officemates including Elias, Tamara, Julian, Ping, Fozia, Farrukh, Xiafu, Jiji, Kat, Shiv and Jessie for putting up with the eyesore of my slightly less-organised desk; and my lovely housemates over these 3.5 years: Erika, Emily, Jan, Lakshmi, Anna, Sarah, Jean, Tolis and Kizzy for chats and fun, and for sometimes feeding me.

Finally, a special thank you to those who prayed for me: Derek, Chilam, Pui Pui, friends from St Ebbe’s Church, Trinity Christian Centre (Singapore) and OCCCSF and all the aunties in my mum’s fellowship group.

Table of Contents

Abbreviations

AGMD	Air gap membrane distillation
ASM	Algorithmic state machine
DCMD	Direct contact membrane distillation
DGM	Dusty gas model
ED	Electrodialysis
E-NTU	Effectiveness-number of heat transfer units
HFM	Hollow fibre module
IPA	Isopropyl alcohol
LEP	Liquid entry pressure
MD	Membrane distillation
MED	Multiple-effect distillation
MSF	Multi-stage flash
NF	Nanofiltration
PE	Polyethylene
PEI	Polyetherimide
PES	Polyethersulfone
PP	Polypropylene
PS	Polysulfone
PTFE	Polytetra-fluoroethylene

PVDF	Polyvinylidene fluoride
RO	Reverse osmosis
SGMD	Sweeping gas membrane distillation
TPC	Temperature polarization coefficient
VBA	Visual Basic Application
VMD	Vacuum membrane distillation

Nomenclature

Symbol	Meaning	Units
A	Area	m^2
C	Heat capacity rate	$J\ K^{-1}s^{-1}$
C_r	Heat capacity ratio	-
D	Diffusion coefficient	$m^2\ s^{-1}$
$D_{w.a}^{P_T}$	Diffusion coefficients for ordinary diffusion of water vapour in air	$m^2\ s^{-1}$
$D_{w.a}^{act}$	Actual diffusion coefficients for ordinary diffusion of water vapour in air, introduced in Eq. 4-4	$m^2\ s^{-1}$
E	Effectiveness	-
E^T	Total energy	J
G	Gap of the channel	M
H	Heat transfer coefficient defined in Eq. 2-8	$Wm^{-2}K^{-1}$
L	Length	M
K*	Membrane coefficient	$kg\ m^{-2}\ s^{-1}Pa^{-1}$
K"	Membrane permeability	$kg\ m^{-2}s^{-1}\ K^{-1}$
N	Mass flux across membrane	$kg\ m^{-2}\ s^{-1}$
N_f	Number of fibre	-
P	Saturated vapour pressure	Pa
P^0	Saturated vapour pressure of pure compound	Pa

Pr	Prandtl number	-
P_T	Total pressure	Pa
Q	Overall heat transfer	W
Re	Reynolds number	-
T	Temperature	K
U	Overall hear transfer coefficient	W $m^{-2}K^{-1}$
U_L	Heat transfer coefficient, Eq. (A2)	W $m^{-2}K^{-1}$
a	Polygonal cell cross-section area	mm^2
a_0	Average polygonal cell cross-section area	mm^2
a_f	Hollow fibre cross-section area	mm^2
b	Ratio of permeate to feed heat transfer coefficient	-
$\bar{c}$	Mean speed of gas molecule	m s^{-1}
c	Specific heat capacity	J $kg^{-1}K^{-1}$
d	Diameter	m
f	Frication factor	-
h	Heat transfer coefficient	$Wm^{-2}K^{-1}$
k	Thermal conductivity	W $m^{-1}K^{-1}$
m	Mass	kg
$\dot{m}$	Mass flowrate	kg s^{-1}

n	Number of molecules per cubic meter	-
p	Pressure	Pa
q	Heat flux	W m^{-2}
r	Radius of pore	m
u	Velocity	ms^{-1}
w	Weight	kg
y	Local mole fraction	-
α	Overall heat transfer coefficient for DCMD	W $m^{-2}K^{-1}$
$\alpha_{\mathrm{Essalhi}}$	Used in Eq. 2-20, contribution of Knudsen diffusion to mass transfer	-
α_w	Water activity	-
β	Contact angel	^{o}
ε	Porosity	-
ρ	Density	kg m^{-3}
σ^2	Molecular cross section as described in Eq. 3-1	m^2
δ	Membrane thickness	M
Λ	Mean free path of vapour	M
λ	Heat of vaporization	J kg^{-1}
$\eta_.$	Thermal efficiency	-
$\eta_{mod.}$	Module thermal efficiency	-

γ	Surface tension of the liquid	N
τ	Tortuosity	-
ϕ	Packing fraction	-
ξ	Correction factor	-
ж	Constant used in Section 4.4.4	-

Subscripts

a	Air
avg	Average value
b	Bulk
c	Cold fluid side
dry	At dry condition
e	Energy
ele	Element/ elemental
Essalhi	Used in Eq. 2-20, refer to parameters introduced in Essalhi et al. 2013
D	Molecular diffusion
f	Feed side
fi	fibre
fm	fluid flow adjacent to the membrane in the feed channel
g	gas
h	Hot fluid side

i	The i th component
j	The j th element
in	Condition at inlet of membrane module
K	Knudsen
m	Membrane or adjacent to membrane
max	Maximum value
min	Minimum value
mp	Membrane polymer
out	Condition at the outlet of membrane module
opt	Optimal
P	Poiseuille
p	Permeate side
pm	fluid flow adjacent to the membrane in the permeate channel
theor.	Theoretical
w	Water
wet	At wetted condition

1. Introduction

This thesis presents a study on the analysis and applications of direct contact membrane distillation (DCMD). While experimental work is included, an emphasis is rested on the modelling and design of membrane distillation (MD) membrane module and systems. This chapter highlights the motivation and some background behind the study. An outline of this thesis is provided at the end of this chapter.

1.1. Background

Inadequate supply and access to potable water is one of the biggest challenges worldwide. Due to climate change, erratic rainfall and increase in global populations, shortage of potable water threatens more and more nations, including both developed and developing countries. It is predicted that by 2025, two-thirds of the world would experience water shortages (Karagiannis & Soldatos, 2008). While approximately 70% of the earth's surface is covered by water, only 3% is fresh water with the rest being salt water (Kalogirou, 2005). Desalination becomes the obvious hope and solution to the problem of water shortage. Potable water should contain less than 0.5 g of salt per litre; while by conventional definition brackish water contains between 0.5 to 30g of salt per litre and saline water contains 30-50g. Any higher concentration is referred as brine.

The world's first land-based desalination plant was a multiple-effect distillation (MED) plant that was installed in Antilles, Netherlands in 1928. It had a capacity of $60m^3day^{-1}$ (Mulvaney & Robbins, 2011). Since then technologies have developed rapidly with large desalination plants using MED, multi-stage flash (MSF) and reverse osmosis (RO) have demonstrated success both technically and economically. Places with high risk of drought like Florida and Saudi Arabia have been relying on desalination to provide fresh water for decades (Ayoub & Alward, 1996). More than three millions cubic meters of potable water is produced by desalination plants in Saudi Arabia each day (which amounts to more than 70 percent of the water used in cities) (Royal Embassay of Saudi Arabia, 2015) and in Abu Dhabi Emirate, about a million cubic meters of fresh water is produced by desalination daily (Sultan, 2010).

According to International Desalination Association (IDA, 2014) in 2013, there are more than 17,000 desalination plants worldwide, treating more than 80 million cubic meters of water daily. Figure 1-1 shows the distribution of total world installed desalination capacity by technology. RO and MSF combine to form 86% of the overall capacity, electrodialysis (ED), nanofiltration (NF) and other technologies add up to less than 10% in total.

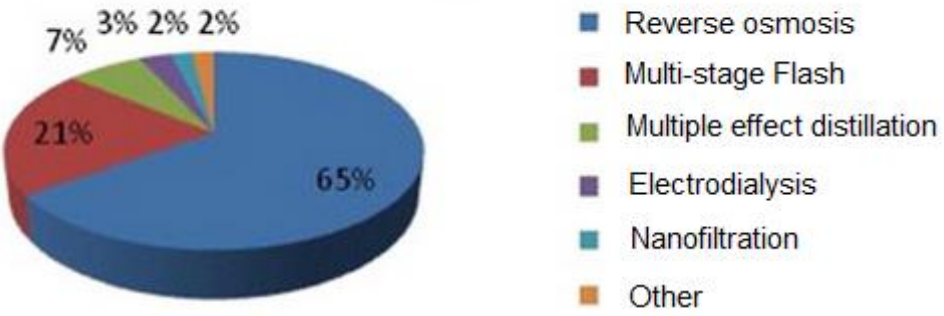

Figure 1-1 Desalination capacity installed by technology (Burn, et al., 2015)

In contrast to developed areas, people living in developing, remote and arid regions often suffer from lack of potable water due to inadequate rain and/or poor water distribution systems (Ayoub & Alward, 1996). In 2006 it was recorded that 84% of the population without access to an improved source of drinking water lived in rural areas (WHO/UNICEF, 2006) and in 2015, it is still estimated that 90% of those relying on untreated surface water live in rural areas (WHO/UNICEF, 2014). Urgent development and establishment of small scale, decentralized, sustainable desalination systems are necessary for inland brackish water treatment.

1.2. Conventional desalination technologies

Conventionally, desalination is performed via an evaporation process (MSF and MED) or a membrane separation process (RO, ED and NF). In both MSF and MED processes, hot saline/brackish water passes and evaporates through serial stages with decreasing temperature or pressure, respectively. Although small or medium scale systems have been considered (Suri, et al., 1989; Sadhukhan & Tewari, n.d.), MSF and MED are commonly used for large-scale desalination for their efficiencies increase with size and the number of effects or stages. The typical capacities of these plants range from 100,000 to almost 1,000,000 m^3 day^{-1} (Govindan, 2012).

Membrane systems are more suitable for smaller-scale desalination due to scalability. RO systems are found ranging from a few litres to thousands of cubic meter per day. Remote RO systems can be coupled with solar photovoltaic panels and/or wind power with battery system for operations (Mokheimer, et al., 2013). The main disadvantages of RO are the high maintenance cost and the need for pretreatment (Al-Karaghouli & Kazmerski, 2012). Thus depending on the situation, although competitive and well-established, RO might not be the best option for remote areas especially when there are potential issues with accessibility to materials and skilled labour. ED is notably less popular and versatile compared to RO, and is often only used to desalinate brackish water due to the electricity demand, which increases rapidly with salinity. Pretreatment is also often required in ED processes.

1.3. Membrane distillation – Principle and common configurations

The working principle in membrane distillation (MD) combines evaporation and membrane separation technologies. The two components which are essential to MD processes are the driving force - the transmembrane vapour pressure difference between the feed and permeate; and a porous hydrophobic membrane that only allows vapour to pass through. Typically, the vapour pressure difference is induced by a temperature difference, and in the case of vacuum membrane distillation, a physical pressure gradient is also applied. There are four commonly acknowledged MD configurations, namely, direct contact membrane distillation (DCMD), air-gap membrane distillation (AGMD), vacuum membrane distillation (VMD) and sweeping gas membrane distillation (SGMD). They are differentiated by the media adjacent to the permeate side of the membrane as depicted in Figure 1-2.

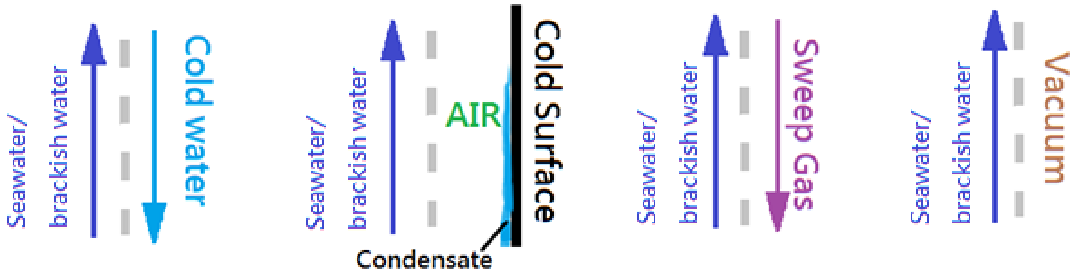

Figure 1-2 Schematics of the four main MD configurations, from left, DCMD, AGMD, SGMD and VMD.

With the simplest design, the main disadvantage of DCMD is the relatively high conductive heat loss due to the direct contact between both fluids and the membrane (Zaragoza, et al., 2014). Compared to DCMD, the heat loss is reduced in AGMD but the stagnant air increases the mass transfer resistance which the transmembrane mass flux is then limited by diffusion across the air gap and evaporation through the pores (Susanto, 2011; Summers, 2013). As a result the permeate flux of AGMD is significantly less than that of DCMD (Selvi & Baskaran, 2014). In VMD, a low pressure or vacuum is applied on the permeate side for a higher permeate flux (Mericq, et al., 2009). Yet this sometimes gives rise to a more severe problem of membrane wetting compared to other configurations (Abu-Zeid , et al., 2015). An external condenser is required to collect the permeate in SGMD which is undesirable due to additional complexity and contributes to extra expense. Heat recovery is also difficult in this configuration (Khayet & Matsuura, 2011).

While each configuration has its merits and disadvantages, with the simplest design, a higher permeate flux compared to AGMD, less aggressive membrane wetting compared to VMD and without the complication of a condenser compared to SGMD, DCMD is considered the preferred configuration for rural application. Thus this thesis concentrates on the study of DCMD.

1.4. Advantages and challenges for MD and research objectives

Ahtough the concept of MD had already been known in the 60s (Lawson & Lloyd, 1996), the interest and research activity in MD only started to boom since the 90s due to progress in membrane fabrications (Figure 1-3).

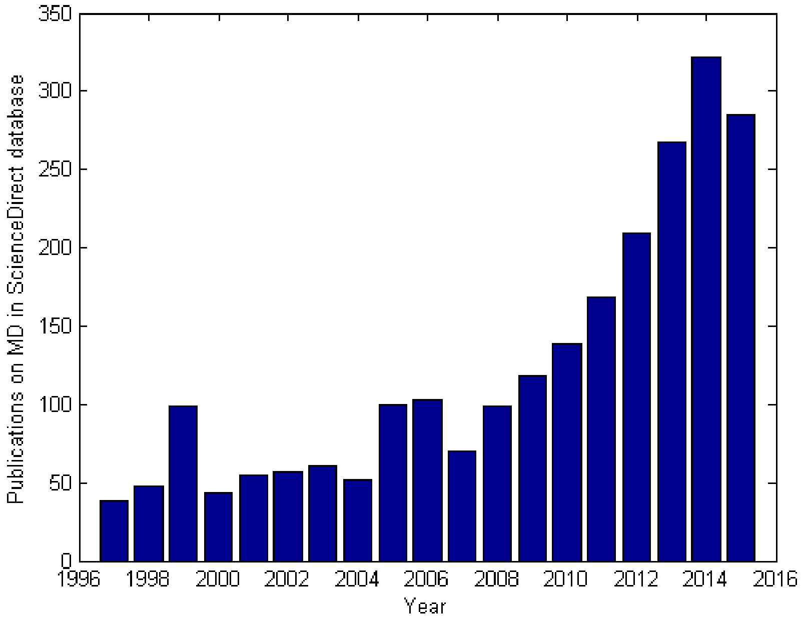

Figure 1-3 MD research activities (publications) from the 90s (ScienceDirect, 2015)

MD has attracted attention because of its many advantages, including (Lawson & Lloryd, 1997):

(a) 100% theoretical rejection of ions or other involatile molecules;

(b) Relatively low operating temperature;

(c) Ambient or relatively low operating pressure;

(d) Reduced or elimination of any chemical interaction.

Moreover, due to the increase in global awareness of sustainable developments in both energy and water supply, renewable energy-desalination coupled systems have attracted a lot of attention (García-Rodríguez, 2003; Mathioulakis, et al., 2007; Ghaffour, et al., 2015), which makes MD even more appealing due to its potential to be directly integrated with solar thermal energy (Tomaszewska, 2000; Banat, et al., 2002; Koschikowski, et al., 2003; Tzen, et al., 2012; Mahmoud , et al., 2013; Ghaffour, et al., 2015; Banat, et al., 2007; Hogan, et al., 1991).

In spite of MD’s good desalination potential and advantages over other technologies, it is still yet to receive much industry acceptance due to its relatively low flux (Qtaishat & Banat, 2013; Zhu & Liu, 2000). In view of this fact and the urgent need of development in small scale desalination systems, this work aims to make positive contributions in optimising MD membranes, modules and process designs. The emphasis is on thorough investigations into various aspects of direct contact membrane distillation (DCMD), which could be suitable for localised desalination of brackish water in arid regions.

1.5. Thesis outlines

This thesis includes 7 chapters, which are highlighted as following:

Chapter 1: Introduction and background - Introduction and motivation of the work presented in this thesis

Chapter 2: Literature survey – A brief literature review, which focuses on:

- Various models of DCMD mass transfer mechanisms;
- Various DCMD performance related factors including membrane properties and module design; and
- Computer-aided simulation of MD modules and systems.

Chapter 3: Investigation of the effect of membrane thickness upon transmembrane flux – Experimental and analytical study of the effect of membrane thickness and optimal membrane thickness. Experiments were carried out with electrospun nanofibrous membranes and results were compared with analytical solutions.

Chapter 4: Modelling of the direct contact membrane distillation process – A re-examination and refinement of the common use of dusty gas model for DCMD is followed by the derivation and validation of a modified effectiveness- number of heat transfer units model for use in DCMD design.

Chapter 5: Influence of design on performance of countercurrent hollow fibre DCMD module – Using a validated MATLAB[1] DCMD hollow fibre module (HFM) model, the impact on module performance due to flow configuration. module packing density, length and fibre size is evaluated.

Chapter 6: Implementation of DCMD in rural arid regions requiring desalination – A process flowsheet is proposed for the application of DCMD in arid regions. The flowsheet is simulated using Aspen Plus and the system deliver 500L of potable per day, which is sufficient for a family's daily consumption.

Chapter 7: Concluding remarks – Recommendations for future work are also included in this chapter.

---

[1] MATLAB – a numerical computing environment provided MathWorks Inc.

2. Literature Survey

The chapter presents a review on various aspects in MD development, including mathematical modelling of the heat and mass transfer across the membrane and the various factors affecting DCMD performance. MD module types and computer-aided simulation on MD process are also discussed.

2.1. Heat and mass transfer in DCMD

2.1.1. Heat transfer

Heat and mass transfer occurs simultaneously in MD operation as illustrated in Figure 2-1. Within the fluid channel, heat is transferred between the bulk fluid to the membrane surface via convection. Across the membrane, heat transfer takes place in two forms: conduction principally across the solid membrane materials and convection due to the permeate flux conveying heat. Apart from the porous contact surface, MD units are highly similar to heat exchanger units. Hence the commonly used heat transfer model for the thermal balance in DCMD is based on the correlations originally derived for heat transfer through non-porous contact surfaces; with an additional term accounting for the heat carried by the vapour permeate from feed to permeate.

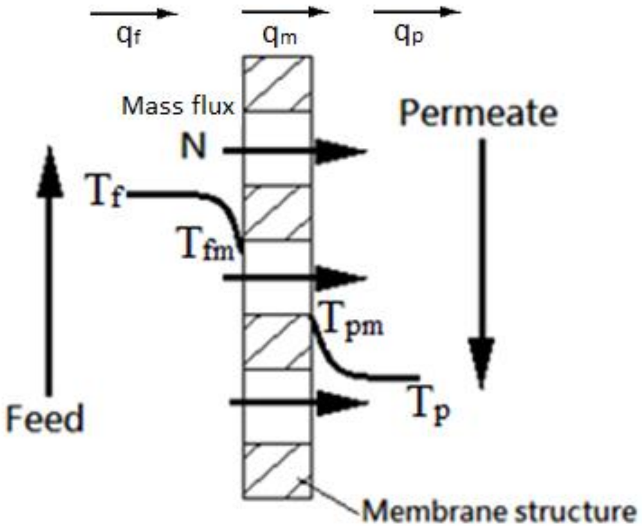

Figure 2-1 Schematic illustration of the heat transfer processes across membrane

The governing equations of heat transfer across the membrane of DCMD are:

$$q_f = h_f(T_f - T_{fm}) \qquad \text{Eq. 2-1}$$

$$q_p = h_p(T_{pm} - T_p) \qquad \text{Eq. 2-2}$$

$$q_m = N\lambda + \frac{k_m}{\delta}(T_{fm} - T_{pm}) \qquad \text{Eq. 2-3}$$

where q is the heat flux, h is the heat transfer coefficient, T is the temperature, δ is the membrane thickness, N is the transmembrane flux and λ is the latent heat of vaporization. The subscripts is noted in nomenclature and shown in Figure 2-1, which f and p denote the bulk flow of feed and permeate and fm and pm denote the fluid flow adjacent to the membrane in the feed and permeate channel respectively. The thermal conductivity of the membrane, k_m , is given by:

$$k_m = \varepsilon k_g + (1 - \varepsilon)k_{mp} \qquad \text{Eq. 2-4}$$

where ε is the porosity of the membrane, k_{mp} is the thermal conductivity of the material (i.e. the membrane polymer) and k_g is the thermal conductivity of the gas present.

In steady state, the three thermal fluxes are the same, yielding:

$$q_f = q_p = q_m \qquad \text{Eq. 2-5}$$

2.1.2. Temperature polarization

Temperature polarization in MD, depicted in Figure 2-1 refers to the difference between the actual temperature difference across the membrane and the temperature difference between the bulk fluids. Schofield et. al (Schofield, et al., 1987) introduced the term temperature polarization coefficient (TPC) which quantifies the level of temperature polarization and is expressed as:

$$TPC = \frac{(T_{fm} - T_{pm})}{(T_f - T_p)} \qquad \text{Eq. 2-6}$$

which can be then be rewritten as (Schofield, et al., 1987):

$$TPC = \left(1 + \frac{H}{h_f} + \frac{H}{h_p}\right)^{-1} \qquad \text{Eq. 2-7}$$

for

$$H = \frac{q_m}{(T_{fm} - T_{pm})} \qquad \text{Eq. 2-8}$$

While temperature polarization plays an important part in MD system (Macedonio, et al., 2013), concentration polarization is negligible in desalination of brackish water (Martínez-Díez & Vázquez-González , 1999) due to the low NaCl concentration, the activity coefficient of the feed remaining close to unity (Kitic, et al., 1986) (see Eq. 2-13).

More commonly, thermal efficiency, η, is used to assess the amount of useful heat in a MD system. η is given as:

$$\eta = \frac{N\lambda}{q_f} \qquad \text{Eq. 2-9}$$

where q_f is often evaluated using:

$$q_f = \frac{c_f(T_{f,in} - T_{f,out})}{A_m} \qquad \text{Eq. 2-10}$$

where c denotes the specific heat capacity, $T_{f,in}$ and $T_{f,out}$ denote the feed inlet and outlet temperature respectively and A_m is the membrane area.

2.1.3. Mass transfer

Conventionally, the permeate flux in DCMD is expressed as:

$$N = K^*\left(P_{fm} - P_{pm}\right) \qquad \text{Eq. 2-11}$$

where P is the partial pressure of water vapour of the fluids (in Pa) and K* is the membrane coefficient (in kg m^{-2} s^{-1} Pa^{-1}). The latter, K*, depends on the diffusivity of the water vapour and on membrane properties.

For pure water, the relationship between water vapour pressure and temperature is given by Antoine equation (Sugiyama, et al., 2012):

$$P_w^0 = \exp\left(23.20 - \frac{3816.44}{T - 46.13}\right) \qquad \text{Eq. 2-12}$$

where T is the absolute temperature (in K).

For aqueous solutions like seawater, the vapour partial pressure is given by:

$$P_w = \alpha_w P_w^0 \qquad \text{Eq. 2-13}$$

where $\alpha_w$is the activity coefficient of water at that concentration.

2.1.4. Modelling DCMD mass transfer mechanisms using dusty gas model

Various mathematical models have been developed to describe the mass transfer in DCMD. Depending on the research objectives, majority of MD modelling studies apply an one-dimensional (1-D) model for mass transfer across the membrane. Dusty gas model (DGM) (Mason & Malinauskas, 1983), depicted in Figure 2-2, has been particularly popular among researchers (Lawson & Lloyd, 1996; Fernández-Pineda, et al., 2002; Jensen, et al., 2011; Izquierdo-Gila, et al., 2008). DGM combines Knudsen diffusion, Poiseuille flow and molecular diffusion to model K^* (in Eq. 2-11) but as noted in (Field, et al., 2013) it is a erroneous to consider that Knudsen diffusion/flow is present at the same time as viscous flow. As discussed later in Chapter 4 of this thesis, one should not consider that there is simply additivity of a 'Knudsen' resistance and an 'Ordinary diffusion' resistance.

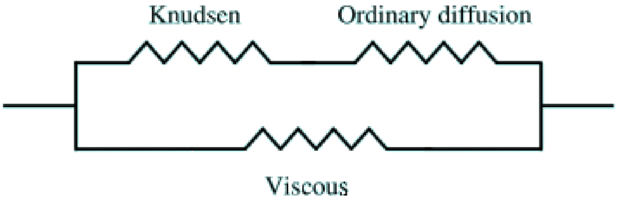

Figure 2-2 Electrical analogy circuit showing DGM model

The following are the different expressions for the permeance, K*, for each mass transport mechanisms (Lawson & Lloryd, 1997; Khayet, 2011):

$$K_K^* = \frac{\varepsilon}{\tau\delta RT_m} D_K \qquad \text{Eq. 2-14}$$

$$K_D^* = \frac{\varepsilon P_T D_{w.a}^{P_T}}{\tau\delta RT_m p_a} \qquad \text{Eq. 2-15}$$

$$K_P^* = \frac{\varepsilon r^2 M p_i}{8\delta RT_m \tau\mu} \qquad \text{Eq. 2-16}$$

where τ is the tortuosity of the membrane, R is the gas constant, P_T is the total pressure, r is the radius of the membrane pore, p is the partial pressure and its subscript refer to the transported compound. The subscripts K, D and P denotes Knudsen, molecular diffusion and Poiseuille flow. D_K and $D_{w.a}^{P_T}$ are the diffusion coefficients for Knudsen diffusion and ordinary diffusion of water vapour in air respectively.

D_K is given by the expression:

$$D_K = \frac{d}{3}\sqrt{\frac{8RT_m}{\pi m_w}} \qquad \text{Eq. 2-17}$$

where d is the diameter of the pore, and $D_{w.a}^{P_T}$ can be found using the empirical formula (Phattaranawik, et al., 2003):

$$D_{w.a}^{P_T} = \frac{(1.895 \times 10^{-5}){T_m}^{2.072}}{P_T} \qquad \text{Eq. 2-18}$$

Considering the typical pore size of DCMD membrane, in 2004 Khayet et al. (Khayet, et al., 2004) concluded that without deaeration, the mass transport mechanism in DCMD was contributed by only Knudsen and molecular diffusion, which for stagnant air, DGM was considered to be reduced to:

$$\frac{J_w^D}{D_{Kw}} + \frac{p_a J_w^D}{D_{w,a}^{P_T}} = -\frac{1}{RT}\nabla p_w \qquad \text{Eq. 2-19}$$

which J_w^D is the diffusive flux of water vapour through pore. Accounting the membrane properties and integration yields:

$$J_w^D = \frac{\varepsilon P_T D_{w,a}^{P_T}}{\delta R T_m} . \ln \left[\frac{D_{Kw} . y_{a,pm} + D_{w,a}^{P_T}}{D_{Kw} . y_{a,fm} + D_{w,a}^{P_T}} \right] \qquad \text{Eq. 2-20}$$

In Eq. 2-20, the diffusive flux, J_w^D, equates to the total transmembrane flux, N, in DCMD system.

More recently Essalhi and Khayet (Essalhi & Khayet, 2013) have weighted the contribution of Knudsen to molecular diffusion, with the weighing being an adjustable parameter:

$$K^*{}_{Essalhi} = \left(\frac{\alpha_{Essalhi}}{K^*{}_k} + \frac{1 - \alpha_{Essalhi}}{K^*{}_D}\right)^{-1} \qquad \text{Eq. 2-21}$$

which $\alpha_{Essalhi}$ is the contribution of Knudsen diffusion to mass transfer.

Using their own-manufactured polyvinylidene fluoride (PVDF) electrospun nano-fibers membranes (Essalhi & Khayet, 2012; Essalhi & Khayet, 2013; Essalhi & Khayet, 2014) which have a range of membrane properties including various membrane thicknesses, they have observed that the value of α increases with the increase of the ratio of the mean electrospun fibre diameter to the inter-fibre space. It is worth pointing out that from Essalhi’s experimental data, no significant changes were observed in the mean fibre diameter and the changes in the ratio of the mean electrospun fibre to inter-fibre space were dominated by the changes in inter fibre space. In other words, the contribution of Knudsen diffusion increases as the Knudsen number (Kn), which is defined as the ratio of the mean free path to the diameter of pores (inter fibre space), increases.

It is reported from experimental data that the values of K* are only slightly dependent on temperature thus can be considered as relatively constant in MD process (Zuo, et al., 2011; Bui, et al., 2010; Song, et al., 2007).

2.2. Factors affecting DCMD performance

The permeate flux, thermal efficiency and the module production rate are the three common indices used for assessing the performance of a DCMD unit. They are determined by both the operational parameters and membrane properties. Comprehensive literature reviews on these various factors have been made by various groups (Lawson & Lloyd, 1996; Drioli, et al., 2000; El-Bourawi, et al., 2006; Khayet, 2011; Alkhudhiri, et al., 2012; Wang & Chung, 2015), and therefore only a short summary on each factor is included in the following two sub-sections, the first considers various operational parameters, the latter various membrane properties.

2.2.1. Operational parameters

Operational parameters include feed and permeate flowrate, temperature and concentration. In some system where mechanical stirring is introduced, the mixing speed is also included as an operational parameter.

2.2.1.1. Feed and permeate temperature and concentration

Given that water vapour pressure increase exponentially with temperature (see Eq. 2-12), the water vapour flux also increases exponentially corresponding to the temperature rise of the saline feed (Singh & Sirkar, 2014). Evaluating from validated DCMD models, it is demonstrated that thermal efficiency increases with feed temperature (Al-Obaidani, et al., 2008; Gryta, 2012) while TPC also decreases with feed temperature (Manawi, et al., 2014). On the other hand, while transmembrane flux increases with lower permeate temperature, the effect of lowering permeate temperature is significantly less (2-fold) than the impact of feed temperature (Alklaibi & Lior, 2005). On the other hand, it is reported that TPC increases with permeate temperature (Manawi, et al., 2014).

An increase in feed solution concentration reduces the transmembrane flux due to the reduction in water activity (Martínez-Díez & Vázquez-González , 1999). It is reported that when the feed concentration is high (167 g NaCl/L), which is over 4 times concentration of seawater, a 40% reduction in permeate flux was reported (Gryta, 2012). Similarly, Yun et al. (2006) have observed that when the concentration of NaCl solutions is above 25%, water fluxes decrease sharply. However for the application in desalination of brackish water or seawater (around 3.5 w/w%), it was observed the effect of the presence of salt is almost negligible (Lawson & Lloyd, 1996).

2.2.1.2. Fluid flowrates

Fluid flowrates, and, when applied, the rate of mechanical stirring, determine the heat transfer coefficients. Higher heat transfer coefficients in DCMD can reduce the effect of temperature polarization (see Eq. 2-7) on both the feed and permeate side of the membrane, as well as reduce the effect of concentration polarization on the feed side of the membrane. In general higher heat transfer coefficients enhance transmembrane flux and thermal efficiency (Al-Obaidani, et al., 2008; Bui, et al., 2010; Zuo, et al., 2011) and reduce the effect of temperature polarization (Manawi, et al., 2014). Literature (Alklaibi & Lior, 2006) has suggested that the increase in feed flowrate has a higher influence on permeate flux compared to the increase permeate flowrate.

When the flow rate or stirring rate is low, the rate controlling step in the MD process is the heat transfer in the boundary layers and when the flow rate or stirring rate is high, the membrane resistance becomes the rate controlling factor if the membranes are relatively thick. Although higher circulation or stirring rate are generally favourable, the increased pressure drop leads to correspondingly increases in power input.

2.2.2. Membrane properties

Most available MD membranes are single-layered, with some groups fabricating multi-layers membrane to enhance the membrane performance. The membranes separate the saline feed from the permeate whilst also providing channels (pores) for vapour flow. Each membrane property, including hydrophobicity of the membrane material, porosity, pore size, tortuosity and thickness, has a significant influence on permeate flux and thermal efficiency. These membrane properties are controlled during the fabrication process.

2.2.2.1. Membrane materials and fabrication technique

A suitable material for MD membranes should have a low surface energy (high in hydrophobicity) and poor thermal conductivity. Polyethylene (PE), polypropylene (PP), polytetra-fluoroethylene (PTFE) and polyvinylidene fluoride (PVDF) are popular materials used in MD membranes due to their hydrophobicity, chemical resistance and thermal stability. With the aim to improve the system performances by either reducing the thermal conductivity and/or increasing the permeability of the membrane, multi-layered membranes fabricated as a hydrophobic/hydrophilic composite membrane have been made, with the different hydrophilic materials being polyetherimide (PEI), polyethersulfone (PES) or polysulfone (PS) (Khayet, 2011; Song, et al., 2008; Förch, et al., 2009; Qtaishat, et al., 2009). Chemical treatments, such as fluorination, can enhance the hydrophobicity of materials to have water contact angles as high as about 120^{o} (Zisman, 1964). Membranes with high roughness, such as those fabricated by electrospinning, can demonstrate a superhydrophobic surface with a water contact angle even greater than 150^o (Liao, et al., 2013).

2.2.2.2. Porosity and pore size

Porosity, defined as the void volume fraction, should be as high as possible as the open space allow more vapour to pass through. From Eq. 2-14, Eq. 2-15, Eq. 2-16 and Eq. 2-20, a linear relationship is used to describe the porosity and membrane permeability. In addition, with a higher porosity, less heat is conducted away by the membrane materials. Most commercial MD membranes have porosity between 60-80%.

The pore size of MD membranes is limited by the liquid entry pressure (LEP), the minimum transmembrane pressure required for liquid to enter into the pore, i.e. for pore wetting to occur. The relationship between LEP and the largest allowable pore size is given by Laplace’s (Cantor) equation, Eq. 2-22.

$$\mathrm{LEP} > \mathrm{P_{liquid}} - \mathrm{P_{vapour}} = \frac{2\gamma\cos\beta}{\mathrm{r_{max}}} \qquad \text{Eq. 2-22}$$

where γ is the surface tension at the interface and β is the contact angle. By rewriting Eq. 2-22, the size of the largest pore is given by:

$$\mathrm{r_{max}} < \frac{2\gamma\cos\beta}{\mathrm{LEP}} \qquad \text{Eq. 2-23}$$

2.2.2.3. Tortuosity and pore size distribution

Pore tortuosity and pore size distribution are unavoidable imperfect membrane features. While pores with straight cylindrical walls and uniform sizes are ideal, the ideal case is yet to be made achievable for microscopic structures. A tortuosity factor of 2 is often included for MD membrane modelling (El-Bourawi, et al., 2006; Phattaranawik, et al., 2003) even though a range of values are observed. Other expressions used for tortuosity include the following (Beeckman, 1990; Singh & Sirkar, 2014; Pantoja, et al., 2015; Kohav & Moshe, 1991):

$$\tau = \frac{\varepsilon}{1-(1-\varepsilon)^{1/3}} \qquad \text{Eq. 2-24}$$

$$\tau = \frac{1}{\varepsilon} \qquad \text{Eq. 2-25}$$

$$\tau = \frac{(2-\varepsilon)^2}{\varepsilon} \qquad \text{Eq. 2-26}$$

The nominal pore size, pore size distribution and the maximum pore size on a membrane sample can be measured using porometer. Laganà et al (Laganà, et al., 2000) and Phattaranawik et al. (Phattaranawik, et al., 2003) used a symmetric Gaussian function in modelling pore size distribution and found that their models produce good prediction.

2.2.2.4. Membrane thickness

While the effect of other membrane properties are generally understood, the role of membrane thickness is less straightforward and its effect to DCMD performance has been unclear and non-conclusive (Drioli, et al., 2015). Membrane thickness plays a significant role in DCMD systems. With a thicker membrane, less heat is conducted away from the feed side to the permeate side, giving a higher difference in transmembrane temperature that results in a higher driving force. However the membrane structure reduces the ease of permeation and impedes the transmembrane flux. Since the membrane thickness is inversely proportional to both the rate of mass and heat transfer across the membrane, provided other membrane parameters remain the same, many researchers suggested the thickness of the single layer membrane might be expected to have an optimal value (Laganà, et al., 2000). Previously for DCMD configurations, experiments have been carried out using available commercial membranes with pure water as feed and for various membrane thicknesses. For similar pore size and porosity, thicker membranes resulted in flux reduction (El-Bourawi, et al., 2006; Essalhi & Khayet, 2013). Gostoli et al. (Gostoli, et al., 1987) reported that for thin membranes, the transmembrane flux depends on the salt concentration whilst for thicker membranes; salt concentration does not play an important role on the flux. Schofield et al. (1990) demonstrated that with the membranes he used, the permeability of the membrane was virtually independent of membrane thickness (Schofield, et al., 1990). Using a computer simulated counter current hollow fibre DCMD module, Laganà suggested that the optimal thickness of a single hydrophobic layer membrane lies between 30-60 μm (Laganà, et al., 2000). Whilst in their model, Al-Obaidani et al. show that the flux drop by about 70% when the membrane thickness increases from 0.25 to 1.55mm, they also identified that an optimal thickness value of 0.7mm for their model, at which it exhibits a maximum thermal efficiency, when operating with a low temperature gradient (<5 ˚C) (Al-Obaidani, et al., 2008).

2.3. Membrane module

Flat sheet modules and hollow fibre modules are the most commonly used designs in both industry and research. Flat sheet membranes are easier to fabricate and more robust while hollow fibre modules are more compact with more membrane area packed into the same volume. In literature, most of the optimizations regarding MD process focuses on optimal operating conditions for a certain module (Bui, et al., 2010; Al-Obaidani, et al., 2008). Regarding hollow fibre module design for membrane distillation, relatively little literature has provided detailed assessment or optimization on individual component’s sizing on module performance. For crossflow module, Zuo et al. reported that there was a critical value of membrane area beyond which extra membrane area had a limited impact on water production (Zuo, et al., 2011).

Module sizing optimization is useful when there are certain fixed inputs (e.g. using waste heat from another process) and when there is a fixed demand of product water. Module production increases with the size of the module, however heat loss due to water evaporation leads to a drop of the temperature between the inlet and outlet, the nonlinear relationship between vapour pressure and temperature means flux reduces as membrane length increases (Camacho, et al., 2013). Moreover while a longer and more densely packed module typical has higher heat transfer coefficient in the shell side and a higher production per pass, the pressure drop is also higher (Costello, et al., 1993) which would increase pumping cost and the risk of membrane wetting (see Eq. 2-22). Furthermore, using a model that includes flow maldistribution in randomly packed module, Ding et al. concluded that packing density almost has no influence on transmembrane flux (Ding, et al., 2003), even though the heat transfer coefficient varies correspondingly to the change in pack densities.

2.4. Modelling approach for DCMD module and process

2.4.1. Membrane module

When adopting one-dimensional mass transfer model for MD module simulation, including DGS described in Section 2.1.4, a typical approach is to divide the model into smaller elements or steps and numerical methods are used to solve the non-linear MD equations simultaneously (Song, et al., 2007; Al-Obaidani, et al., 2008; Zuo, et al., 2011; Guan, et al., 2014; Pantoja, et al., 2015). The outputs from one element are passed into the next element. The final output values are compared to experimental data for validation.

Apart from one-dimensional models, recently two and three dimensional heat and mass transfer MD models have been developed. Monte Carlo simulation of DCMD can describe the vapour movement within the interconnected pores in the membrane structures (Imdakm & Matsuura, 2004; Khayet, et al., 2010; Imdakm & Matsuura, 2005). Computational fluid dynamics (CFD) models have also been used for module designs to investigate local temperature and concentration polarization, flux and pressure drop in lab-scale modules (Yu, et al., 2012; Yang, et al., 2012; Yang, et al., 2012). Furthermore, a state-of-the-art three dimensional model based on kinetic theory of gases was introduced that simulates pore size distribution and interconnectivity within the membrane (Hitsov, et al., 2015). While these methods of modelling provide good estimates and predictions on DCMD performances, the establishment (constructing and running) of these models could be rather difficult and time consuming, especially in the case of CFD simulations (Guan, et al., 2014).

2.4.2. Effectiveness-Number of Transfer Units method

Due to its robustness, the effectiveness-Number of Transfer Units (E-NTU) method, popularised by Kays and London (Kays & London, 1984) has become the industrial standard for designing heat exchanger systems and networks (Tan & Liu, 1990; Mathew & Hegab, 2010; Fakheri, 2014; Serth & Lestina, 2014) for many years. As a design tool, the E-NTU method can be used to calculate the rate of heat transfer in heat exchangers when the temperature profile is unknown and when there is insufficient information to obtain the log-mean temperature. It is also used to determine the required surface area of the heat exchanger for a fixed effectiveness and set of inlet conditions. Recently, different researchers have used the backbone of the original version of E-NTU, which only applies to heat exchangers, for various mass transfer systems. Sharqawy et al. (2013) has developed the effectiveness-mass transfer units (E-MTU) for pressure retarded osmosis (PRO) membrane mass exchanger and similarly, Banchik et al. (2014) has developed E-MTU for reverse osmosis (RO). Others have also looked into the use of E-NTU in dehumidification, which is a conjugate heat and mass transfer system (Ren, et al., 2007; Zhang, 2010). The E-NTU has yet to be applied to DCMD and we explore its use in Chapter 4.

2.4.3. MD process simulation using Aspen Plus

For process design purposes, while the inputs and outputs of any individual component in a flowsheet can be calculated separately (He, et al., 2013; Pantoja, et al., 2015; Chen, et al., 2012), several reports have used Aspen software for flowsheet simulation (Chang, et al., 2009; Zuo, et al., 2011; Guan, et al., 2014). Aspen Plus is a flowsheet simulation platform developed by Aspentech. With an extensive library of chemical and thermodynamic property data along with a wide range of standard process operation block, for example, various designs of heat exchangers and distillation columns, Aspen has gained popularity amongst process design engineers. Compared to Aspen HYSYS which is another similar software package provided by Apsentech, Aspen Plus is primarily used for chemical processes and Aspen HYSYS is used primarily for oil and gas processes (Aspentech, 2015).

Since MD is yet to be a popular process industrially, in order to incorporate DCMD modules into Aspen Plus, a customized unit model is required. Due to software restriction, Aspen does not compile with any COM-interface, like MATLAB, directly, customised unit models can only be created using either FORTRAN or Visual Basic for

Applications (VBA) (Aspen Technology, Inc., 2012; Xu, et al., 2014) which impose an additional complexity in the implementation. Recently researchers have found ways to bridge this gap by an indirect interface using Microsoft spreadsheet for Aspen HYSYS and MATLAB (Liu, 2012; Etoumi, 2014). In chapter 5 of this thesis, a similar link is built to incorporate a MATLAB simulated model into Aspen Plus. Alternate methods are also presented to enhance the simulation speed while using result from both MATLAB and Aspen simulations.

2.5. Gaps for further research

Based on the review of the literature, there are a few gaps and key issues in the literature for which this thesis aims to address. The key issues include:

(a) Better understanding and investigation of the role of membrane thickness in DCMD performance;

(b) The use of conventional DGM in DCMD in one dimensional mass transfer modelling;

(c) The lack of effective design method for DCMD systems, which could be further broken down into:

  (i) Generic design method for DCMD systems;

  (ii) A more conclusive study on DCMD hollow fibre module design and configuration on DCMD performance; and

  (iii) More effective ways of incorporating DCMD models into flowsheet simulation software, i.e. Aspen Plus, for process design and optimization.

3. The effect of membrane thickness upon transmembrane flux

3.1. Introduction

In this Chapter, the effect of membrane thickness and optimal membrane thickness are investigated and evaluated both experimentally and analytically. Experimentally, MD membranes of different thickness were fabricated using electrospinning and the characteristics and performance of the membranes were tested and evaluated. A MATLAB model of a countercurrent DCMD flatsheet membrane module was constructed to explore further of the experimental results. Analytically, an expression for the theoretical optimal membrane thickness was derived algebraically and solved graphically.

As discussed in Section 2.2.2.4, Membrane thickness plays a significant role in DCMD systems. It is inversely proportional to both the rate of mass and heat transfer across the membrane. With a thicker membrane, less heat is conducted away from the feed side to the permeate side, giving a higher difference in transmembrane temperature that results in a higher driving force. However the membrane structure reduces the ease of permeation and impedes the transmembrane flux. Thus conceptually, provided other membrane parameters remain the same, an optimal membrane thickness is anticipated which would yield the highest transmembrane flux: with a membrane thick enough to provide sufficient transmembrane temperature difference required to drive the vapour flux while not too thick that the membrane structure impede the flow too significantly.

3.2. Experimental approach

Membranes with different thicknesses were prepared using electrospinning for different length of time. After the electrospun membranes were dried thoroughly, they were further treated by a heat press machine, which gave the electrospun membrane a more intact structure.

3.2.1. Membrane fabrication by electrospinning

Compared to other membrane fabrication methods, electrospinning was chosen because the amount of the membrane material, which relates to the thickness of the membrane, can be controlled relatively easily by altering the electrospinning time. Figure 3.1 shows the schematic of the electrospinning setup used (dimensions detailed in section 3.2.1.2). The electrospinning dope solution (preparation detailed in Section 3.2.1.1), was injected to the charged tip by a syringe pump. The dope outlet tip was mounted onto a moving stage that allows horizontal movement for the control of the size of the membrane fabricated. A cylindrical, rotating, earthed metal collector was placed below the outlet tip. During operation, charged nanofibre deposited onto the rotating collector, producing a strip around the perimeter. For the present work, the recorded electrospun membranes were fabricated by spinning for 4 to 10 hours.

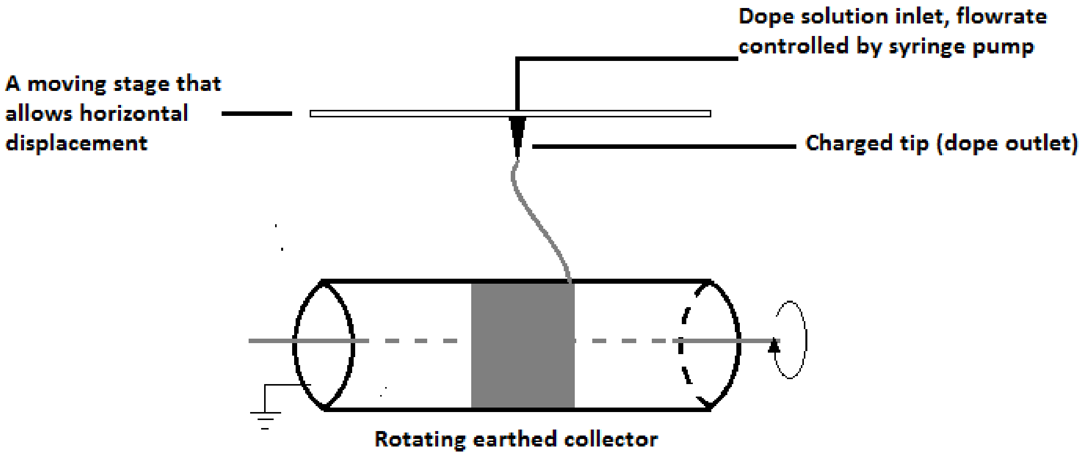

Figure 3.1 Schematic of the electrospinning setup used for membrane fabrication.

3.2.1.1. Preparation of electrospinning dope solution

The materials and chemicals used are listed in Table 3-1. The preparation method composition of the dope solution was recommended by Liao et al. (2013). PVDF readily dissolves in organic solvent and possesses good hydrophobicity. Prior to use, the PVDF polymer, in powder form, was dried at 323K under vacuum condition for at least 24 hours, to ensure all the moisture was removed. The dope solution was then prepared by dissolving 5 wt% PVDF into a mixture of DMF and acetone with a weight ratio of 6 to 4 followed by adding 0.004 wt% of Lithium Chloride, LiCl, powder into the solution. LiCl enhanced the electrical conductivity of the dope solution, resulting in finer nanofibers. The solution was stirred mechanically with a magnetic bar for 24 hours at 333K to ensure thorough dissolving and cooled at room temperature for 24 hours prior to the electrospinning process.

Table 3-1 List of chemicals included in the electrospinning dope solution

Chemical	Supplier
PVDF Kynar HSV 900	Arkeme Inc., Singapore
Acetone	Fisher, Singapore
N,N-Dimethylformamide (DMF)	Fisher, Singapore
Lithium chloride (LiCl)	Merck, Singapore

3.2.1.2. Electrospinning conditions and Heat press post - treatment

With the setup demonstrated in Figure 3.1, a potential difference of 27kV was applied between the dope outlet tip and the collector, which were placed 120mm apart. The flowrate of dope solution was set at 1.8 cm^3 h^{-1} while the moving stage moved horizontally back and forth, at a speed of 0.1mm s^{-1}, across a length of 8cm. After the electrospinning process, the membranes were then dried in a fanned incubator for 24 hours, at 323K, to ensure all the solvents were evaporated before heat press treatment.

For the heat press post-treatment, the dried PVDF membranes were placed between two flat glass panes, which were then transferred to the heat press machine. An image of the heat press machine set up is included in Appendix A1. The heat press was operated at 423K for 1 hour and the hot plate were just touching the surfaces of the glass panes, without exerting any noticeable pressure as measured by the pressure gauge. The melting temperature of PVDF used was approximately 443K under ambient pressure.

3.2.2. Characterization of electrospun membrane

It is essential to characterize the membrane parameters, including porosity, pore sizes, hydrophobicity and membrane surface roughness.

The porosity of the membrane was calculated using a gravimetric method with the membranes being immersed into isopropyl alcohol (IPA) which penetrates into the pores of the membrane. The membrane porosity is calculated using the following equation:

$$\varepsilon \ = \frac{\left(w_{wet} - w_{dry}\right)/\rho_{IPA}}{\left(w_{wet} - w_{dry}\right)/\rho_{IPA} + w_{dry}/\rho_{PVDF}} \qquad \text{Eq. 3-1}$$

where w denotes weight and ρ is the density of the chemical and the subscripts denote the chemical or the membrane condition, whether it is dry or wetted.

The pore size of the membranes was determined by a capillary flow porometer (model CFP 1500A, from Porous Material. Inc. (PMI) in Singapore). To measure and quantify the hydrophobicity of the membrane surface, the contact angle between the membrane surface and a water droplet, a 5 µL sessile drop of deionized water, was measured. The contact angles of the membranes were measured using a goniometer software (Contact Angle System OCA, from Data Physics Instruments GmbH in Singapore). The membrane surface roughness was evaluated by observing and comparing the nanofibre structure and diameter on the membrane surface. Scanning electron microscopy (SEM) (EVO, 50 Carl Zeiss AG, Singapore) was used to take magnified images of the membrane surface for the evaluation. The membrane samples were sputtered with platinum dust prior to SEM. To observe the cross-sectional morphology of the membrane using SEM, pieces of membrane sample were broken in liquid nitrogen before coating with by platinum dust. The thickness of the membranes was measured in two ways: with a standard micrometer and also by using SEM images (as demonstrated in Figure 3.5).

3.2.3. DCMD performance tests

The electrospun membranes were tested using the a DCMD experiment setup, shown in Figure 3.4. The size of the membrane module had an effective membrane area of 36 cm^2. The dimensions of the feed and permeate channels were identical with a length of 9 cm, a width of 4cm and a depth of 2 mm. While deionized water was used on the permeate side throughout all the tests, 10% (w/w) NaCl concentration was used as feed solution and the mass flowrates were maintained at 1.5 kg min^{-1} on each channel. The membrane module was placed vertically with hot saline feed and cold deionized water running counter-currently. Figure 3.4 shows the schematic setup of the experiment. Fluxes were determined by collecting permeate from runs that lasted for between 3 to 5 hours. The conductivity of the permeate was monitored throughout the experiment to ensure there was no membrane wetting. While the permeate temperature were kept at 293K, the feed temperature was varied within the range 318-338K. At each condition at least three evaluations were made and as the membranes were fragile, new membranes were used for each testing. Fluxes were calculated to an accuracy of better than ±5% and therefore the variation in the fluxes at a given thickness reflects the variation in porosity and pore size that arise naturally from the electrospinning process.

3.2.4. DCMD simulation for performance prediction

In order to further explore the experimental data, effectively interpolate or extrapolate the results, a counter current DCMD flatsheet membrane module model simulation was constructed with MATLAB. The modules were divided into many thin strips in the streamwise direction in the mathematical model. For each element, the governing equations of MD (Eq. 2-1-Eq. 2-11) were solved with MATLAB function, *fsolve*. Outputs from each strip including outlet temperature and flow rate, were used as input for the next strip (as depicted in Figure 3.2) using Eq. 3-2 – 3-5:

$$\mathrm{T_{f,j+1}} = \mathrm{T_{f,j}} - \frac{\mathrm{q_j A_{ele}}}{\mathrm{\dot{m}_{f,i} c_f}} \qquad \text{Eq. 3-2}$$

$$\mathrm{T_{p,j}} = \mathrm{T_{p,j+1}} + \frac{\mathrm{q_j A_{ele}}}{\mathrm{\dot{m}_{p,i} c_p}} \qquad \text{Eq. 3-3}$$

$$\mathrm{\dot{m}_{f,j+1}} = \mathrm{\dot{m}_{f,j}} - \mathrm{N_j A_{ele}} \qquad \text{Eq. 3-4}$$

$$\mathrm{\dot{m}_{p,j}} = \mathrm{\dot{m}_{p,j+1}} + \mathrm{N_j A_{ele}} \qquad \text{Eq. 3-5}$$

which $\mathrm{A_{ele}}$is the elemental membrane area, c is the specific heat capacity of the fluid and the subscript j denotes the corresponding values obtained for the j th element.

Since the permeability (K in Eq. 2-11) of the membranes was not known, a base permeability, K_o, was determined using Matlab function, fmincon. The explanation for such base permeability is reported in Section 3.2.5.1. It is also worth noting that the flowrates were the same for each channel and invariant and so the heat transfer coefficients would be the same if the temperatures were the same. However temperature was different on either side of the membrane and this affects the viscosity. With turbulent flow along the channels, one can relate the heat transfer coefficients h_f and h_p to each other by assuming that the ratio is $(\mu_f/\mu_p)^{-0.5}$. Using this assumption, the base permeability K_0, h_f and h_p are estimated using our experimental data and MATLAB optimization function, fmincon. Fmincon is an optimization function included in MATLAB optimization toolbox. It allows user to specify constraints and optimize a few variables simultaneously. In this case, the value of K_0 is fixed as constant. Each data collected in our experiment were used to compute the value of K_0 that best fits all the data. Meanwhile the values of h_f and h_p at different temperature were computed using the assumption stated previously. Fmincon is used to ensure a constant K_0 for our analysis. It can also avoid any potential systematic errors when an empirical formula is used to calculate the heat transfer coefficients. The values of h_f and h_p obtained were within the estimates obtained from the data itself using the method given in (Field, et al., 2013).

With a counter-current set-up, it is necessary to initiate the simulation by making an initial selection for one of the outlet temperatures, in this case the feed output temperature. The inlet temperatures of both streams are known. Temperatures, heat and mass fluxes across the membranes and other variables are then calculated. An calculation loop was set up to ensure that the temperature profile on the permeate side converged to match the known fixed input permeate temperature. The algorithm used is shown in the algorithmic state machine (ASM) chart, Figure 3.3.

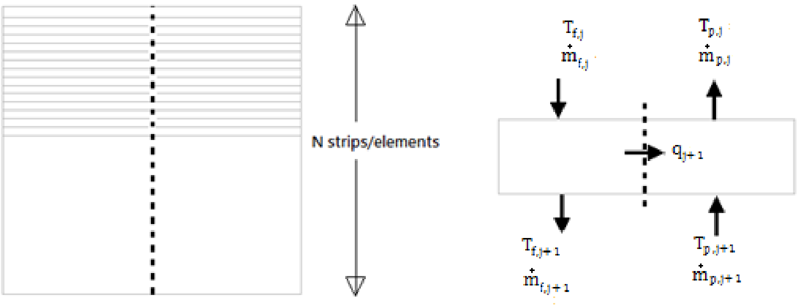

Figure 3.2 Flat sheet module divided into strips (left) and an enlargement of a strip (right)

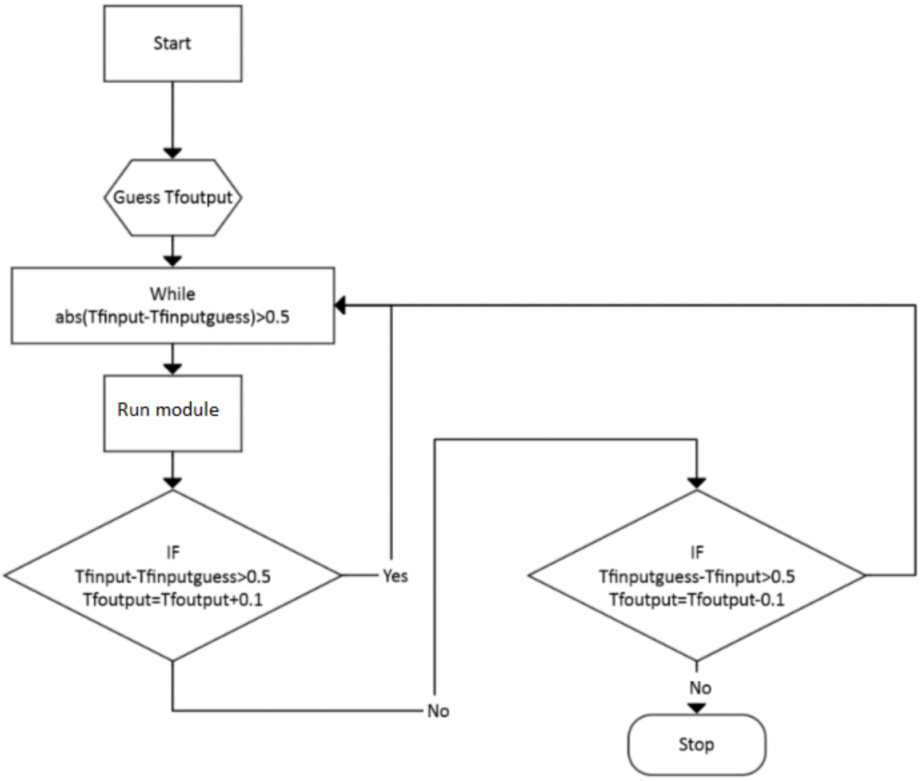

Figure 3.3 Counter-current optimization logic diagram.

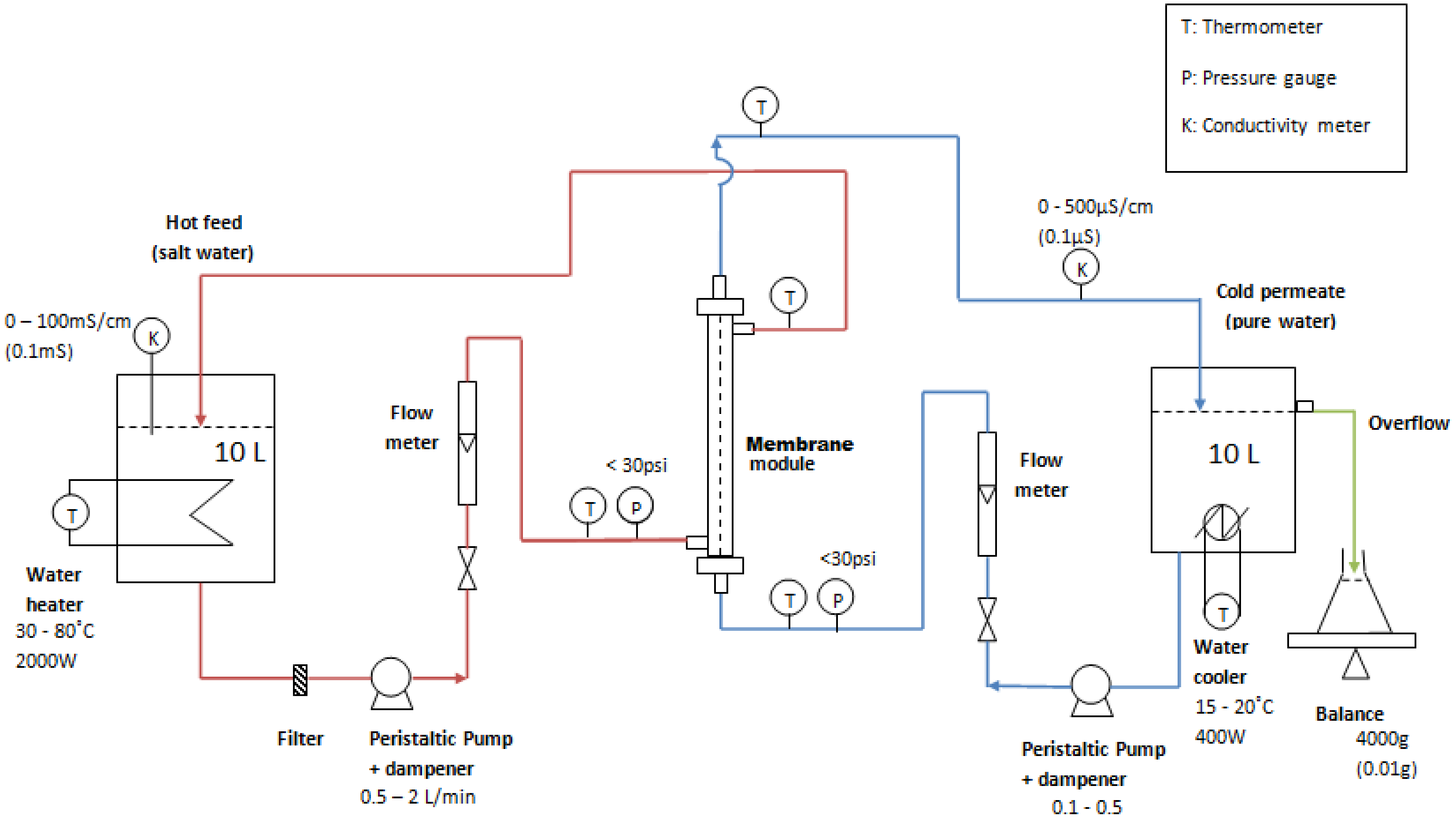

Figure 3.4 Schematic of the DCMD test setup used for membrane performance evaluation.

Table 3-2 Characteristics of the nanofibre membranes with different electrospinning time

Electrospinning time (h)	**4**	**6**	**8**	**10**
Without heat treatment				
Porosity (%)	92.3±0.4	90.6±0.7	90.5±0.8	89.2±1
Ave. fibre diameter (μm)	0.14±0.06	0.14±0.05	0.15±0.07	0.14±0.03
Ave. pore diameters (μm)	0.33±0.17	0.31±0.17	0.29±0.15	0.25±0.11
Thickness (μm)	36.4±2.5	46.4±2.5	64.3±2.5	77.0±2.5
Contact angle (degree)	139.4±1.2	141.0±0.5	140.8±1.8	139.0±0.3
With heat treatment				
Porosity (%)	83.6±0.4	80.8±0.2	80.0±1	80.5±0.4
Ave. fibre diameter (μm)	0.16±0.05	0.15±0.04	0.15±0.03	0.16±0.03
Ave. pore diameters (μm)	0.21±0.09	0.18±0.06	0.17±0.08	0.15±0.07
Thickness (μm)	27.9±2.5	35.6±2.5	45.7±2.5	58.4±2.5
Contact angle (degree)	130.6±1.6	129.9±1.5	131.3±2.5	130.0±2
Structural deviation factor: Φ (See Section 3.2.5.1)	*1.45*	*1.20*	*1.13*	*1*

3.2.5. Experimental results

3.2.5.1. Membranes characterization

The properties of various electrospun membranes are recorded in Table 3-2, which includes results obtained before and after the heat-press treatment. It is evidential from the reduction in membrane thickness, porosity and pore size, that the heat press treatment created a denser structure for the membranes. This is important as literature (Liao, et al., 2013) shows that without heat press treatment, air bubbles could be trapped within membrane structure during operation. The reduction of membrane thickness caused by heat press process was roughly 25%±4% for all membranes with a range of thickness. This consistency suggests that the change, in thickness, caused by the process is proportional to the amount of membrane materials present in the samples. The intact structure of the nanofibre membranes can be observed using SEM imaging, as shown in Figure 3.5. The cross sectional SEM image show the numerous layers of fibre within the membrane structure and the membrane top surface images show that the nano-fibrous structure was clearly preserved after the heat treatment and each fibre is well defined. The top cross sectional SEM image shows that there is an observable deviation in thickness across the electrospun membrane, which is due to the uneven spreading of fibres during electrospinning. An average membrane thickness value was always evaluated in this work. Moreover from Table 3-2, it is observed that the fibre diameter and contact angle of the membranes did not vary with electrospinning time of the membranes. In the case of 4-hour-sample, the porosity was significantly higher than for longer times. Apart from variation in the pore size in the samples, another possible reason of the variations in measurements could be due to the working principle of the capillary flow porometer. Firstly the sample was wetted with a wetting liquid, and an inert was introduced to displace the liquid that were trapped in the pores. The pressure required for displacing the liquid was used to determine the pore sizes. In the case of nanofibrous membranes, since the pores in the membrane were not straight but all interconnected, as the number of layer of fibre deposition increased, the overlapping of fibres increased the tortuosity of the membrane. Since the porometer does not take into account the thickness of the membrane and cannot determine the tortuosity of the sample, the change in the ease of permeation has fully translated into changes in pore size. In view of the fact that there is no accurate way of determining tortuosity of nanofibrous membrane currently, in order to account for this undetermined structural deviation in the estimation of membrane permeability, a structural deviation factor, Φ, is introduced and is defined as:

$$\Phi \quad = \frac{\mathcal{E}\, d}{\mathcal{E}_{10h} d_{10h}} \qquad \text{Eq. 3-6}$$

As suggested in Eq. 3-1 and shown in the last row in Table 3-2 that the value of Φ was relative to the membrane fabricated with electrospinning time. Its introduction was helpful for evaluating the effect of thickness alone on transmembrane flux, while the change in membrane permeability due to other membrane properties are accounted for in Φ. The function of Φ that was used in the simulations was computed by fitting a polynomial to the experimental values given in Table 2. The permeability of the membranes, K, was assumed to be ΦK_o, where $K_o$is the value for the membrane with a thickness of 58.4 microns. Using Matlab function, fmincon, the values K_o that best fits all the data is 4.5x10-11 kg (m s Pa)-1. It must be mentioned that, to account for the structural deviation observed, using the values of Φ obtained experimentally a polynomial expression for Φ as a function of thickness was included in the MATLAB simulation.

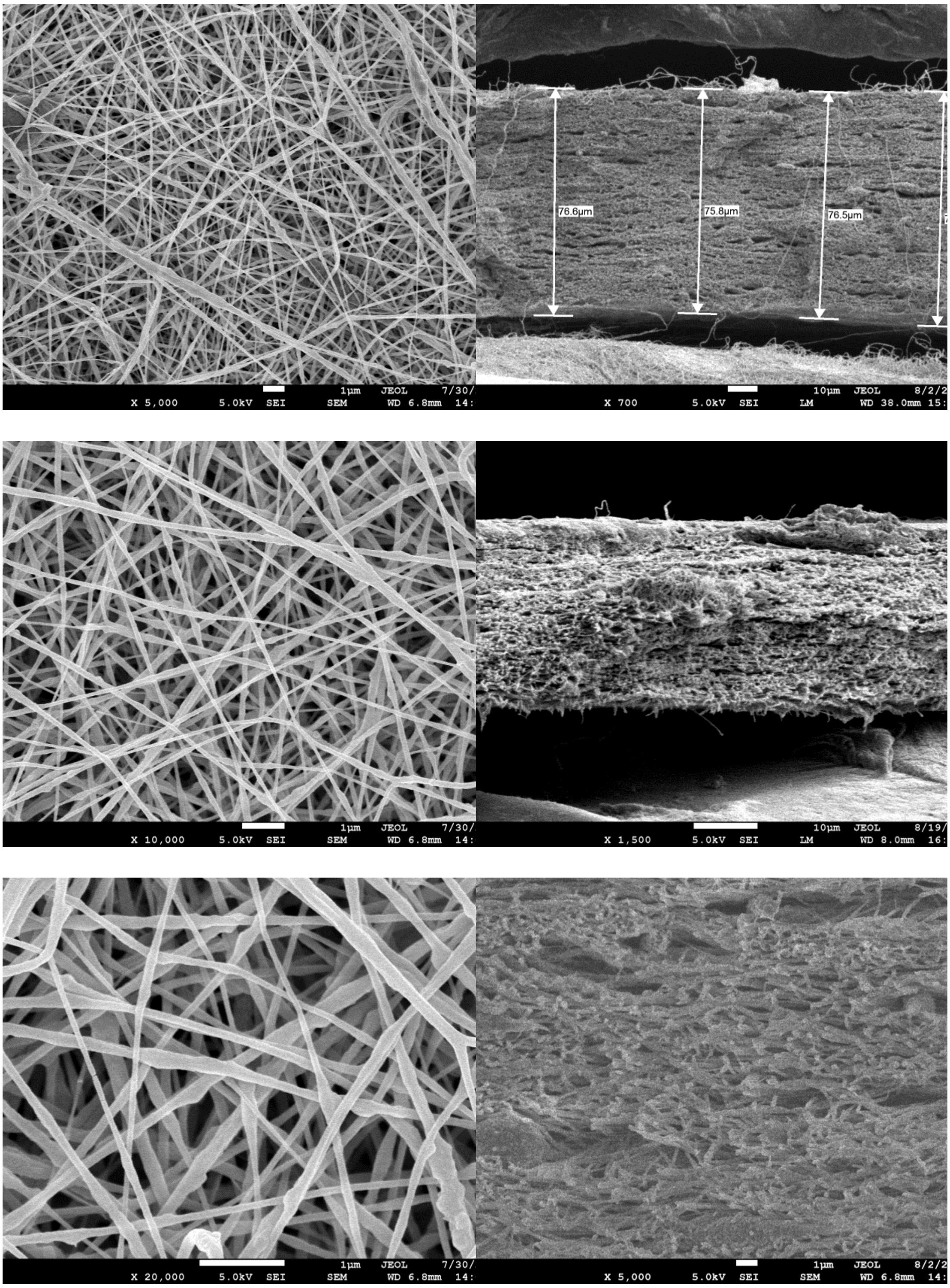

Figure 3.5 SEM images showing surface morphology (left columns) and the cross section (right column) of the nanofibre membrane, post heat press treatment, under a range of magnifications as recorded at the bottom of each individual image.

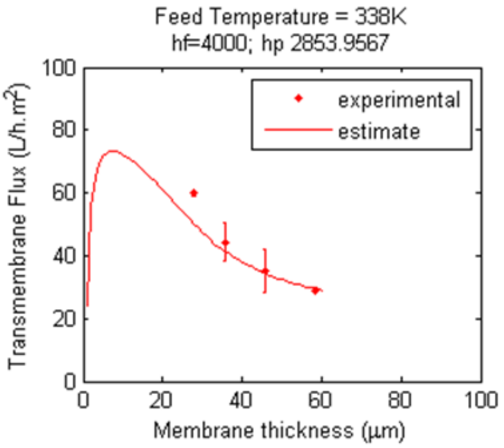

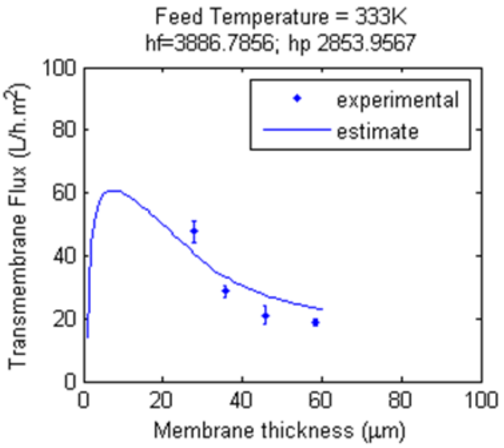

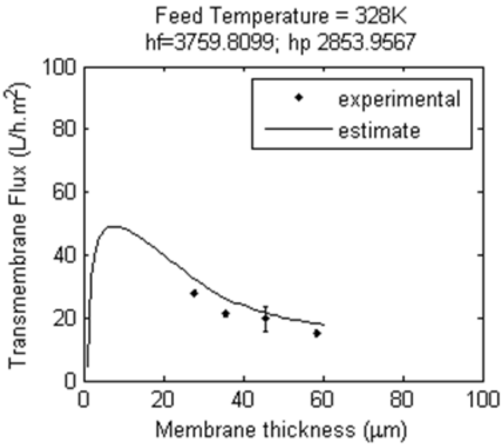

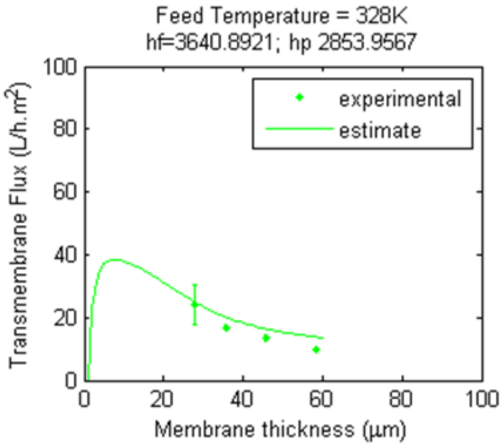

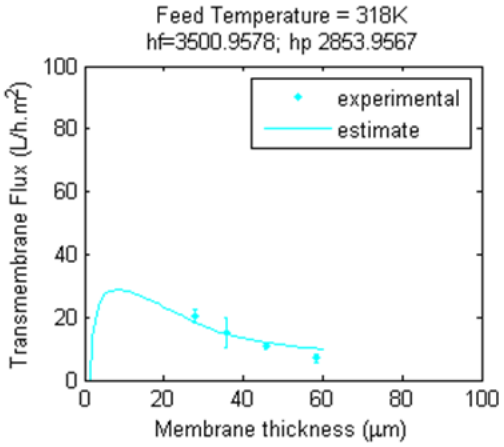

Figure 3.6 (top left) , Figure 3.7(top right), Figure 3.8(centre), Figure 3.9(bottom left) and Figure 3.10 (bottom right) show the experimental data and the estimated production rate of our DCMD experiment.

Figure 3.6 and Figure 3.10 show the data obtained experimentally and produced from the MATLAB model, which gives a good fitting to the experimental data. From these figures, it is evidenced that with for the combination of membranes and process conditions evaluated there was a clear influence of membrane thickness: the thinner the membranes, the higher the transmembrane flux. Due to the nonlinear dependence of partial pressure on temperature, a higher feed temperature results in a much higher flux. From our experiment, with the thinnest membrane, a flux of 60 L/h m^2 is obtained when the input temperature is 338 K. In contrast, when the feed temperature is 323 K, the obtained permeate flux is only about a third of this value.

It is apparent that some of the error bars especially those in Figure 3.6 were quite significant. It is suspected that due to the very thin nature of the membranes, the uncertainty in tortuosity and the non-uniformity imperfections of individual membrane and variations among each the membrane samples became more evidential. This is especially apparent when the driving force, the transmembrane partial pressure difference, increases. No experimental results were recorded for thinner membranes (with electrospinning time of 2 and 3 hours). Whilst they could be fabricated, handled and mounted onto the test module, they were not robust enough to withstand the vibrations caused by the fluid flow and were broken and wetted within an hour of testing. Thus no results were obtained for membranes with a thickness close to the predicted optimal thickness.

From the simulated data, every graph yields a peak (where maximum flux was estimated) at approximately 10 microns. This value would be the suggested for impractically thin optimal membrane.

3.3. Analytical approach

3.3.1. Obtaining expression for the optimal thickness

While there are many indices for assessing DCMD performance, including thermal efficiency, energy cost and GOR, transmembrane flux is assessed here for optimization as it is hugely dependent on membrane characteristic and is the primary data used for various DCMD performance evaluations. To access optimal thickness analytically, an expression of $\frac{dN}{d\delta}$ is first obtained by solving the governing equations of DCMD given in Chapter 2 and reproduced below, where N is the transmembrane flux and δ is membrane thickness. In this section it is assumed that there is no variation of K with thickness.

$$q_f = h_f(T_f - T_{fm}) \qquad \text{Eq. 3-7}$$

$$q_p = h_p(T_{pm} - T_p) \qquad \text{Eq. 3-8}$$

$$q_m = N\lambda + \frac{k_m}{\delta}(T_{fm} - T_{pm}) \qquad \text{Eq. 3-9}$$

$$N = \frac{K}{\delta}\left(P_{fm} - P_{pm}\right) \qquad \text{Eq. 3-10}$$

whilst

$$P_{pm} = e^{\left(23.20 - \frac{3816.44}{T_{pm} - 46.13}\right)} \qquad \text{Eq. 3-11}$$

$$P_{fm} = \alpha_w e^{\left(23.20 - \frac{3816.44}{T_{fm} - 46.13}\right)} \qquad \text{Eq. 3-12}$$

$$\lambda = mT_{fm} + g \qquad \text{Eq. 3-13}$$

where m and g are constants and have the value of -2400 (J kg^{-1} K) and 3,200,000 (J kg^{-1}). These coefficients were obtained by fitting a line of best fit to the values of specific enthalpy of water phase change given in a standard Oxford Engineering Data book

(Howatson, et al., 2009), corresponding to water temperature in the range of 293-383K. At steady state operation,

$$q_f = q_p = q_m = q \qquad \text{Eq. 3-14}$$

To solve the problem it is useful to express the feed and permeate heat transfer coefficient relatively to each other by letting:

$$h_p = bh_f \qquad \text{Eq. 3-15}$$

Also substitutions of Eq. 2-12 and Eq. 3-12 into and Eq. 2-11 yields:

$$N = \frac{K}{\delta}\left[\alpha_w e^{\left(23.20-\frac{3816.44}{T_{fm}-46.13}\right)} - e^{\left(23.20-\frac{3816.44}{T_{pm}-46.13}\right)}\right] \qquad \text{Eq. 3-16}$$

To obtain an expression for $\frac{dN}{d\delta}$, Eq. 3-16 is differentiated with respect to δ :

$$\frac{dN}{d\delta} = \frac{K}{\delta}\left[\alpha_w \frac{dP_{fm}}{dT_{fm}}\frac{dT_{fm}}{d\delta} - \frac{dP_{pm}}{dT_{pm}}\frac{dT_{pm}}{d\delta}\right] - \frac{K}{\delta^2}\left(P_{fm} - P_{pm}\right) \qquad \text{Eq. 3-17}$$

The expressions of Eq. 3-17 contains derivatives $\frac{dP}{dT}$ and $\frac{dT}{d\delta}$, which are the components of $\frac{dP}{d\delta}$ using chain rule. P_{fm} and P_{pm} are related respectively to T_{fm} and T_{pm} , as expressed in Eq. 2-12 and Eq. 3-12, the values of T_{fm} and T_{pm} are related to the thickness of the membrane. The expressions of $\frac{dP_{pm}}{dT_{pm}}$ and $\frac{dP_{fm}}{dT_{fm}}$ can be obtained by differentiating Eq. 2-12 and Eq. 3-12:

$$\frac{dP_{pm}}{dT_{pm}} = \left(\frac{3816.44}{(T_{pm} - 46.13)^2}\right) e^{\left(23.20-\frac{3816.44}{T_{pm}-46.13}\right)} \qquad \text{Eq. 3-18}$$

$$\frac{dP_{fm}}{dT_{fm}} = \alpha_w \left(\frac{3816.44}{(T_{fm} - 46.13)^2}\right) e^{\left(23.20-\frac{3816.44}{T_{fm}-46.13}\right)} \qquad \text{Eq. 3-19}$$

and further substitutions of Eq. 3-18 and Eq. 3-19 into Eq. 3-17 yields:

$$\begin{aligned}\frac{dN}{d\delta} &= \frac{K}{\delta} e^{\left(23.20-\frac{3816.44}{T_{fm}-46.13}\right)}\left[\alpha_w\left(\frac{3816.44}{(T_{fm}-46.13)^2}\right)\frac{dT_{fm}}{d\delta}-\frac{1}{\delta}\right] \\ &\quad -\frac{K}{\delta} e^{\left(23.20-\frac{3816.44}{T_{pm}-46.13}\right)}\left[\left(\frac{3816.44}{(T_{pm}-46.13)^2}\right)\frac{dT_{pm}}{d\delta}-\frac{1}{\delta}\right]\end{aligned}$$

Eq. 3-20

In addition to Eq. 3-20, another expression containing $\frac{dN}{d\delta}$ can be obtained by differentiating Eq. 3-9, which yields the following expression:

$$\begin{aligned}\frac{dQ}{d\delta} &= \frac{dN}{d\delta}\lambda + Nm\frac{dT_{fm}}{d\delta} + \frac{k_m}{\delta}\left(\frac{dT_{fm}}{d\delta}-\frac{dT_{pm}}{d\delta}\right) \\ &\quad -\frac{k_m}{\delta^2}\left(T_{fm}-T_{pm}\right)\end{aligned}$$

Eq. 3-21

From Eq. 3-7and Eq. 3-8, $\frac{dQ}{d\delta}$ and $\frac{dT_{pm}}{d\delta}$ can be expressed as:

$$\frac{dQ}{d\delta} = -h_f\frac{dT_{fm}}{d\delta}$$

Eq. 3-22

$$\frac{dT_{pm}}{d\delta} = \frac{1}{bh_f}\frac{dQ}{d\delta} = -\frac{1}{b}\frac{dT_{fm}}{d\delta}$$

Eq. 3-23

and the following expression of $\frac{dT_{fm}}{d\delta}$ is then obtained by substituting Eq. 3-22 and Eq. 3-23 into Eq. 3-21, followed by rearrangement:

$$\frac{dT_{fm}}{d\delta} = \frac{\frac{dN}{d\delta}\lambda - \frac{k_m}{\delta^2}\left(T_{fm}-T_{pm}\right)}{-h - Nm - \frac{k_m}{\delta}\left(1+\frac{1}{b}\right)}$$

Eq. 3-24

Lastly, substituting Eq. 3-23 and Eq. 3-24 into Eq. 3-20 and setting $\frac{\mathrm{dN}}{\mathrm{d}\delta} = 0$ (which corresponds to the maximum), an expression of the theoretical optimal thickness, $\delta_{\mathrm{theor.,opt.}}$, can be obtained by rearranging the equation. The expression of $\delta_{\mathrm{theor.,opt.}}$ is given as:

$$\delta_{\mathrm{theor.,opt.}} = \frac{\mathrm{k_m}\left(\mathrm{T_{fm}} - \mathrm{T_{pm}}\right)\left[\alpha_{\mathrm{w}}\mathrm{e}^{-\frac{3841}{\mathrm{T_{fm}}-45}}\left(\frac{3841}{(\mathrm{T_{fm}}-45)^2}\right) + \mathrm{e}^{-\frac{3841}{\mathrm{T_{pm}}-45}}\left(\frac{3841}{(\mathrm{T_{pm}}-45)^2}\right)\left(\frac{1}{\mathrm{b}}\right)\right]}{\mathrm{h_f}\left(\mathrm{e}^{-\frac{3841}{\mathrm{T_{fm}}-45}} - \mathrm{e}^{-\frac{3841}{\mathrm{T_{pm}}-45}}\right)} - \frac{\mathrm{k_m}}{\mathrm{h_f}}\left(1 + \frac{1}{\mathrm{b}}\right) - \frac{\mathrm{mK}}{\mathrm{h_f}}\left(\alpha_{\mathrm{w}}\mathrm{e}^{23.238-\frac{3841}{\mathrm{T_{fm}}-45}} - \mathrm{e}^{23.238-\frac{3841}{\mathrm{T_{pm}}-45}}\right) \qquad \text{Eq. 3-25}$$

This above expression includes the unknown interface temperatures. One of these can be eliminated in terms of the other by combining Eq. 3-7and Eq. 3-8.

$$\mathrm{h_f}(\mathrm{T_f} - \mathrm{T_{fm}}) = \mathrm{h_p}(\mathrm{T_{pm}} - \mathrm{T_p}) \qquad \text{Eq. 3-26}$$

$$\mathrm{T_{pm}} = \frac{\mathrm{h_f}}{b}(\mathrm{T_f} - \mathrm{T_{fm}}) + \mathrm{T_p} \qquad \text{Eq. 3-27}$$

3.3.2. Determination of theoretical optimal thickness by assessing solution graphically

After eliminating $\mathrm{T_{pm}}$ using Eq. 3-27, there remains two unknowns in Eq. 3-25, $\mathrm{T_{fm}}$ and $\delta_{theor.,opt.}$. The other parameters in the expression are controlled and determined by operational condition or membrane characteristics. With two unknowns, one more equation is required to solve the expression. A second equation relating δ and T_{fm} can be obtained by substituting Eq. 2-1, Eq. 3-8, Eq. 3-9 and Eq. 3-13 into Eq. 2-11. After rearrangement this yields:

$$\delta = \frac{K(mT_{fm} + c)(P_{fm} - P_{pm}) + k_m(T_{fm} - T_{pm})}{h_f(T_f - T_{fm})} \quad \text{Eq. 3-28}$$

Hence by applying suitable (estimated or experimental) values for b, h_f, K, k_m, which are experimental or membrane characteristic parameters, and setting the input temperatures T_f and T_p, the two expressions given by Eq. 3-25 and Eq. 3-28 can be plotted for a suitable range of T_{fm}. A solution can be obtained graphically from an intersection of the plots.

It is important to highlight that in our analytical approach, T_f is assumed to be constant which results in a constant T_{fm}. In reality, unless there is a constant heat source along the module, both T_f and T_p change along the module. The temperature changes depend on the size of the module, the rate of heat transfer and membrane thermal conductivity. Thus the value estimated experimentally for the optimum thickness would vary slightly from the analytical value.

3.3.3. Results and discussions from analytical analysis

Values (listed in Table 3-3) close to typical experimental parameters were used for the analytical model. Expressions Eq. 3-25 and Eq. 3-28 and plotted on the same graph as demonstrated in Figure 3.11.

Table 3-3 Operation and membrane structural parameters used in analytical model

Stimulation conditions		
b	1	-
h_f	2500	W/m^2 K
K	4.5x10^{-11}	kg/ m s Pa
k_m	0.045	W/m K
T_f	338	K
T_p	293	K

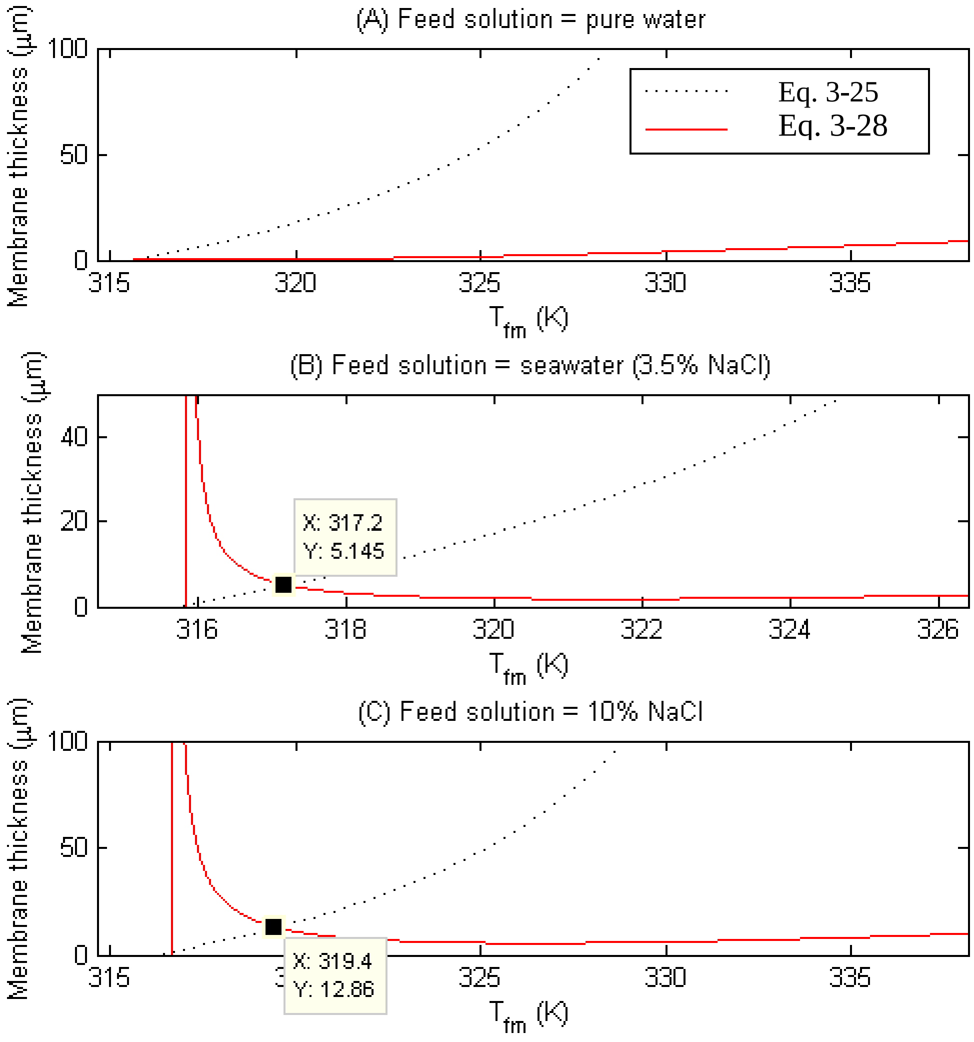

Figure 3.11 Graphical determination of optimal thickness for pure water (A, top); 3.5% NaCl solution (B, middle); and 10% NaCl solution (C, bottom). Simulation conditions are given in Table 3-3.

In Figure 3.11A, the curves obtained from Eq. 3-25 and Eq. 3-28 meet when the membrane thickness is very close to zero, in fact they meet at a thickness of 0.4 µm, as shown in Figure 3.12. When using aqueous NaCl as feed solution, Figure 3.11B and C show that value of optimal thicknesses increases with increasing salinity. With an activity coefficient of 0.98, using seawater as feed, it is estimated that the optimal thickness is about 5 microns, for the chosen simulation conditions. When using 10% NaCl as feed solution, which has an activity coefficient of 0.94, it is estimated that for the chosen simulation condition, the optimal thickness is about 13 microns. These values correspond were for $h_f = h_p = 2500$ W m^{-2} K^{-1}. For a value of a 1000 W m^{-2} K^{-1}, with other parameters unchanged the respective optimal thicknesses are 5.1 and 12.9 µm. The effect of heat transfer coefficients is discussed in more details below.

Salinity plays an important part in the determination of optimal membrane thickness. The presence of salt reduces the water vapour partial pressure in the feed through the term α_w in equationEq. 3-12. Below optimal thickness, as the membrane thickness increases the high transmembrane temperature difference results in a higher, driving force, $P_{fm} - P_{pm}$. In this region this increases more rapidly than the membrane resistance to mass transfer which increases linearly with thickness. However, above optimal thickness, the driving force increases less rapidly than the membrane resistance. For any given conditions, the value of membrane thickness corresponding to zero or negative flux is always smaller than the corresponding value for maximum flux. These values are too small to be of any practical interest; the thicknesses of commercially available membranes are about 100 microns. Indeed such thicknesses are significantly larger than the optimal thicknesses determined in Figure 3.11. Using the same procedure as described, graphical solutions are also obtained with different input values, as shown in Figure 3.12 and Figure 3.13. Figure 3.12 shows the variation of theoretical optimal thickness with respect to changes in salt concentration, under the operation conditions according to Table 3-3. It is shown that, even with aqueous NaCl solution as concentrated as 20%, the optimal thickness are much thinner than membranes available in the market.

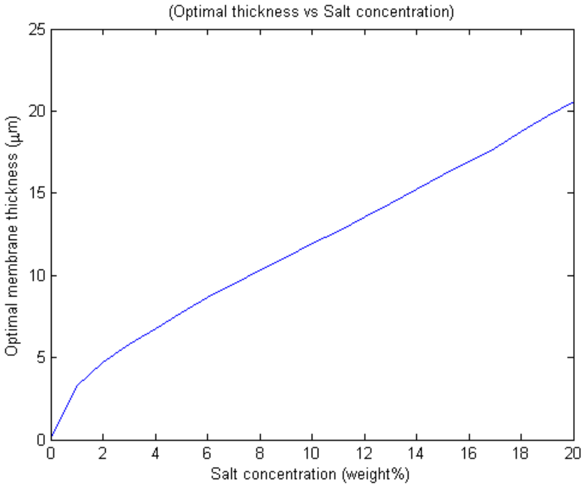

Figure 3.12 Variation of theoretical optimal thickness with respect to changes in salt concentration

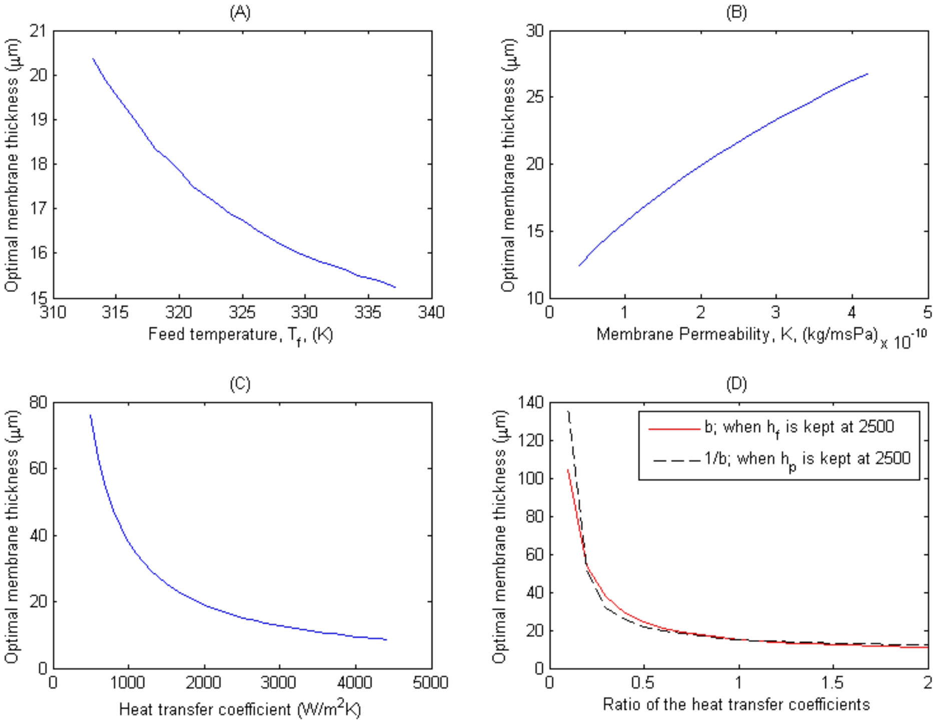

Figure 3.13 Variation in optimal thickness with changes in: (A) Feed Temperature; (B) Membrane permeability; (C) Heat transfer coefficient; (D) Ratio of permeate heat transfer coefficient to feed heat transfer coefficient. Other simulation parameters remain identical as those demonstrated in Figure 3 for 10% NaCl solution.

Figure 3.13(A) shows that the optimal membrane thickness increases by 30% for a reduction in the feed temperature from 338 K to 313 K. A lower T_f results in a lower

T_{fm}. Due to the temperature sensitivity of water vapour partial pressure, in order to achieve an effective driving force across the membrane, when the bulk feed temperature, T_f, is lowered; a thicker membrane is required to sustain a higher effective temperature difference; (and hence an effective partial pressure difference) across the membrane. From Figure 3.13(B), it can be seen that as the permeability of the membrane increases, the optimal membrane thickness increases. Owing to a higher permeate flux resulting in more heat transfer via convection; a thicker membrane is required to provide the optimal transmembrane temperature difference.

Figure 3.13(C) and (D) show that the value of optimal membrane thickness is very sensitive to the heat transfer coefficients determine the temperature polarization effect. Temperature polarization refers to the system characteristic wherein the fluid temperatures at the membrane boundaries are different to their corresponding bulk temperatures. Due to thermal boundary layer resistance, the heat transfer across the boundary layers is often the major rate determining step. With higher heat transfer coefficients on either or both sides of the membrane, the overall boundary layer resistance is reduced, giving a reduction in the temperature polarization effect. As a result, a thinner membrane would be able to provide enough relative heat transfer resistance for optimal balance between the transmembrane temperature difference (that determines the water vapour pressure difference) and the membrane resistance. Thus in Figure 3.13(C) as both h_p and h_f increase simultaneously, where $h_p = bh_f$ and b=1 (included in Eq. 3-15), the optical thickness decreases. Figure 3.13(D) shows the change in optimal thickness when only one of the heat transfer coefficients is changed. When the ratio of b is low (h_p is low and the thermal resistance at the permeate side is high), the permeate-side flow is ineffective in the transferring of heat from the membrane interface to the bulk fluid and so the consequence is that thicker membranes are required to maintain a sufficient transmembrane temperature difference, T_{fm}-T_{pm}. However the corresponding optimal thickness reduces rapidly as b increases and the steepness of the curve reduces rapidly as b approaches 1. Similar behaviour (dashed line) can be observed if h_p is kept constant and only h_f is changed. From the steepness of the curves in Figure 3.13(D), it is evident that the optimal thickness is relatively more sensitive to the change in h_f then changes in h_p.

3.4. Chapter summary

Electrospun membranes were produced by spinning from a PVDF dope. For spinning times of 2 and 3 hours, the membrane were sufficiently robust to be handled but insufficiently robust to withstand the first hour of testing. Membranes fabricated with spinning time of 4-10 hours had thickness of 27-58µm after being consolidated in a heatpress. Fluxes over 60 L/h m^2 were obtained with the 27 µm membrane when inlet feed temperature exceeded 338K. The bulk of the data lies in the range of 10-30 L/h m^2. With the introduction of structural derivation factor in our estimations, the model was found to fit the data very well including the thinner membranes operated in a system with high inlet feed temperature.

Obtaining solutions from our analytical model, it was shown that the value of optimal membrane thickness varies with salinity. In the absence of salinity, the optimal membrane thickness obtained is close to zero, at a value of 0.4µm. When the salinity is at 10%, the membrane thickness was found to be around 13µm. The values of optimal thickness were found to depend on operational conditions and the membrane properties. The value increases with lower heat transfer coefficients (especially lower feed-side heat transfer coefficients); lower feed inlet temperature; and increased membrane permeability.

It had been hoped to produce sufficiently thin membranes to demonstrate experimentally the effect of optimal thickness. However from the experimental work, it is found that such thin unsupported PVDF membranes were not robust enough. Nevertheless the excellent fit to the model suggests that the maxima at around 10 microns, shown in Figure 3.6and Figure 3.10, would be the experimental maxima if only sufficiently thin membranes had been made.

4. Mass transfer model and membrane module modelling for direct contact membrane distillation

4.1. Introduction

The first part of this chapter re-assesses, from basic kinetic theory, the common method of evaluating DCMD mass transfer by combining Knudsen diffusion coefficient and the molecular diffusion coefficient. Secondly, a re-examination of a linear mass transfer model previously proposed by Gostoli, et al. (1987) for MD is included. By expanding from the model, an equivalent effectiveness-number of heat transfer units (E-NTU) is introduced and validated for simplifying the design process of DCMD.

4.2. The reassessment of transmembrane mass transfer in DCMD

4.2.1. Use of dusty gas model (DGM) for DCMD re-visited

As reported in the literature survey, the DGM is the most widely used model for modelling transmembrane membrane mass transfer in DCMD. While a lot of the earlier literature has suggested the simultaneous presence of Poisseuille flow with Knudsen and molecular diffusion, it is necessary to emphasize that within a pore channel, Knudsen diffusion necessarily excludes the presence of Poisseuille flow according to their physical definitions: when the mean free path, Λ, of the molecule is significantly smaller (typically more than a hundred times ,Turel, 2008) than the diameter of the pore, d Poisseuille flow (viscous flow) can be assumed and the flow is treated as a continuum. On the other hand, Knudsen diffusion describes the diffusion phenomenon that occurs when the pore diameter gets smaller such that it is close to the mean free path of the molecules. The continuum (viscous) assumptions of various layers at different velocities no longer hold and molecule-wall collusions become significant. Figure 4.1 illustrates the differences between the two flows. In the figure, the velocity profiles between two plate plates: a lower stationary plate and an upper plate moving at velocity, u, for (a) d≫Λ, (b) d≈5Λ, (c) d<Λ. In panel (a), there is no slip at all adjacent to the surface of the plates while in panel (b), there is a reduced gradient, because of an effective discontinuity in the mean tangential gas velocity close to the wall. For panel (c), there is complete slip of $\frac{1}{2}$u at each surface. Considering the typical pore size of DCMD membranes, Poisseuille flow cannot be established and thus only Knudsen and molecular diffusion should be considered.

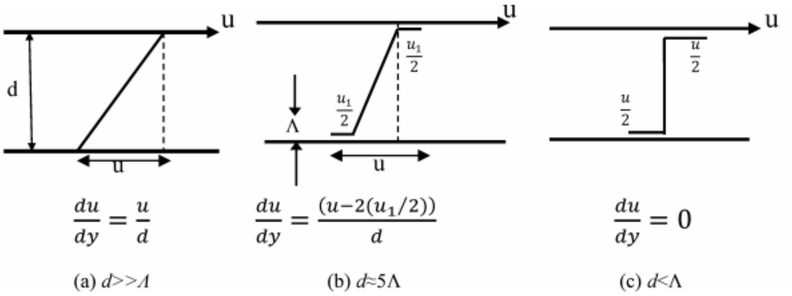

Figure 4.1 Demonstration of flow continuum and discontinuity using velocity profiles between two plates. (Adapted from (Tabor, 1991).) where in the figure, u is the velocity of the plates, d, in the same direction as y-axis, is the size of the gap between the plates.

4.2.2. Examination of combined Knudsen and molecular diffusion

Prior to examining the combined mode of diffusion, it is helpful to briefly examine the derivation of the diffusion coefficient from first principles. The coefficient of self-diffusion is expressed as (Tabor, 1991):

$$D = \frac{\bar{c}}{3\pi n\sigma^2} \qquad \text{Eq. 4-1}$$

where $\bar{c}$ is the mean speed of a gas molecule, n is the number of molecules per cubic meter, and σ^2 is the molecular cross section. The number of molecules is proportional to pressure (and inversely proportional to temperature), which is reflected in Eq. 4-3 where product of diffusion coefficient and total pressure is always taken to be a constant. Since according kinetic theory and assuming ideal gas behaviour:

$$\frac{m\bar{c}^2}{2} = \frac{3}{2}kT \qquad \text{Eq. 4-2}$$

where m is the mass of a molecule, $\bar{c}$, is the mean speed of the molecules, k is Boltzmann's constant and T is the absolute temperature of the gas. Thus, from Eq. 4-1, one would expect the diffusion coefficient, D, increases roughly to a power of 1.5 with temperature if the molecular cross section, σ^2, remains constant. (The mean speed of a gas molecule, $\bar{c}$, relates to $T^{0.5}$ according to its kinetic energy.) However, in reality the diffusion coefficient increases roughly as the 2.0 power of temperature (as clearly suggested in the empirical formula Eq. 4-3 (Mills, 2001; Phattaranawik, et al., 2003)

$$D_{w,a}^{P_T} = \frac{(1.895 \text{ x } 10^{-5})T^{2.072}}{P_T} \qquad \text{Eq. 4-3}$$

This brief inspection of Eq. 4-3and examination of the effect of temperature on diffusion coefficient prove that D is reduced by the number of molecular collisions which is determined by n and the molecular cross-section σ^2.

The traditional approach of combining Knudsen and molecular diffusion assumes that the resistances of the molecule-molecule interactions and the molecule-wall act in series with each other. However, physically, the influence of the former must be reduced as the influence of the latter increases. This work contends that at any instance a fraction of molecules, θ, is moving through a pore by Knudsen diffusion, then only a fraction of $1-\theta$ is experiencing molecule-molecule interactions.

Consequently, the effective molecular diffusion coefficient in this case should be given as:

$$D_{w,a}^{act.} = \frac{D_{w,a}^{P_T}}{(1-\theta)} \qquad \text{Eq. 4-4}$$

which $D_{w,a}^{act.}$ denotes the actual molecular diffusion coefficient.

To determine an expression for θ, we assume random Brownian motion of the particles and considering the distance between molecules and the distance between a molecule and the walls of the porous structure. Then an approximation of θ can be expressed as:

$$\theta = \frac{\Lambda}{d+\Lambda} \qquad \text{Eq. 4-5}$$

Now given Knudsen number, Kn, is defined as $\frac{\Lambda}{d}$; Eq. 4-5 can be rewritten and rearranged to:

$$\frac{1}{1-\theta} = 1 + \mathrm{Kn} \qquad \text{Eq. 4-6}$$

By incorporating Eq. 4-4 and Eq. 4-6 into Eq. 2-19 the result is Eq. 4-7:

$$\frac{J_w^D}{D_{Kw}} + \frac{p_a(1+\mathrm{Kn})J_w^D}{D_{w,a}^{P_T}} = -\frac{1}{RT}\nabla p_w \qquad \text{Eq. 4-7}$$

Its integration yields the refined transmembrane flux expression:

$$N = \frac{(\varepsilon/\tau)P_T\,(1+\mathrm{Kn})D_{w,a}^{P_T}}{\delta RT_m}.\ln\left[\frac{D_{Kw}.y_{apm} + (1+\mathrm{Kn})D_{w,a}^{P_T}}{D_{Kw}.y_{afm} + (1+\mathrm{Kn})D_{w,a}^{P_T}}\right] \qquad \text{Eq. 4-8}$$

The main point for this section is to suggest the notion that while both Knudsen and molecular diffusions take place simultaneously through the pore, allowance is needed for that fact that the fraction of molecules that are colliding with the channel wall (experiencing Knudsen diffusion), are not involved simultaneously involved in molecule-molecule interactions. This has recently been recognised by others like Essalhi (Essalhi & K hayet, 2013) but was first proposed in (Field, et al., 2013). Below we use experimentally determined value from literature (Song et al. 2007) for membrane coefficient but if one wanted to explore theoretically the question of the effect of pore size upon performance then the balance between Knudsen and molecular diffusion should be handled appropriately.

4.3. A linear model for DCMD and an overall mass transfer coefficient

Gostoli, Sarti and Matulli (1987) proposed a linear mass transfer model for DCMD which is suitable for dilute solutions and for sufficiently small temperature differences across the membrane:

$$\mathrm{N} = \mathrm{K}''(\Delta\mathrm{T} - \Delta\mathrm{T}^{\mathrm{BP}}) \qquad \text{Eq. 4-9}$$

where K” is the flux of water vapour through the membrane per unit of temperature difference across the membrane. K” is a membrane property. ΔT is the transmembrane temperature difference, T_{fm}-T_{pm}, $\Delta\mathrm{T}^{\mathrm{BP}}$ is the temperature change in boiling point due salinity. Additionally when the bulk temperature difference, $\Delta\mathrm{T}_{\mathrm{b}}$, is considered they defined:

$$\mathrm{N} = \mathrm{K}_{\mathrm{eff}}(\Delta\mathrm{T}_{\mathrm{b}} - \Delta\mathrm{T}_{\mathrm{b}}^{\mathrm{BP}}) \qquad \text{Eq. 4-10}$$

For ease of exposition and given the focus on this work is on brackish water, $\Delta\mathrm{T}_{\mathrm{b}}^{\mathrm{BP}}$is approximated to 0 due to the low NaCl concentration.

Recalling the four MD governing equations Eq. 2-1-Eq. 2-4 in Section 2.1.1, combing Eq. 2-1and Eq. 2-2 gives:

$$q\left(\frac{1}{h_f}+\frac{1}{h_p}\right) = (\Delta T_b - \Delta T) \qquad \text{Eq. 4-11}$$

By defining a combined heat transfer coefficient, U_L :

$$U_L = \left(\frac{1}{h_f}+\frac{1}{h_p}\right)^{-1} \qquad \text{Eq. 4-12}$$

and substituting Eq. 4-9 - Eq. 4-12 into Eq. 2-3one obtains:

$$\frac{(\Delta T_b - \Delta T)}{U_L} = K_{eff}\Delta T_b\lambda + \frac{k_m}{\delta}\Delta T \qquad \text{Eq. 4-13}$$

Eq. 4-9 and Eq. 4-10 can be used to eliminate, ΔT, and after rearrangement, the expression for K_{eff} is given by:

$$K_{eff} = \frac{K''}{\delta + \frac{k_m}{U_L} + \frac{\lambda K''}{U_L}} \qquad \text{Eq. 4-14}$$

K_{eff}, is seen to depend on both the hydrodynamics, which affect U_L and membrane properties. Generally this is obtained experimentally, but can be estimated when the membrane permeability, K* or K" (with the unit of kg $m^{-1}s^{-1}Pa^{-1}$ or kg $m^{-1}s^{-1}K^{-1}$ respectively) and the heat transfer coefficients are known. A good estimation of K_{eff} is given as follow:

The transmembrane flux is driven the difference in vapour partial pressure and because of the non-linearity of vapour partial pressure and temperature, the value of K"changes as the temperatures change. By comparing Eq. 4-9 and Eq. 2-11, it is deduced that:

$$K'' = K^*\frac{dP}{dT} \qquad \text{Eq. 4-15}$$

where the value of K* solely dependent on the properties of the hydrophobic membrane. By fitting a forth order polynomial to Antoine equation in the temperature range 290 to 340K, the water vapour partial pressure and its differential with respect to temperature can be expressed as the following:

$$P = 0.00093687T^4 - 1.059T^3 + 452.75T^2 - 86690T + 6267900 \qquad \text{Eq. 4-16}$$

and differentiation gives:

$$\frac{dP}{dT} = 0.00374738T^3 - 3.177T^2 + 905.5T - 86690 \qquad \text{Eq. 4-17}$$

Thus K" can be evaluated for any temperature range when the value of K* is known using Eq. 4-18.

$$K'' = \frac{K^*}{2}\left(\left.\frac{dP}{dT}\right|_{T_f} + \left.\frac{dP}{dT}\right|_{T_p}\right) \qquad \text{Eq. 4-18}$$

Finally, using K", $K_{eff,}$ is computed using Eq. 4-14.

4.4. Effectiveness- Number of Transfer Units for DCMD

4.4.1. Derivations of modified E-NTU expressions

As noted in Section 2.4.2 that mass transfer models based on the effectiveness-Number of Transfer Units (E-NTU) have been introduced recently for mass transfer membrane system, namely, RO and PRO. This work proposes a model that estimates the performance of DCMD modules with a modified E-NTU method using the linear model and overall mass transfer coefficient derived in the previous section. In the original application for E-NTU, the overall heat transfer coefficient, U, is defined and given as:

$$U = \frac{Q}{\Delta T} = \left(\frac{\delta}{k_m} + \frac{1}{h_p} + \frac{1}{h_f}\right)^{-1} \qquad \text{Eq. 4-19}$$

In the case of DCMD, the overall heat transfer coefficient, α, can be found by substituting Eq. 4-11 and Eq. 4-12 into Eq. 4-13, rearrangement yields:

$$q = \alpha\left(T_f - T_p\right) \qquad \text{Eq. 4-20}$$

where

$$\alpha = \left(\frac{K_{eff}\lambda + \frac{k_m}{\delta}}{1 + \frac{k_m}{\delta h_p} + \frac{k_m}{\delta h_f}}\right) \qquad \text{Eq. 4-21}$$

$$= U\left(1 + \frac{K_{eff}\lambda}{\frac{k_m}{\delta}}\right) \qquad \text{Eq. 4-22}$$

For the derivation of the E-NTU expressions, conservation of energy detemines the temperature changes in the feed and permeate flows along the module. It follows that as:

$$dT_f = \frac{-q dA}{\dot{m}_f c_f} \qquad \text{Eq. 4-23}$$

$$dT_p = \frac{q dA}{\dot{m}_p c_p} \qquad \text{Eq. 4-24}$$

and combining Eq. 4-23 and Eq. 4-24 yields the following differential equation:

$$\frac{d(T_f - T_p)}{dA} = -\,\alpha\left(T_f - T_p\right)\left(\frac{1}{\dot{m}_f c_f} + \frac{1}{\dot{m}_p c_p}\right) \qquad \text{Eq. 4-25}$$

Using the boundary conditions given Table 4-1, a set of suitable E-NTU expressions for DCMD are obtained and these are shown in Table 4-2 and

Table 4-3 for countercurrent and cocurrent flows respectively. In the tables, for the standard heat exchanger hot and cold streams are referred, and for DCMD to feed and permeate streams. Do note that capital C's refer to heat capacity rate (the product of mass flowrate and specific heat capacity) as is standard in E-NTU analysis. In the case of DCMD, both feed and permeate have similar fluid properties and the specific heat capacities c_f and c_p are approximately equal.

Table 4-1 Boundry conditions for the integration of Eq. 4-25

Cocurrent flow:	
At A = 0	$T_f - T_p = T_{f,in} - T_{p,in}$
A= A_1	$T_f - T_p = T_{f,out} - T_{p,out}$
Countercurrent flow:	
At A = 0	$T_f - T_p = T_{f,in} - T_{p,out}$
A= A_1	$T_f - T_p = T_{f,out} - T_{p,in}$

where A denotes accumulated membrane surface area along the streamwise diresction and A_1 is assigned here as the total membrane area

Table 4-2 Comparison of E-NTU expressions, in countercurrent flow configuration, between the conventional case and the modified case for DCMD.

Flow condition	Conventional E-NTU	Modified E-NTU for DCMD
$m_{h,in}C_h > m_{c,in}C_c$ $m_{f,in}C_f > m_{p,in}C_p$ Countercurrent flow	$E = \frac{Q}{Q_{max}}$ $= \frac{C_h\left(T_{h,in} - T_{h,out}\right)}{C_c\left(T_{h,in} - T_{c,in}\right)} = \frac{C_c\left(T_{c,out} - T_{c,in}\right)}{C_c\left(T_{h,in} - T_{c,in}\right)}$ $C_r = \frac{C_{min}}{C_{max}} = \frac{\dot{m}_{c,in}\,c_c}{\dot{m}_{h,in}\,c_h}$ $NTU = \left(\frac{UA}{C_{min}}\right) = \left(\frac{UA}{C_c}\right)$ $E = \frac{1 - \exp\left[(-NTU)(1 - C_r)\right]}{1 - C_r\exp\left[(-NTU)(1 - C_r)\right]}$	$E = \frac{Q}{Q_{max}} = \frac{C_f\left(T_{f,in} - T_{f,out}\right)}{C_{min}\left(T_{f,in} - T_{p,in}\right)} = \frac{T_{p,out} - T_{p,in}}{T_{f,in} - T_{p,in}}$ $C_r = \frac{C_{min}}{C_{max}} = \frac{\dot{m}_{p,in}\,c_p}{\dot{m}_{f,in}\,c_f} = \frac{T_{f,in} - T_{f,in}}{T_{p,out} - T_{p,in},} = \frac{C_p}{C_f}$ $NTU = \left(\frac{\alpha A_1}{C_p}\right) = \left(\frac{K_{eff}\lambda + \frac{k_m}{\delta}}{1 + \frac{k_m}{\delta h_p} + \frac{k_m}{\delta h_f}}\right)\left(\frac{A_1}{C_p}\right)$ $E = \frac{1 - \exp\left[(-NTU)(1 - C_r)\right]}{1 - C_r\exp\left[(-NTU)(1 - C_r)\right]}$
$m_{c,in}C_c > m_{h,in}C_h$ $m_{p,in}C_p > m_{f,in}C_f$ Countercurrent flow	$E = \frac{Q}{Q_{max}}$ $= \frac{C_h\left(T_{h,in} - T_{h,out}\right)}{C_h\left(T_{h,in} - T_{c,in}\right)} = \frac{C_c\left(T_{c,out} - T_{c,in}\right)}{C_h\left(T_{h,in} - T_{c,in}\right)}$ $C_r = \frac{C_{min}}{C_{max}} = \frac{\dot{m}_{h,in}\,c_h}{\dot{m}_{c,in}\,c_c}$ $NTU = \left(\frac{UA}{C_{min}}\right) = \left(\frac{UA}{C_h}\right)$ $E = \frac{1 - \exp\left[(-NTU)(1 - C_r)\right]}{1 - C_r\exp\left[(-NTU)(1 - C_r)\right]}$	$E = \frac{Q}{Q_{max}} = \frac{C_p\left(T_{p,out} - T_{p,in}\right)}{C_{min}\left(T_{f,in} - T_{p,in}\right)} = \frac{T_{f,in} - T_{f,out}}{T_{f,in} - T_{p,in}}$ $C_r = \frac{C_{min}}{C_{max}} = \frac{\dot{m}_{f,in}\,c_f}{\dot{m}_{p,in}\,c_p} = \frac{T_{p,out} - T_{p,in}}{T_{f,in} - T_{f,out}} = \frac{C_f}{C_p}$ $NTU = \left(\frac{\alpha A_1}{C_f}\right) = \left(\frac{K_{eff}\lambda + \frac{k_m}{\delta}}{1 + \frac{k_m}{\delta h_p} + \frac{k_m}{\delta h_f}}\right)\left(\frac{A_1}{C_f}\right)$ $E = \frac{1 - \exp\left[(-NTU)(1 - C_r)\right]}{1 - C_r\exp\left[(-NTU)(1 - C_r)\right]}$

Table 4-3 Comparison of E-NTU expressions, in cocurrent flow configuration, between the conventional case and the modified case for DCMD.

Flow condition	Conventional E-NTU	Modified E-NTU for DCMD
$m_{h,in}C_h > m_{c,in}C_c$ **$m_{f,in}C_f > m_{p,in}C_p$** Cocurrent flow	$E = \frac{Q}{Q_{max}}$ $= \frac{C_h\left(T_{h,in} - T_{h,out}\right)}{C_c\left(T_{h,in} - T_{c,in}\right)} = \frac{C_c\left(T_{c,out} - T_{c,in}\right)}{C_c\left(T_{h,in} - T_{c,in}\right)}$ $C_r = \frac{C_{min}}{C_{max}} = \frac{\dot{m}_{c,in}\, c_c}{\dot{m}_{h,in}\, c_h}$ $NTU = \left(\frac{UA}{C_{min}}\right) = \left(\frac{UA}{C_c}\right)$ $E = \frac{1 - \exp\left[(-NTU)(1 + C_r)\right]}{1 + C_r}$	$E = \frac{Q}{Q_{max}} = \frac{C_f\left(T_{f,in} - T_{f,out}\right)}{C_{min}\left(T_{f,in} - T_{p,in}\right)} = \frac{T_{p,out} - T_{p,in}}{T_{f,in} - T_{p,in}}$ $C_r = \frac{C_{min}}{C_{max}} = \frac{\dot{m}_{p,in}\, c_p}{\dot{m}_{f,in}\, c_f} = \frac{T_{f,in} - T_{f,out}}{T_{p,out} - T_{p,in}} = \frac{C_p}{C_f}$ $NTU = \left(\frac{\alpha A_1}{C_p}\right) = \left(\frac{K_{eff}\lambda + \frac{k_m}{\delta}}{1 + \frac{k_m}{\delta h_p} + \frac{k_m}{\delta h_f}}\right)\left(\frac{A_1}{C_p}\right)$ $E = \frac{1 - \exp\left[(-NTU)(1 + C_r)\right]}{1 + C_r}$
$m_{c,in}C_c > m_{h,in}C_h$ **$m_{p,in}C_p > m_{f,in}C_f$** Cocurrent flow	$E = \frac{Q}{Q_{max}}$ $= \frac{C_h\left(T_{h,in} - T_{h,out}\right)}{C_h\left(T_{h,in} - T_{c,in}\right)} = \frac{C_c\left(T_{c,out} - T_{c,in}\right)}{C_h\left(T_{h,in} - T_{c,in}\right)}$ $C_r = \frac{C_{min}}{C_{max}} = \frac{\dot{m}_{h,in}\, c_h}{\dot{m}_{c,in}\, c_c}$ $NTU = \left(\frac{UA}{C_{min}}\right) = \left(\frac{UA}{C_h}\right)$ $E = \frac{1 - \exp\left[(-NTU)(C_r + 1)\right]}{1 + C_r}$	$E = \frac{Q}{Q_{max}} = \frac{C_p\left(T_{p,out} - T_{p,in}\right)}{C_{min}\left(T_{f,in} - T_{p,in}\right)} = \frac{T_{f,in} - T_f}{T_{f,in} - T_{p,in}}$ $C_r = \frac{C_{min}}{C_{max}} = \frac{\dot{m}_{f,in}\, c_f}{\dot{m}_{p,in}\, c_p} = \frac{T_{p,out} - T_{p,in}}{T_{f,in} - T_{f,out}} = \frac{C_f}{C_p}$ $NTU = \left(\frac{\alpha A_1}{C_f}\right) = \left(\frac{K_{eff}\lambda + \frac{k_m}{\delta}}{1 + \frac{k_m}{\delta h_p} + \frac{k_m}{\delta h_f}}\right)\left(\frac{A_1}{C_f}\right)$ $E = \frac{1 - \exp\left[(-NTU)(1 + C_r)\right]}{1 + C_r}$

4.4.2. Applications of the new E-NTU expressions for DCMD

From the set of modified E-NTU expressions for DCMD one can straightforwardly determine either the stream outlet temperatures when the module size is known, or the membrane area required for the desired overall heat transfer across the membrane. However as the estimation of the value of transmembrane flux is of primary concern and the main performance indicator in MD systems it is important that design tools can (i) determine the overall permeate production of a given DCMD membrane module and (ii) estimate the size a module given a desired production rate. To achieve (i) and (ii), an accurate estimation of the membrane module thermal efficiency, $\eta_{mod.}$, is required as:

$$\dot{m}_{production} = \frac{Q\eta_{mod.}}{\lambda} \qquad \text{Eq. 4-26}$$

Typically, the thermal efficiency of a DCMD module is given by:

$$\eta = \frac{N\lambda}{Q} \qquad \text{Eq. 4-27}$$

and substituting Eq. 4-9, Eq. 4-20 and Eq. 4-21 into Eq. 4-27 gives:

$$\eta = \frac{K_{eff}\lambda(1 + \frac{k_m}{\delta h_p} + \frac{k_m}{\delta h_f})}{K_{eff}\lambda + \frac{k_m}{\delta}} \qquad \text{Eq. 4-28}$$

Since η varies along the module, a more accurate estimation or the overall module efficiency, $\eta_{mod.}$, can be obtained by taking the average of the η obtained at the both ends when the outlet temperatures could be calculated or estimated.

Figure 4.2 and Figure 4.3show respectively the algorithms to rate and size a DCMD module using the E-NTU expressions. It is shown in Figure 3 that in order to validate the calculation of the membrane area needed for the specified amount of permeate, there is an extra step which verifies whether such demand is possible for the operating conditions supplied. This step is the one checks whether $Q_{max} > Q_{req}$. FromEq. 4-26, the heat required is given by:

$$Q\text{-}_{req.} = \frac{\dot{m}_{producion}\lambda}{\eta} \qquad \text{Eq. 4-29}$$

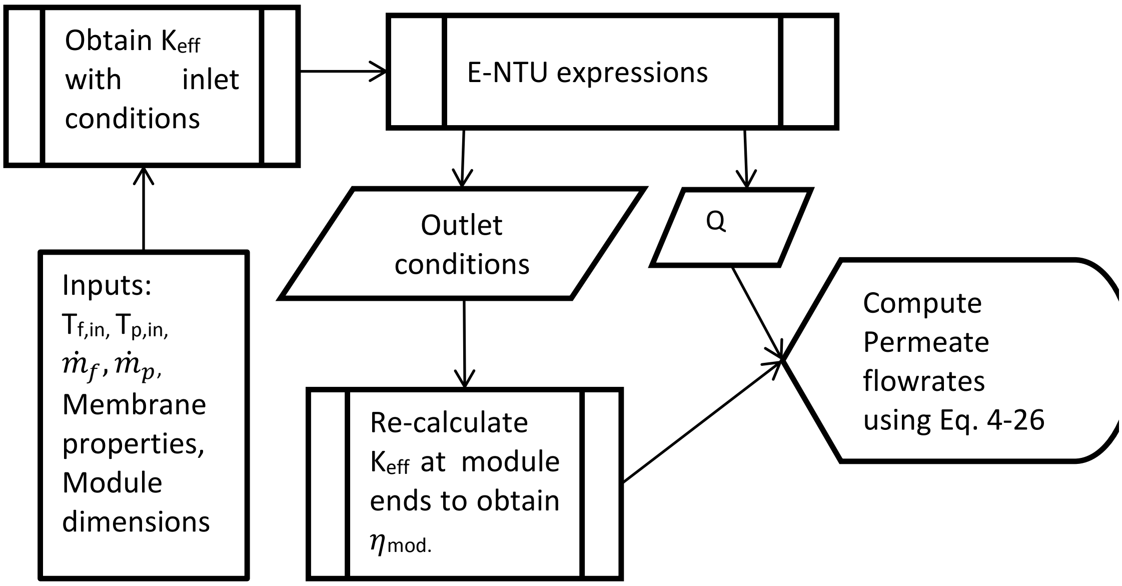

Figure 4.2 Flowchart for DCMD 'rating' calculations. The E-NTU method is used to obtain the permeate flowrates given inputs that include membrane area.

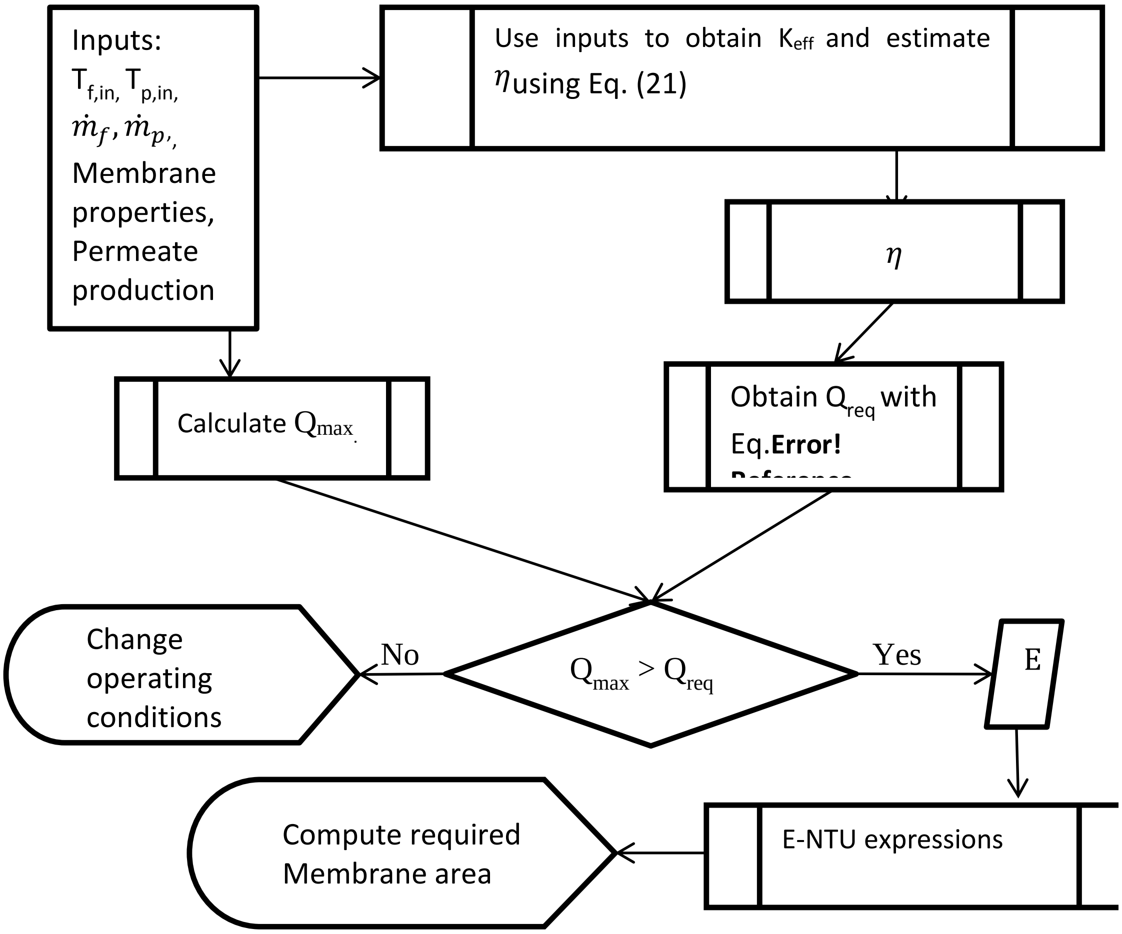

Figure 4.3 Flowchart for DCMD design calculations; using the E-NTU method to obtain the required membrane area for specified production rate.

4.4.3. Model validation – without correction factor

In order to assess and identify the accuracy and reliability region of the proposed E-NTU model, the data from the E-NTU method is compared with the simulated result obtained from the MATLAB discretised counter-current flat sheet module (described in Section 3.2.4 of this thesis). Various feed and permeate flowrates, membrane properties and the module geometries were investigated, including membrane permeability, module channel geometry, mass flow rate and permeate to feed flowrate ratio. The simulation conditions are referred and compared to a base case defined by the values given in Table 4-4.

Table 4-4 List of values used for the base case simulation

Parameters for base case	Assigned value
Membrane permeability, K_0	$8.6\text{x}10^{-7}$ kg $m^{-1}s^{-1}$ Pa^{-1}
Height (gap) of the feed channel, G_{f0}	$3\ \text{x}10^{-3}$ m
Height of the permeate channel, G_{p0}	$3\ \text{x}10^{-3}$ m
Feed flowrate, $\dot{m}_{f0}$	0.025 kg s^{-1}
Permeate flowrate, $\dot{m}_{p0}$	0.025 kg s^{-1}
Feed inlet temperature, T_{fin}	358 K
Permeate inlet temperature, T_{pin}	298 K

Both the feed and permeate channels has a width of 10 cm (depicted in Figure 4.4). For both of the models, the heat transfer coefficient is calculated using Eq. 4-30, given in (Rathore & Kapuno, Jr., 2009), for laminar flow in channels:

$$h = \frac{k}{D} 0.332 Re^{\frac{1}{2}} Pr^{\frac{1}{3}} \qquad \text{Eq. 4-30}$$

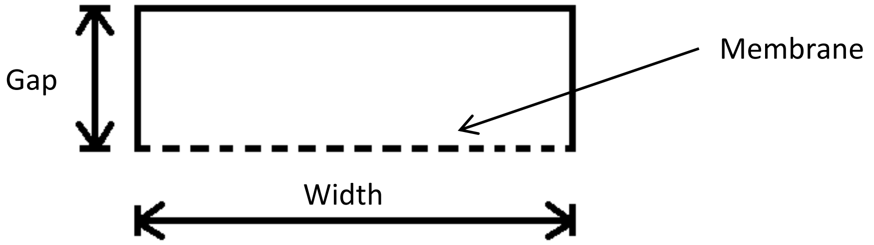

Figure 4.4 Drawing of the cross section of one of the membrane channel

The comparisons between the results obtained from Matlab discretized model and the E-NTU model are shown in Figure 4.5 - Figure 4.8 for co-current configuration.

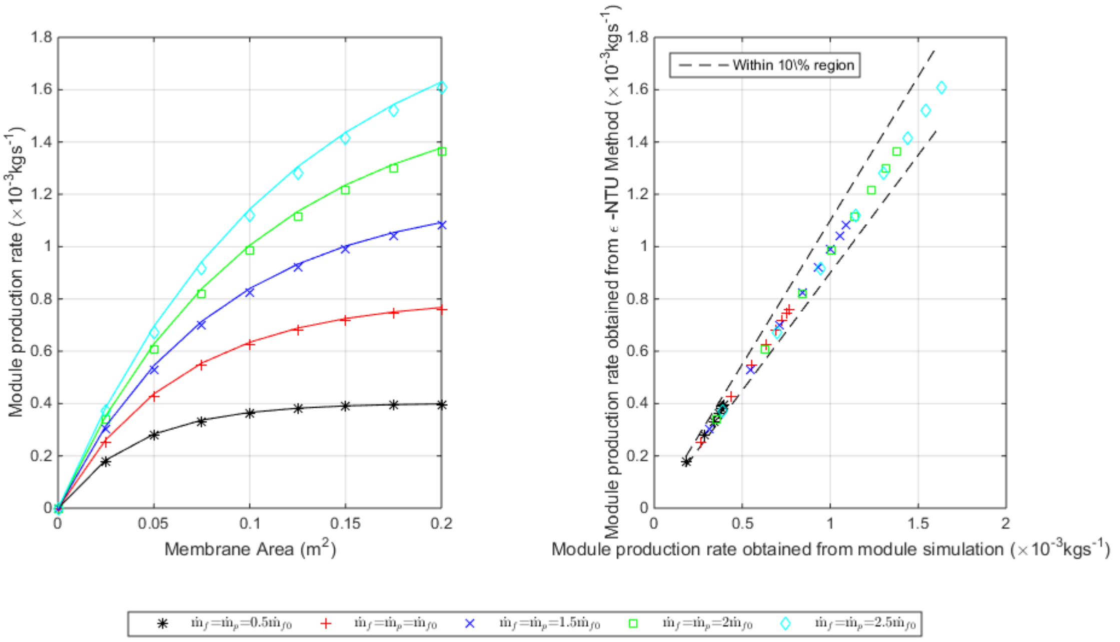

Figure 4.5 (A-left) and (B-right) Evaluation of E-NTU method for co-current flow: variation of module production rate with membrane area for various mass flowrates. Solid lines are simulated result obtained from MATLAB discretised DCMD module.

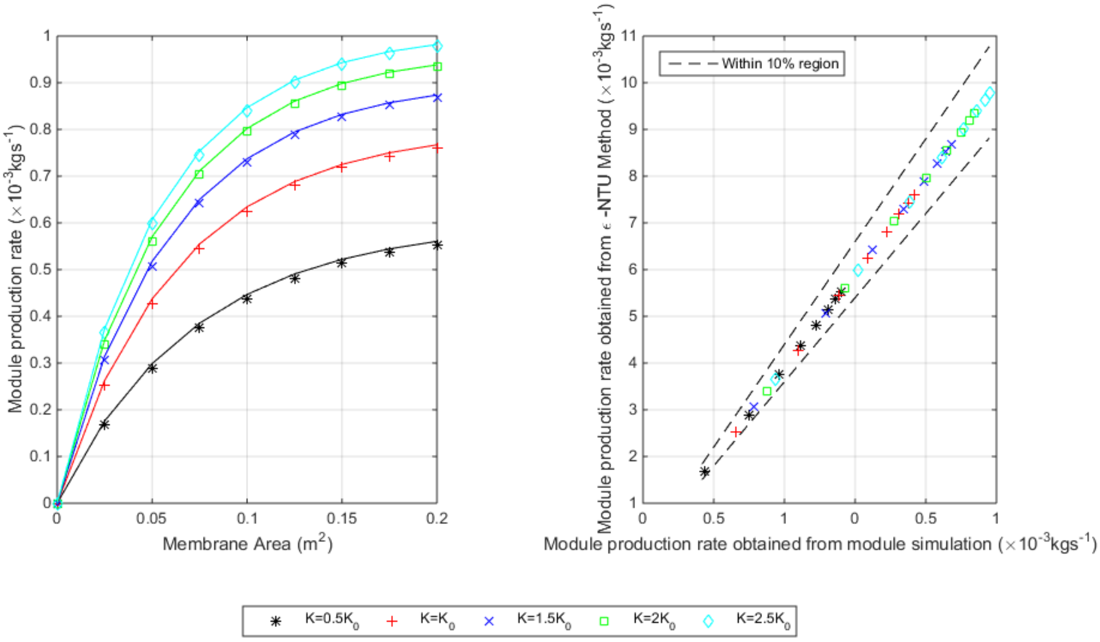

Figure 4.6 (A-left) and (B-right) Evaluation of E-NTU method for co-current flow: variation of module production rate with membrane area with changing membrane permeability. Solid lines are simulated result obtained from MATLAB discretised DCMD module.

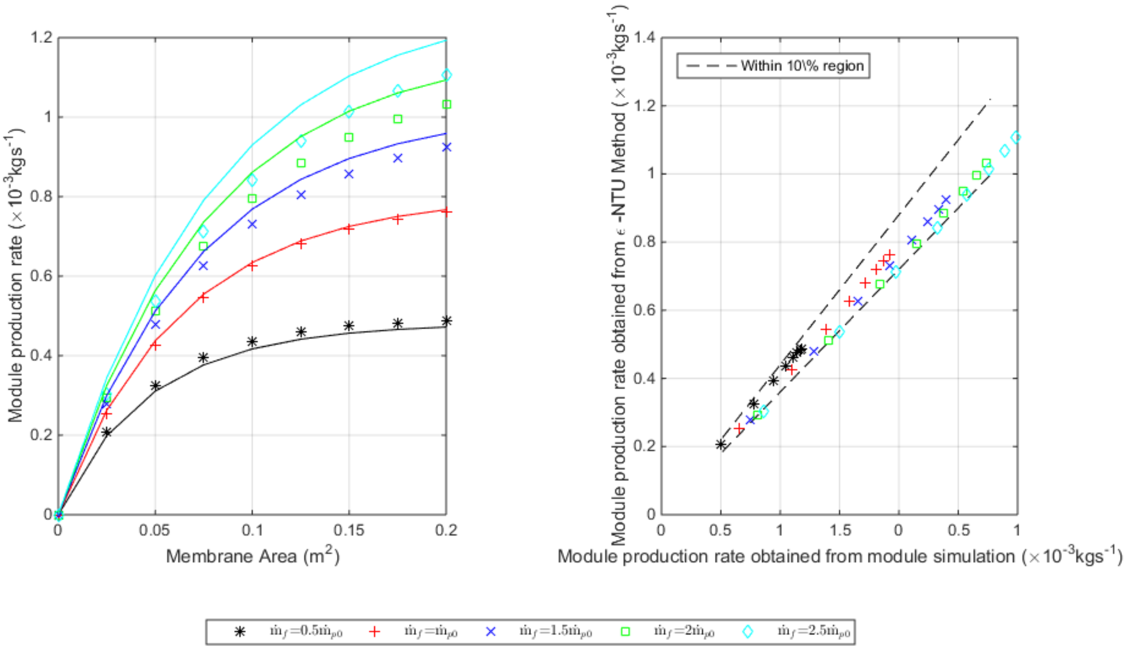

Figure 4.7 (A-left) and (B-right) Evaluation of E-NTU method for co-current flow: variation of module production rate with membrane area with changing feed to permeate ratio. Solid lines are simulated result obtained from MATLAB discretised DCMD module.

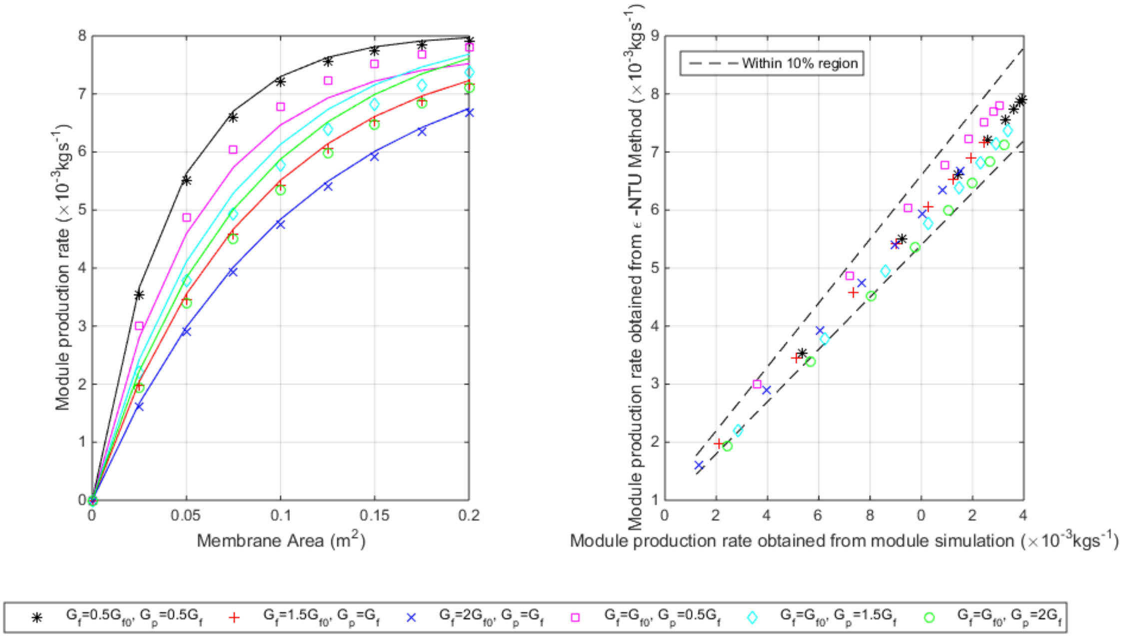

Figure 4.8 (A-left) and (B-right) Evaluation of E-NTU method for co-current flow: variation of module production rate with membrane area with changing channel dimensions. Solid lines are simulated result obtained from MATLAB discretised DCMD module.

It is evident from Figure 4.5 and Figure 4.6 show that the accuracy of our E-NTU model is not affected by either changes in mass flowrates (the ratio of feed side to permeate side is kept constant at 1:1) or by changes in membrane permeability. In Figure 4.5A and Figure 4.6A one can see that the E-NTU model gives a very minor but consistent underestimation compared to the result obtained from MATLAB simulation. This assessment is confirmed by Figure 4.5B and Figure 4.6B with all the data points almost aligned along the diagonal on the graph.

It is evident from Figure 4.7A and B that the E-NTU model becomes less accurate as the ratio of feed to permeate flowrate increases. The level of underestimation becomes more significant with increasing ratio of m_f to m_p. On the other hand, overestimation is evidential when the ratio of m_f to m_p is below one. This observation can be explained by examining the derivation of the model. As shown in Eq. 4-12, h_f and h_p are combined using a straight forward, resistance-based approach. This way of combining h_f and h_p into $U_L$means that our model is insensitive to the location of the individual values of the two heat transfer coefficients. The ratio between h_f and h_p increases with increase in the ratio of feed to permeate flowrates. In the case of m_f being 2.5 times of m_p (in Figure 4.7A and B), h_f is 1.5 times the value of $h_{p.}$ While literature (Lawsob & Lloryd, 1997; Alklaibi & Lior, 2005; Khayet, 2011)has stated that the rate of heat transfer in the feed stream affects the performance of MD systems more significantly compared to the rate of heat transfer the permeate stream, this is not captured in the derivation of our model. The same reason can be used to explain Figure 4.8A and B. As the membrane module becomes more non-symmetrical as the flow channels' dimensions change, the change in hydraulic diameter and flow velocity alter the corresponding heat transfer coefficients. This results in the E-NTU model becomes less accurate with a more severe level of underestimations when h_f is significantly higher than h_p, but the predictions are still within or very close to the 10% region.

For the countercurrent configuration, the comparisons between the E-NTU model and the results obtained from our discretization model are shown in Figure 4.9 - Figure 4.12. Similar to the case of cocurrent flow, there are some offsets, as demonstrated in Figure 4.9 and Figure 4.10, however the general level of accuracy remains high but not as high.

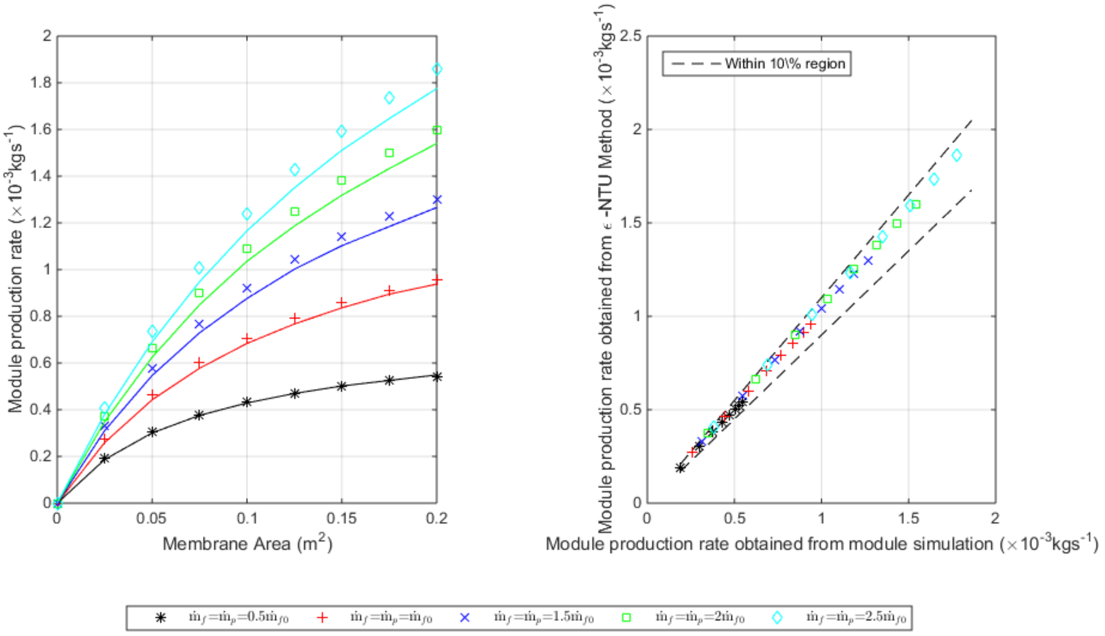

Figure 4.9 (A-left) and (B-right) Evaluation of E-NTU method for countercurrent flow: variation of module production rate with membrane area for various mass flowrates. Solid lines are simulated result obtained from MATLAB discretised DCMD module.

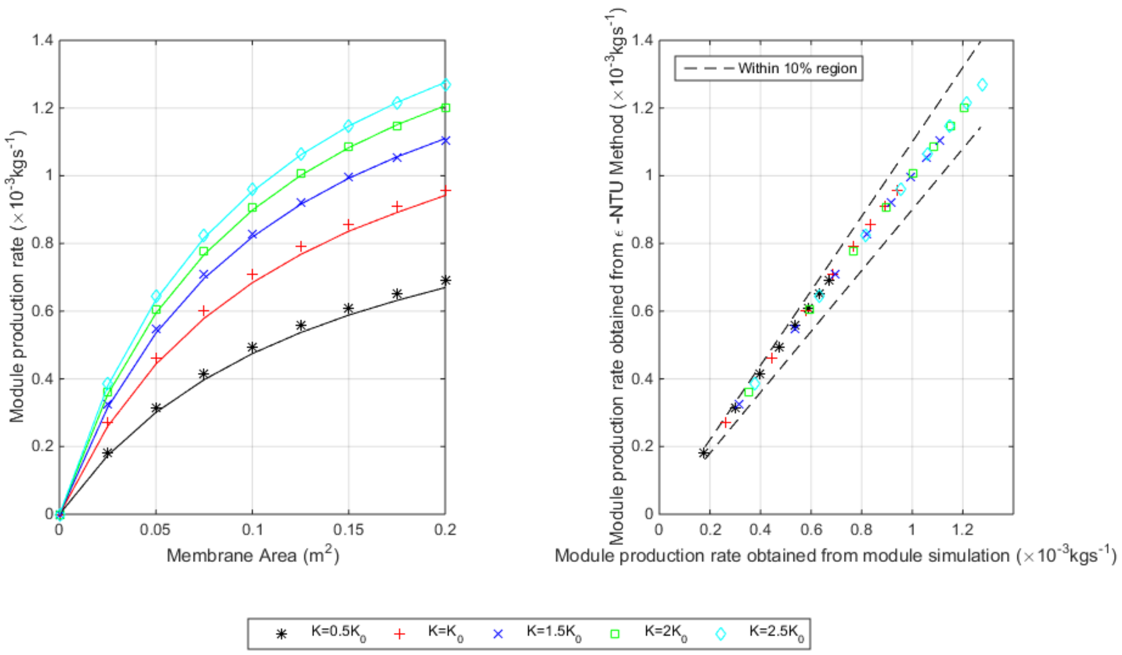

Figure 4.10 (A-left) and (B-right) Evaluation of E-NTU method for countercurrent flow: variation of module production rate with membrane area with changing membrane permeability. Solid lines are simulated result obtained from MATLAB discretised DCMD module.

Unlike the cocurrent configuration, overestimations are observed at the base case of countercurrent flow configuration. Moreover the offset becomes more apparent as the mass flowrate increases. In concurrent system, due to the symmetry of the flow and the module, the axial variation of the membrane temperature is considerably small. However in countercurrent flow there is an axial variation in membrane temperature between the hotter and cooler end of the modules, resulting in a higher variation of K_{eff} and η along the module. Thus an average thermal efficiency using only the inlet and outlet temperatures poses a more apparent inaccuracy. As the non-linear relationship between vapour partial pressure and temperature results in the vapour pressure falling rapidly when the temperature drops, the model tends to overestimate the thermal efficiency in countercurrent flow. Nonetheless the results obtained lie comfortably within the 10% percentage error region.

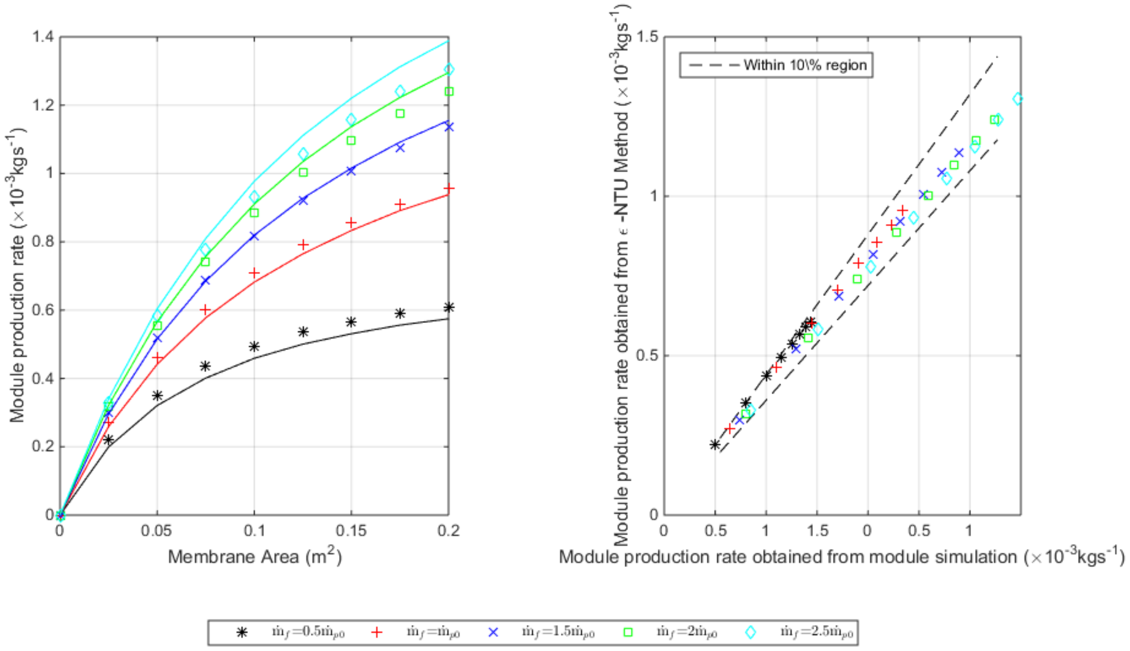

Figure 4.11 (A-left) and (B-right) Evaluation of E-NTU method for countercurrent flow: variation of module production rate with membrane area with changing feed to permeate ratio. Solid lines are simulated result obtained from Matlab discretised DCMD module.

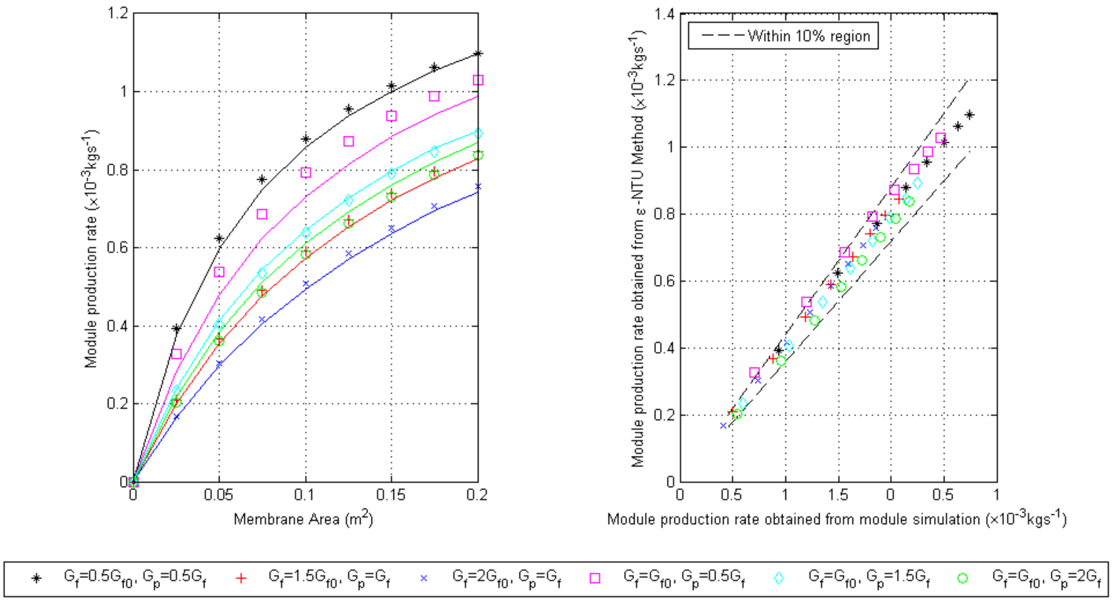

Figure 4.12 (A-left) and (B-right) Evaluation of E-NTU method for countercurrent flow: variation of module production rate with membrane area with changing channel dimensions. Solid lines are simulated result obtained from Matlab discretised DCMD module.

Similar to the reasoning suggested for the case of cocurrent flow, Figure 4.11 and Figure 4.12 show that the accuracy of the E-NTU model changes when the difference between h_f and h_p becomes more significant. As noted previously the rate of heat transfer in the feed stream affects the performance of MD systems more significantly compared to the rate of heat transfer in the permeate stream. When h_p is higher than h_f in the case of countercurrent flow (i.e. the thermal resistance on the feedside is relatively higher), the inaccuracy of overestimation becomes more significant (as evidenced in the asterisk markers in Figure 4.11B and square markers in Figure 4.12B). In the case when h_f is significantly higher than h_p, the E-NTU model starts to underestimate the module production rate as shown in Figure 4.11A and B.

Figure 4.13 assesses all the data shown in Figure 4.7 -Figure 4.12. It shows the percentage difference between the discretization model and the discretised model for varying ratio of the heat transfer coefficients. It is suggested that the accuracy of our proposed E-NTU model depends on the ratio of h_f and h_p such that as the ratio increases to well above 1, the level of underestimation increases while when the ratio is below one, overestimating is observed. Given that no correction factors have been applied, the overall accuracy of our E-NTU model is very good with 95% of our data points lying well within the 10% accuracy region.

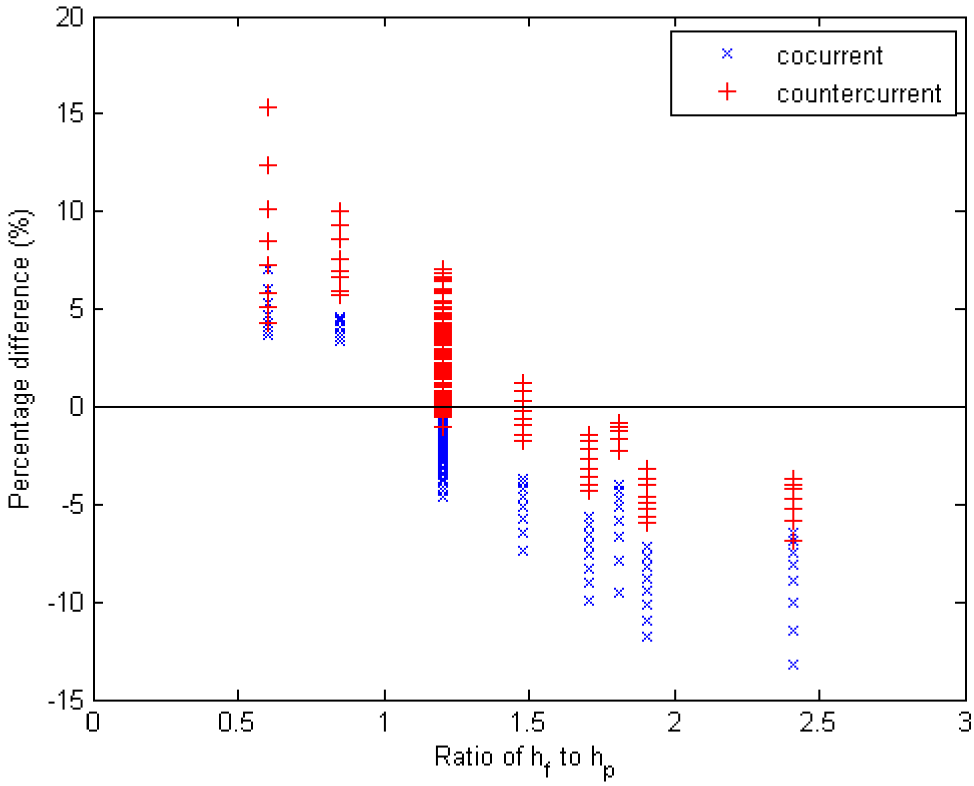

Figure 4.13 Percentage difference between discretization model and the E-NTU model with varying ratio of the heat transfer coefficients.

4.4.4. Correction factor, ξ

A correction factor is introduced to further improve the proposed model, aiming to reduce the error due to consistent offset and the model's insensitivity to the location of the individual values of the two heat transfer coefficients. It is proposed here that the expression of the correction factor is in the form:

$$\xi = \text{Ж}_1 \left(\frac{h_f}{h_p}\right)^{\text{Ж}_2} \tag{Eq. 4-31}$$

where Ж_1 and Ж_2 are constant to be found and the correction factor is to be incorporated into the model as shown in Eq. 4-32. The correction factor for heat transfer correlations provided by Sieder and Tate (Field, 1990) takes the form $(\mu_b/\mu_w)^{0.14}$, the bulk and wall viscosity respectively, and Eq. 4-31 is of a similar nature.

$$\dot{m}_{production} = \frac{Q\eta_{mod.}}{\lambda}\xi \qquad \text{Eq. 4-32}$$

Consider the offset generated by the E-NTU model in the base case by both configuration where the ratio of heat transfer coefficient is unity. A very slight underestimation is observed in concurrent flow while an overestimation is observed in countercurrent flow. Using Excel Solver Application, and only data shown in Figure 4.5 and Figure 4.6 for concurrent flow, and data shown in Figure 4.9 and Figure 4.10 for countercurrent flow $Ж_1$ is found by minimizing the sum of percentage errors. The quality of the E-NTU model is apparent from the fact that $Ж_1$ was found to be 1.0 for concurrent and 0.96 for countercurrent flow. Once $Ж_1$ was computed, $Ж_2$ is obtained by minimizing the maximum percentage error observed in all the cases. The equations obtained were:

$$\xi_{cocurrent} = 1.0\left(\frac{h_f}{h_p}\right)^{0.125} \qquad \text{Eq. 4-33}$$

$$\xi_{countercurrent} = 0.96\left(\frac{h_f}{h_p}\right)^{0.111} \qquad \text{Eq. 4-34}$$

For DCMD systems operating in a similar temperature range, this error function is generically applicable when the heat transfer coefficients of the streams can be estimated accurately, especially when the flows in the channels are uniform.

4.4.5. Model validation – with correction

The result obtained with the incorporation of the correction factor is shown in Figure 4.14 - Figure 4.21. It is evidenced that a slight overcorrection is observed in cases when the ratio of h_f to h_p is close to 1. However in cases when the ratio is not close to 1, a clear improvement can be seen. An overall evaluation of the modified E-NTU method for countercurrent flow is shown in Figure 4.22. The maximum error percentage has dropped from approximately 13% to 5.5%, with most of the data having a percentage error of less than 4%.

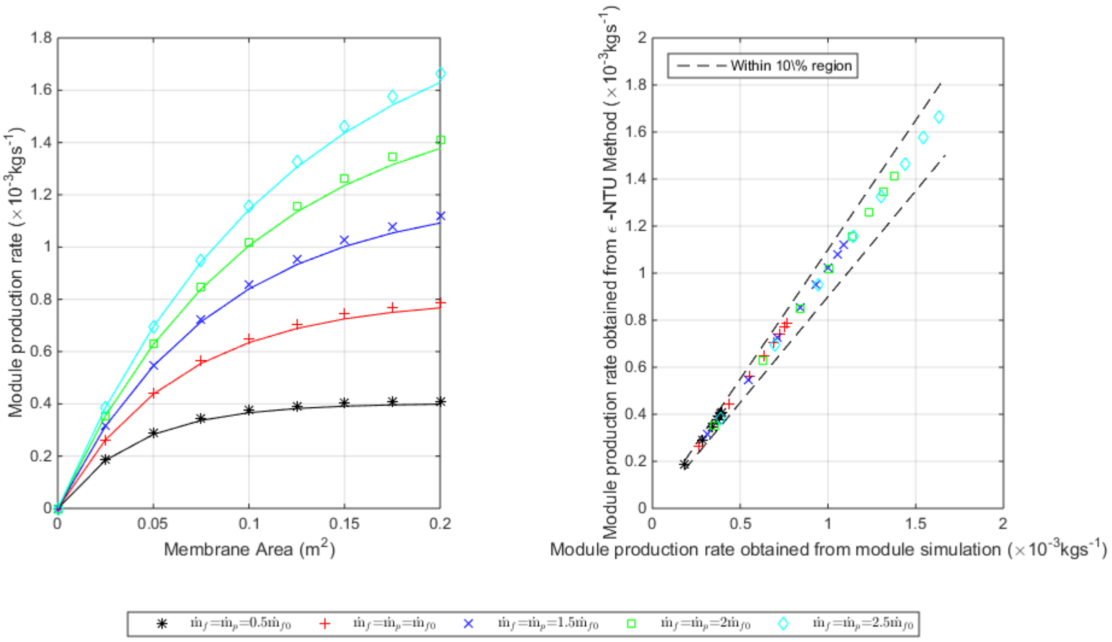

Figure 4.14 (A-left) and (B-right) Evaluation of E-NTU method for co-current flow: variation of module production rate with membrane area for various mass flowrates. Solid lines are simulated result obtained from MATLAB discretised DCMD module.

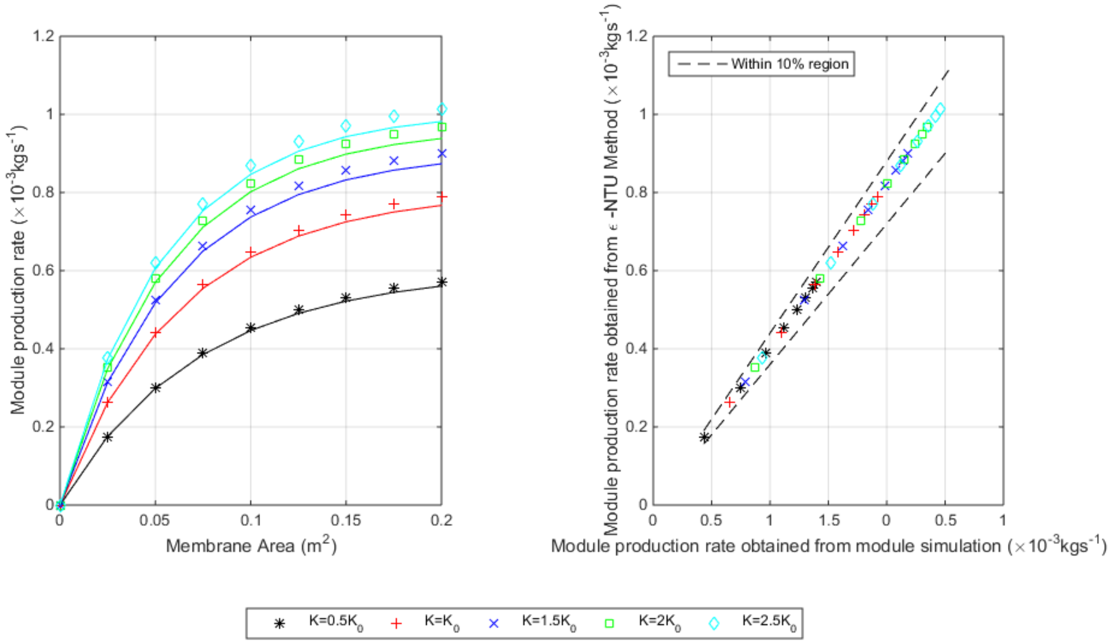

Figure 4.15 (A-left) and (B-right) Evaluation of E-NTU method for co-current flow: variation of module production rate with membrane area with changing membrane permeability. Solid lines are simulated result obtained from MATLAB discretised DCMD module.

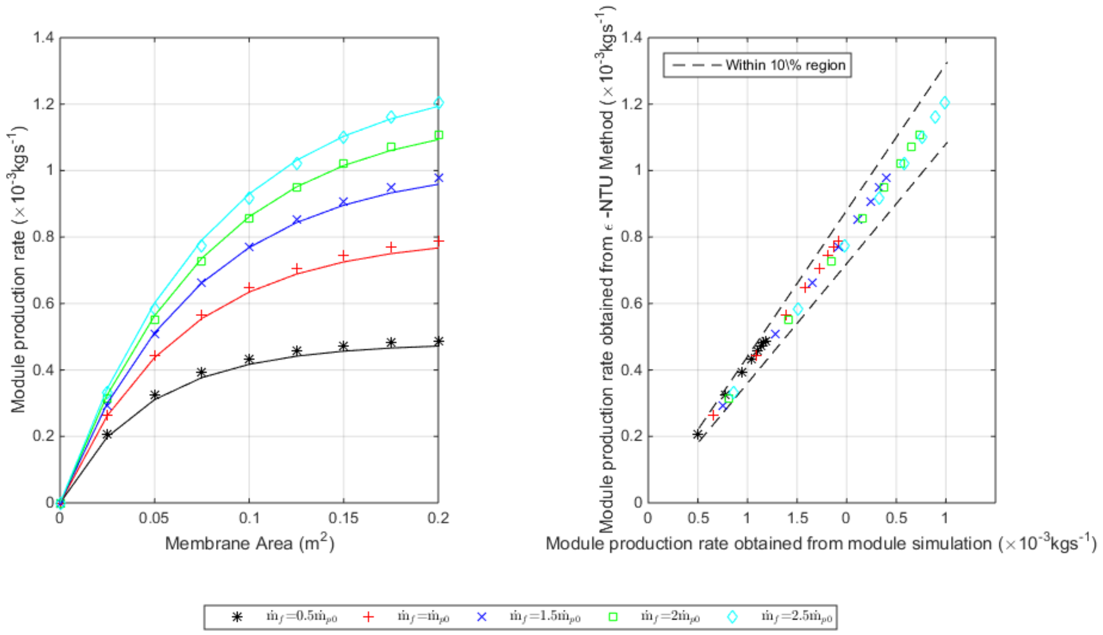

Figure 4.16 (A-left) and (B-right) Evaluation of E-NTU method for co-current flow: variation of module production rate with membrane area with changing feed to permeate ratio. Solid lines are simulated result obtained from MATLAB discretised DCMD module.

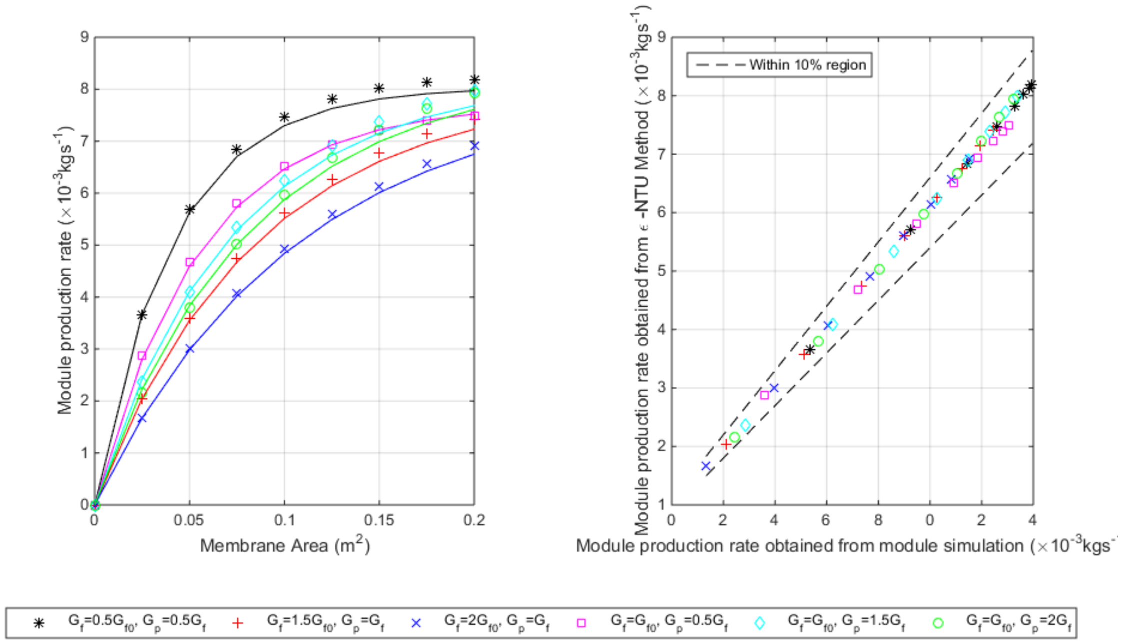

Figure 4.17 (A-left) and (B-right) Evaluation of E-NTU method for co-current flow: variation of module production rate with membrane area with changing channel dimensions. Solid lines are simulated result obtained from MATLAB discretised DCMD module.

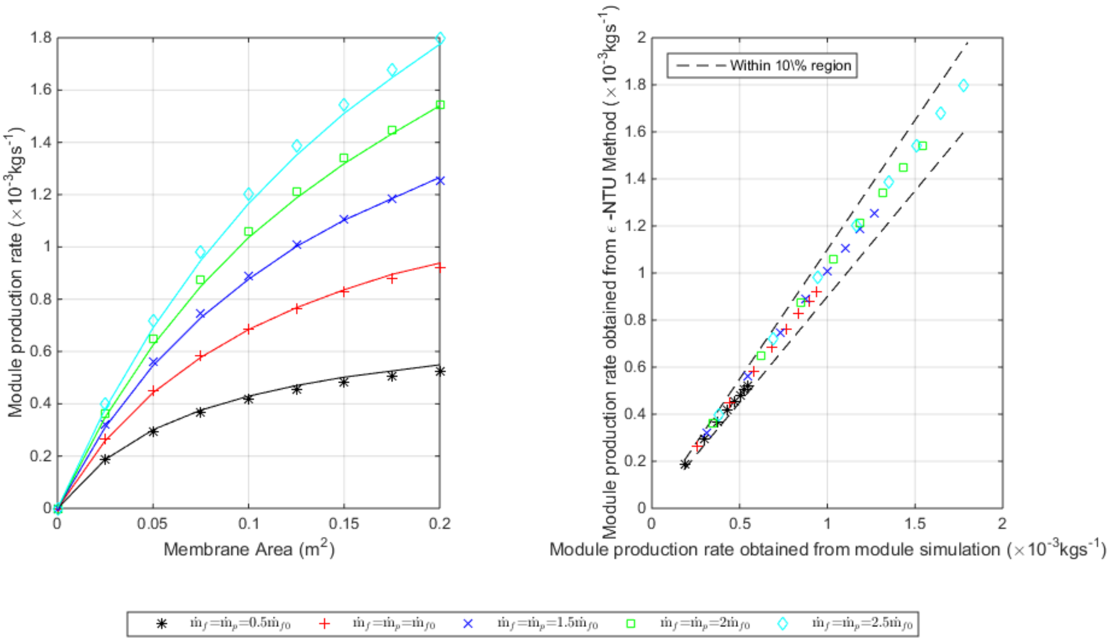

Figure 4.18 (A-left) and (B-right) Evaluation of E-NTU method for countercurrent flow: variation of module production rate with membrane area for various mass flowrates. Solid lines are simulated result obtained from MATLAB discretised DCMD module.

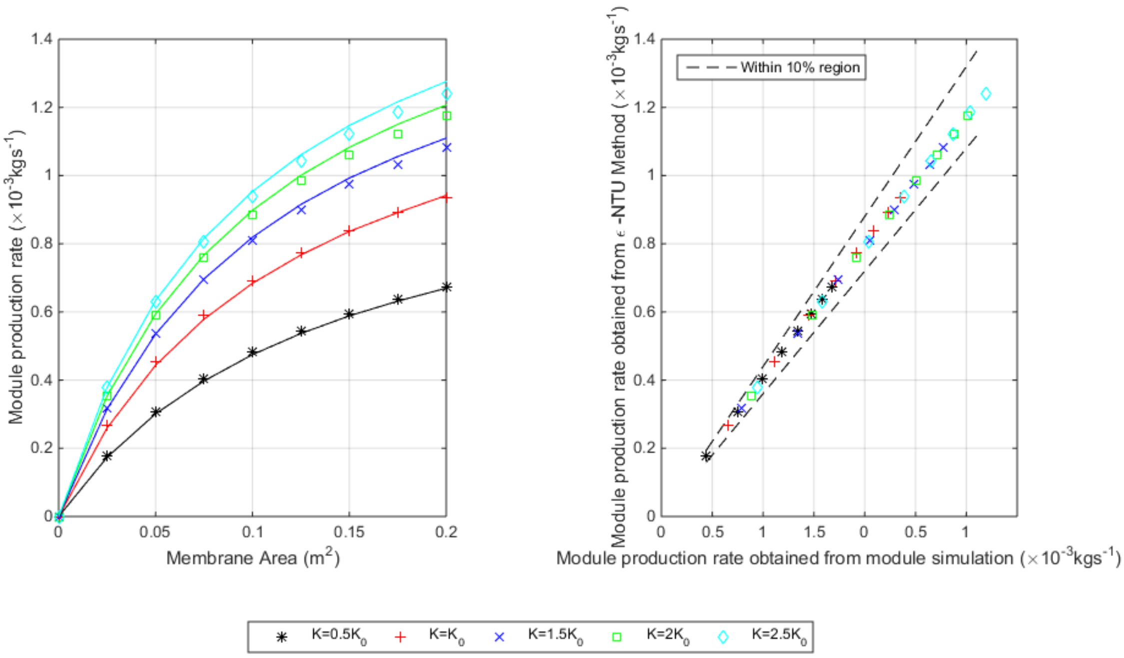

Figure 4.19 (A-left) and (B-right) Evaluation of E-NTU method for countercurrent flow: variation of module production rate with membrane area with changing membrane permeability. Solid lines are simulated result obtained from MATLAB discretised DCMD module.

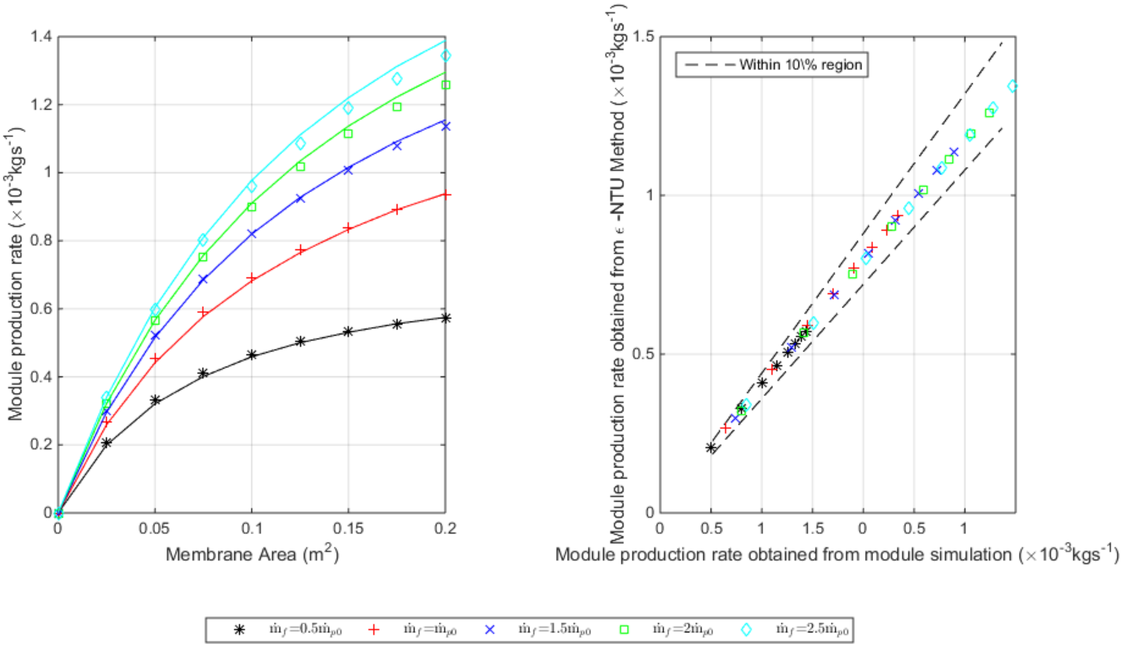

Figure 4.20 (A-left) and (B-right) Evaluation of E-NTU method for countercurrent flow: variation of module production rate with membrane area with changing feed to permeate ratio. Solid lines are simulated result obtained from MATLAB discretised DCMD module.

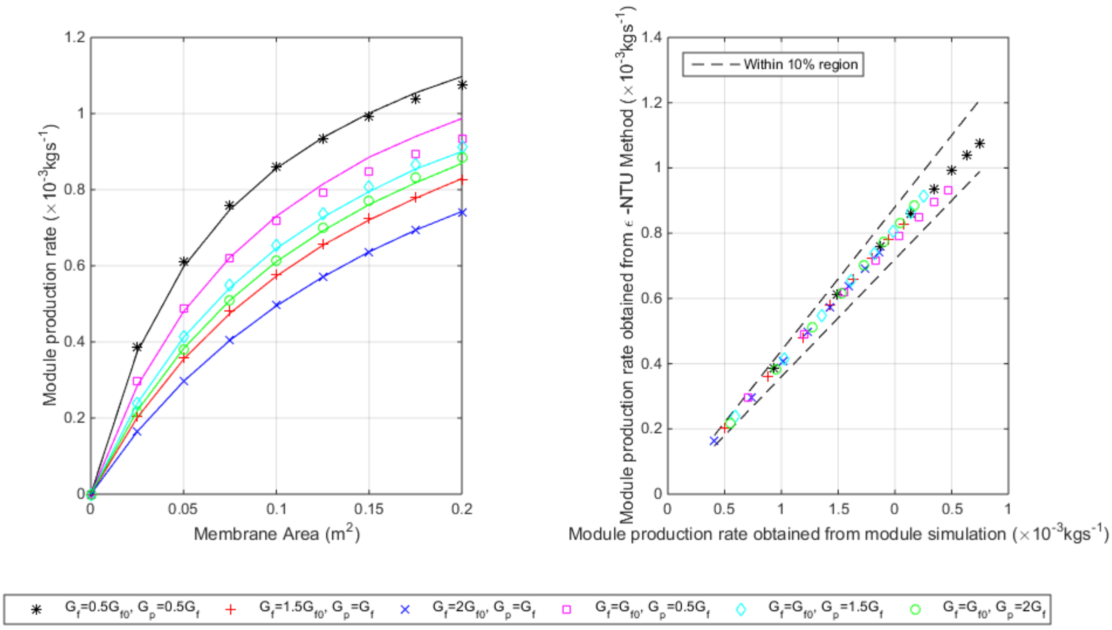

Figure 4.21 (A-left) and (B-right) Evaluation of E-NTU method for countercurrent flow: variation of module production rate with membrane area with changing channel dimensions. Solid lines are simulated result obtained from MATLAB discretised DCMD module.

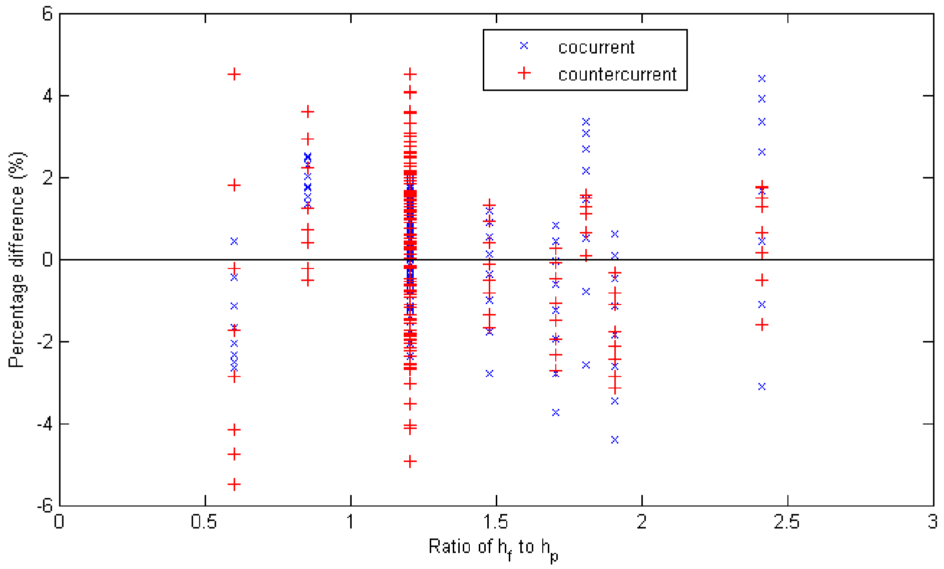

Figure 4.22 Percentage difference between discretization model and the E-NTU model with varying ratio of the heat transfer coefficients, after applying the error function.

4.5. Practical use of the E-NTU method

This E-NTU model for DCMD can be applied in a similar fashion as the conventional E-NTU for heat exchanger design and networking. Compared to other design tools or discretized or discretization model, this method combines rigorousness and versatility. It is suitable for any preliminary calculations, allowing one to 'have a feel' regarding sizing or throughput requirements and output estimations, prior to action. Action could range from design of experiments to constructing a more detailed model or to designing or scaling up a full-scale DCMD system or network. Moreover, any changes in operating conditions or the use of a membrane with a different permeability can be assessed very readily and easily using this set of E-NTU expressions. It is straight forward to explore the effect upon performance of changing T_f.

Moreover this model allows the use of any readily built heat exchanger models or systems for DCMD performance evaluation. This would save a lot of computation cost and time for constructing an equivalent DCMD models.

4.6. Chapter summary

Driven by scientific interest, a revisit to the use of the DGM for DCMD has identified some double counting of resistance. Thus a refined expression was introduced (Eq. 4-8) for estimating transmembrane flux using the DGM.

Considering the design and the practical application of DCMD, an equivalent E-NTU approach was introduced. The set of equations were derived in the same manner as those derived for the use of heat exchanger systems. The input into the E-NTU method is a, for a given module design and set of operating conditions. Then using the set of equations given in either Table 4-2 or Table 4-3 depending on module configurations, together with the algorithms provided in Figure 4.2 or 4.3 would enable a good performance or sizing estimations to be obtained for a concurrent and countercurrent DCMD. With the introduction of a correction function that accounts for the unequal contribution to performance by the two heat transfer coefficients, the error percentage was reduced to below 6%.

5. Influence of design on performance of countercurrent hollow fibre DCMD modules

5.1. Introduction

This chapter presents a parametric study on the sizing for a simple DCMD hollow fibre module (HFM) where no spacers of baffles are incorporated. A validated MATLAB DCMD-HFM model has been developed where the effects of flow configuration, length, fibre size and the number of fibres in the module on module performance were investigated.

5.2. Methodology

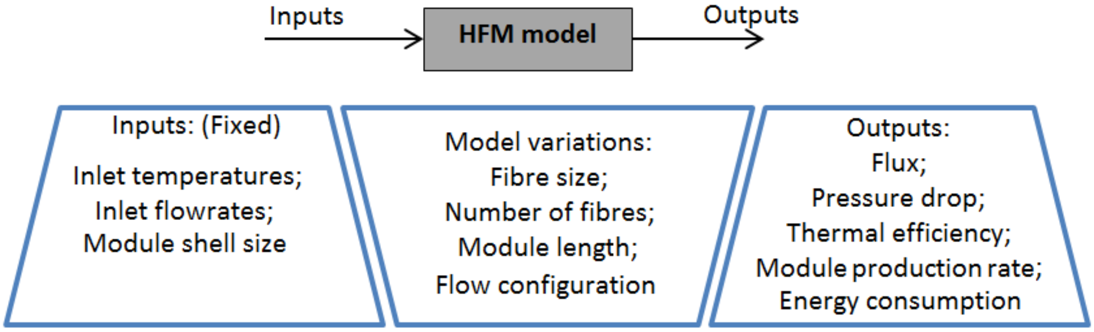

Figure 5-1 Scheme for problem resolution

Figure 5-1 shows the list of design parameters investigated in the parametric study. For a given module shell size, the fibre size, number of fibres, module length. Two flow configurations were tested at a fixed set of inlet flow conditions. The packing density, defined as the fraction of space occupied by the fibres within the HFM, is determined by the number of fibres and fibre size and is kept within the typical packing density range, between 0.25-0.7 (Pearce, 2012). The range of module length tested is

0.2-2m which is also the typical length of HFMs. Different flow configurations were also assessed, with feed either flow in the shell side, which is labelled hot-out-cold-in (HOCI), or feed flow inside the lumen of the fibres, which is labelled hot-in-cold-out (HICO). Transmembrane flux, module productivity and energy (thermal and overall) efficiencies are obtained for module evaluations.

5.2.1. Modelling of DCMD HFM

A simple HFM model, assuming cylindrical shell with cylindrical fibres, is simulated within the MATLAB environment. The same modelling approach as described in Chapter 3, section 3.2.4, for the flat sheet module is adopted in the current HFM configuration. Regarding mass transfer across the membrane, similar governing equations to those given previously in Section 2.1 are still applicable. The main difference is the heat transfer coefficient correlations for the membrane surface. However, due to the thickness and curvature of tubular membrane, the elemental area of the tubular membrane is given by:

$$\mathrm{A_{ele}} = \pi \mathrm{L_{ele}} \mathrm{d_{fi,lm}} \qquad \text{Eq. 5-1}$$

where L_{ele} denotes element length and $d_{fi,lm}$, denotes the logarithmic mean value of fibre diameter.

Since the main objective of this work is to observe the changes imposed by changing module arrangement and design, uniform membrane properties have been assumed in our model. Table 5-1 lists the key design features and assumptions used to model the HFM.

Table 5-1 Features and characteristic of the HFM model

Key features of the HFM model
(1) Random packing of fibres within the module
(2) No polydispersity of fibre **inner diameter**
(3) No polydispersity of fibre outer diameter

5.2.1.1. Flow in the fibre

The assumption of no polydispersity of fibre inner diameter allows uniform flow to be assumed within the lumen side of the fibre. The heat transfer coefficient inside the fibre is given by (Howatson, et al., 1973):

$$h = 1.615k\,(\mathrm{Re}\,\mathrm{Pr}\,d_{fi})^{\frac{1}{3}}\ L^{\frac{2}{3}} \qquad \text{Eq. 5-2}$$

and the pressure drop within a fibre is estimated using Darcy-Weisbach equation (Howatson, et al., 1973):

$$\Delta p_{fi} = f\frac{4L}{d_{fi}}\frac{\rho u^{2}}{2} \qquad \text{Eq. 5-3}$$

where f is the Darcy friction factor, which for laminar flow, can be expressed as:

$$f = \frac{16}{\mathrm{Re}} \qquad \text{Eq. 5-4}$$

5.2.1.2. Flow in shell side

The assumption of no polydispersity of fibre outer diameter suggests that the shell side flow distribution is only determined by the fibre arrangement in the module. Often the literature has assumed regular packing when modelling HFM (Ki , et al., 2015; Kim, 2014; Kim, et al., 2013), however it was found that the flow maldistribution caused by the random fibre arrangement has a huge impact on DCMD performance (Ding, et al., 2003). In this work, Voronoi tessellation method, which was introduced by Chen et al. in 1994 (Chen & Hlavacek, 1994), is used to model the random packing. This method has been adopted by other researchers to model randomly packed HFM (Cheng, et al., 2008; Wang, et al., 2003; Ding, et al., 2003; Ding, et al., 2006; Wu & Chen, 2000; Al-Obaidani, et al., 2008). Using this method, the module's cross-section is subdivided into polygonal cells, each associated with a single fibre each (depicted in Figure 5-2).

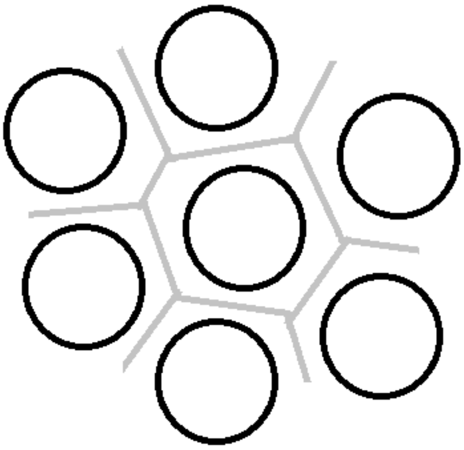

Figure 5-2 Illustration of Voronoi tessellation: A polygonal cell with a single fibre and its neighbouring fibres

The packing faction of the i th polygonal cell can be expressed as:

$$\phi_i = \frac{\mathrm{a_f}}{\mathrm{a}_i} \qquad \text{Eq. 5-5}$$

where $\mathrm{a_f}$ is the fibre area, and a is the polygonal cell area.

The probability, Џ, that a polygonal cell has a packing fraction between ϕ_1 and ϕ_2 is:

$$\text{Џ} = \int_{\text{ӄ}_1}^{\text{ӄ}_2} s^s \frac{\text{ӄ}^s}{(s-1)!} e^{-s\text{ӄ}}\, d\text{ӄ} \qquad \text{Eq. 5-6}$$

where $$\text{ҁ}_i = \frac{(1-\phi_{\mathrm{i}})\phi}{(1-\phi\,)\phi_{\mathrm{i}}}, i = 1{,}2 \qquad \text{Eq. 5-7}$$

where s is the number of nearest neighbouring fibres and is assumed to be 6 in our model (Wu & Chen, 2000; Chen & Hlavacek, 1994). The fractional flow in the shell side for the i th polygonal cell categories can be expressed as (Ding, et al., 2003):

$$\mathrm{W}_i = \text{Ɥ}_i \left[\frac{(\mathrm{f\,Re})_{\mathrm{e}}}{(\mathrm{f\,Re})_{\mathrm{i}}}\right]\left[\frac{(1-\phi_{\mathrm{i}})\phi}{(1-\phi\,)\phi_{\mathrm{i}}}\right]^3 \qquad \text{Eq. 5-8}$$

where (f Re) is the product of the friction factor and Reynolds number. Its effective values, $(\mathrm{f\,Re})_{\mathrm{e}}$, for the hollow fibre bundle can be obtained using:

$$\frac{1}{(\mathrm{f\,Re})_{\mathrm{e}}} = \sum_{i=1}^{m} \text{Ɥ}_i \left[\frac{1}{(\mathrm{f\,Re})_{\mathrm{i}}}\right]\left[\frac{(1-\phi_{\mathrm{i}})\phi}{(1-\phi\,)\phi_{\mathrm{i}}}\right]^3 \qquad \text{Eq. 5-9}$$

where $(\mathrm{fRe})_{\mathrm{i}}$ was obtained using Figure 5-3, extrapolating and interpolating the data, assuming a triangular array.

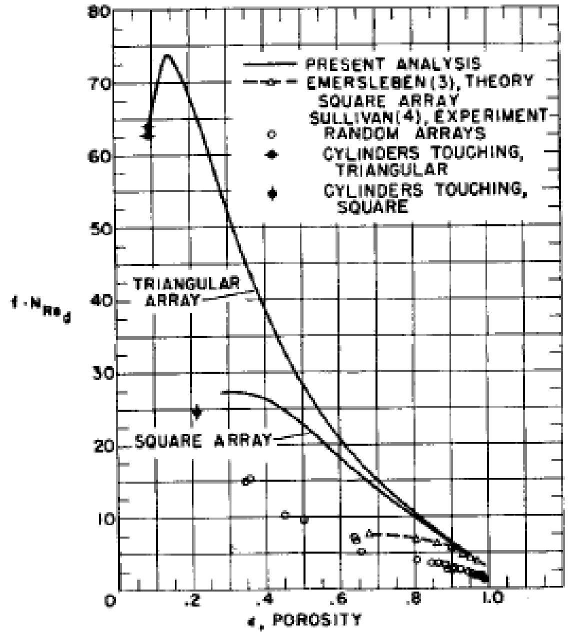

Figure 5-3 Friction factor – Reynolds number as a function of porosity (Fig. 7 in (Sparrow & Loeffler JR., 1959))

Ignoring the entrance and exit losses, and assuming laminar flow throughout the fibre bundle (Chen & Hlavacek, 1994), the pressure drop in the shell side can be calculated using:

$$\Delta \mathrm{p}_{\mathrm{shell}} = \left(\frac{2\mu \mathrm{L}}{\rho}\right)\left(\frac{(\mathrm{f\,Re})_{\mathrm{e}}}{A_c \mathrm{d}_{\mathrm{h}}^2}\right)\dot{m} \qquad \text{Eq. 5-10}$$

where the characteristic dimension of heat transfer on the shell side, $\mathrm{d_h}$, is given by (Cheng, et al., 2008; Kim, et al., 2013):

$$\mathrm{d_h} = \left(\frac{(1-\phi)}{\phi}\right)\mathrm{d_o} \qquad \text{Eq. 5-11}$$

The local velocity of the shell side fluid is given by dividing the fractional flow in the shell side (obtained using Eq. 5-8) by the corresponding area in the module (obtained by solving Eq. 5-6 and substituting into Eq. 5-5). Finally, the local heat transfer coefficient in each flow area can be estimated from the following relationship. When the flow is in laminar region, Lévêque's equation is used, which for a single tube or channel (Wu & Chen, 2000; Lévêque, 1928) is:

$$\mathrm{Nu_i} = 1.615\left(\frac{\mathrm{Re_i Pr\, d_{hi}}}{\mathrm{L}}\right)^{1/3} = \frac{\mathrm{h_i d_{hi}}}{\mathrm{k}} \qquad \text{Eq. 5-12}$$

5.2.2. Module performance indicators

The transmembrane flux and module production rate were computed directly as model outputs. Thermal efficiency, η_{th}, is defined by assessing the fraction of energy that has been used to evaporate the water permeating through the membrane.

$$\eta_{th} = \frac{E^{T}_{vap.}}{E^{T}_{th}} \qquad \text{Eq. 5-13}$$

where $E^{T}_{vap.}$ is total heat used for vaporization, and is given by the expression:

$$E^{T}_{vap.} = \sum_{1}^{n_{ele}} A_{ele} N_{ele}\, \lambda \qquad \text{Eq. 5-14}$$

where n_{ele} denotes the number of elements (or strips in the model), axially, in the module simulation, A_{ele} is the elemental area, whilst N_{ele} and λ are respectively the transmembrane flux and heat of vapourization at the membrane temperature at the element. E^{T}_{th} is thermal energy required by the system, which is given by:

$$E^{T}_{th} = c_f \dot{m}_f (T_{f,in} - T_{f,out}) \qquad \text{Eq. 5-15}$$

For the overall energy efficiency, η_e, the electrical energy, E^{T}_{e}, required for pumping is included, where E_e is obtained using:

$$E^{T}_{e} = \sum_{k} \dot{m}_k \ (1 + 0.15).\Delta p_k; \quad k = \text{feed, permeate} \qquad \text{Eq. 5-16}$$

assuming that the pressure lost due to the piping could reach around 15% of the pressure drop through the membrane Δp_k (Bui, et al., 2010).

Then η_e is calculated by:

$$\eta_e = \frac{E^{T}_{vap.}}{E^{T}_{th} + E^{T}_{e}} \qquad \text{Eq. 5-17}$$

In this work, a simple linear addition of thermal and electrical energy is used to obtain the total energy spent in the system (denominator in Eq. 5-17) and the subsequently energy efficiency calculation. However it is important to highlight that the two forms of energy (heat and electrical work) are fundamentally different. Thus the simple linear addition should be modified correspondingly to the cost and availability of the energy sources if data is available.

5.3. Model validation

To verify the model's validity, its simulation result were compared to the experimental data collected from two independent experimental studies studies (Al-Obaidani, et al., 2008; Pantoja, et al., 2015). Both set of experiment were conducted with a commercial hollow fibre module, Microdyn Nadir MD020CP2N, with heated saline solution fed to the tube side and cold water fed to the shell side in countercurrent mode. The properties of the module, MD020CP2N, are listed in Table 5-2.

Table 5-2 Properties of membrane module, MD020CP2N

Manufacturer	Microdyn Nadir[2]
Number of fibres, NF	40
Length of fibres, (m)	0.47
Fibre inner diameter (mm)	1.8
Shell diameter, d_s (mm)	20
Pore diameter, d_p (μm)	0.2
Membrane thickness, δ (μm)	400[3]
Porosity, Ɛ (%)	70
Effective area (based on inner fibre diameter), (m^2)	0.1
Tortuosity, χ	1.42[4]
Membrane material	Polypropylene

---

[2] Key module characteristics are based on commercial module, MD020CP2N, produced by Microdyn Nadir (Anon., n.d.)

[3] As reported in (Lee & Kim, 2014).

[4] Taking tortuosity as the inverse of porosity, as in (Al-Obaidani, et al., 2008)

Adopting the design specifications of MD020CP2N (listed in Table 5-2) into our MATLAB model, the transmembrane flux of each discretised element is calculated using Eq. 4-8.

Table 5-3 Model results compared with experimental data reported in literature (Pantoja, et al., 2015)

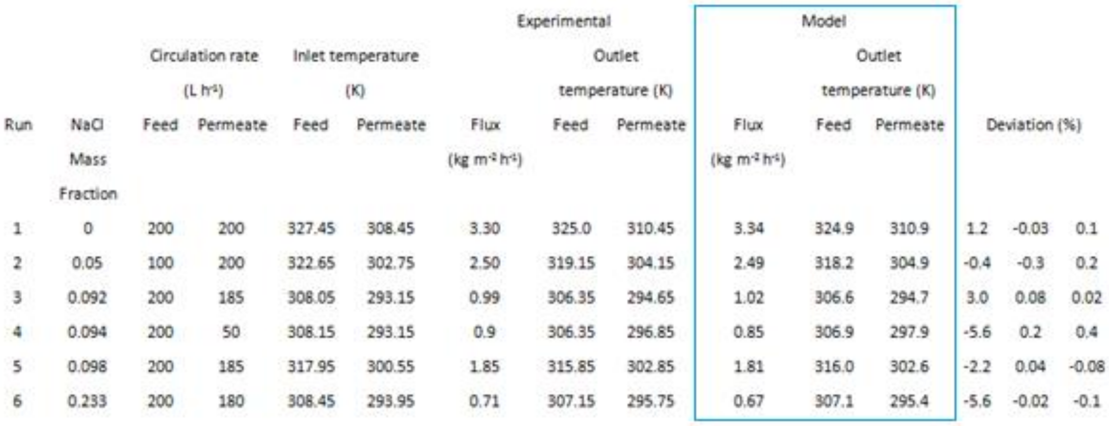

						Experimental			Model					
		Circulation rate $(L\ h^{-1})$		Inlet temperature (K)			Outlet temperature (K)			Outlet temperature (K)				
Run	NaCl Mass Fraction	Feed	Permeate	Feed	Permeate	Flux $(kg\ m^{-2}\ h^{-1})$	Feed	Permeate	Flux $(kg\ m^{-2}\ h^{-1})$	Feed	Permeate	Deviation (%)		
1	0	200	200	327.45	308.45	3.30	325.0	310.45	3.34	324.9	310.9	1.2	-0.03	0.1
2	0.05	100	200	322.65	302.75	2.50	319.15	304.15	2.49	318.2	304.9	-0.4	-0.3	0.2
3	0.092	200	185	308.05	293.15	0.99	306.35	294.65	1.02	306.6	294.7	3.0	0.08	0.02
4	0.094	200	50	308.15	293.15	0.9	306.35	296.85	0.85	306.9	297.9	-5.6	0.2	0.4
5	0.098	200	185	317.95	300.55	1.85	315.85	302.85	1.81	316.0	302.6	-2.2	0.04	-0.08
6	0.233	200	180	308.45	293.95	0.71	307.15	295.75	0.67	307.1	295.4	-5.6	-0.02	-0.1

With varying the feed and permeate's temperature, flowrates and salt concentration, Table 5-3 shows that the simulated result including transmembrane flux, feed and permeate outlet temperature, are in good agreement with experimental data, with the maximum derivation being 5.6%. It also shows that the current model provides reliable predictions as saline feed as concentrated as 23.3 (w/w %) was included for comparison. Figure 5-4 shows that as the feed side temperature was increased from 303K to 343K, the flux was increasing exponentially and good agreement was observed for transmembrane fluxes between the model predictions and the experimental data. While the accuracy of the model deviates slightly under different operation conditions, Figure 5-4 and Table 5-3 show that the model provides good prediction for the wide range of feed concentration and operating temperature typically used for DCMD desalination.

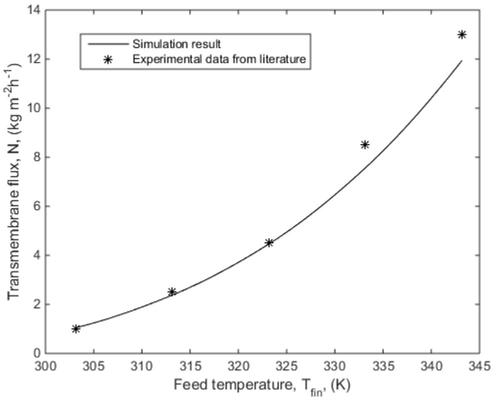

Figure 5-4 Comparison of current simulation results with experimental data reported in literature (Al-Obaidani, et al., 2008), showing the effects of feed temperature on DCMD, with feed concentration of 35g L^{-1}, $\dot{m}_f$ = 0.055 kg s^{-1}, $\dot{m}_p$= 0.027 kg s^{-1} and $T_{p,in}$=288.15K. Only feed temperature were adjustable for this simulation.

5.4. Result and discussions

Having validated the model it was used to explore the impact of individual design feature on DCMD-HFM performance. Starting with an investigation on the significance of flow configurations, in Section 5.4.1, results obtained with the two configurations, HICO and HOCI are presented and compared. Following this, the influence of packing density and fibre size are examined in Section 5.4.2. A discussion on module length and area on module performance is included in Section 5.4.3.

5.4.1. Examining the effect of flow configurations – HICO vs HOCI

Figure 5-5 - Figure 5-8 show the transmembrane flux and thermal efficiency achieved by simulations with the two different flow configurations. With different module designs specifications being tesed (which will be discussed further in a later section), our results show that HICO operation mode is superior in both performance in flux and thermal efficiency. The difference in thermal efficiency is most significant, HICO mode achieves an average of 0.54 while the HOCI mode obtains a thermal efficiency that is below 0.5. This contradicts Ki et al. (2015)'s recent publications which states in the theory and simulation that "We consider the hot-out/cold-in (HOCI) operation mode of HFDCMD, where the hot and cold streams flow in the shell and lumen regions, respectively. The opposite operational scheme is the hot-in/cold-out (HICO) mode. HOCI maximizes the flux with properly (sic) available heat sources, and HICO fully utilizes any available thermal energy in the feed stream."

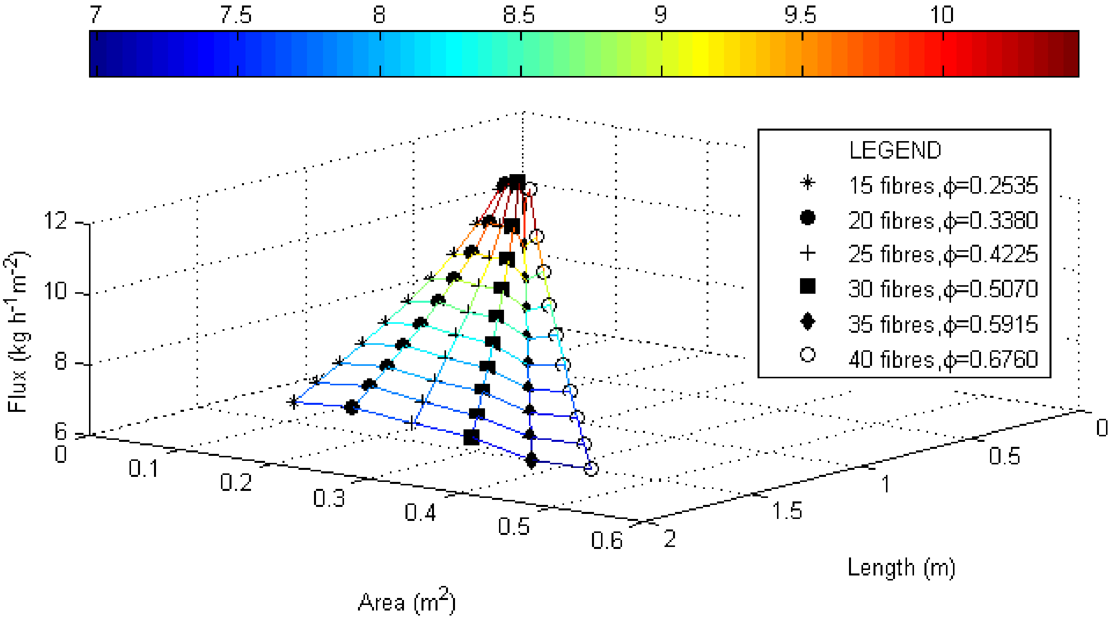

Figure 5-5 Influence of packing density (d_f=1.8mm) and module size on module transmembrane under HICO operating mode. ($\dot{m}_f = \dot{m}_p = 0.055\ kg\ s^{-1}$; $T_{f,in}$ = 343K and $T_{p,in}$=298K, NaCl concentration=2 w/w %)

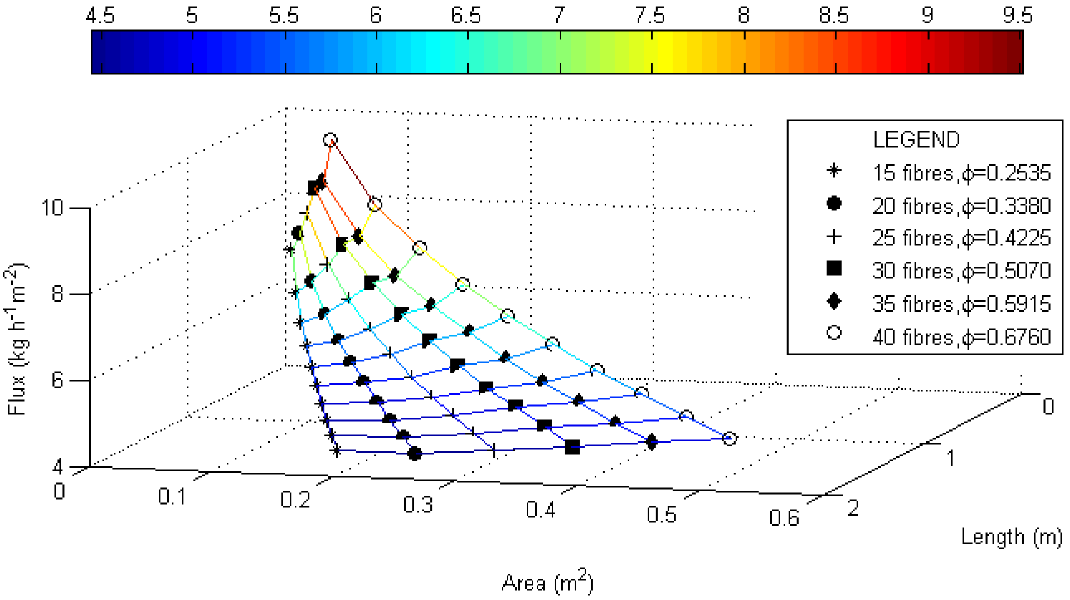

Figure 5-6 Influence of packing density (d_f=1.8mm) and module size on module transmembrane under HOCI operating mode. ($\dot{m}_f = \dot{m}_p = 0.055\ kg\ s^{-1}$; $T_{f,in}$ = 343K and $T_{p,in}$=298K, NaCl concentration=2 w/w %)

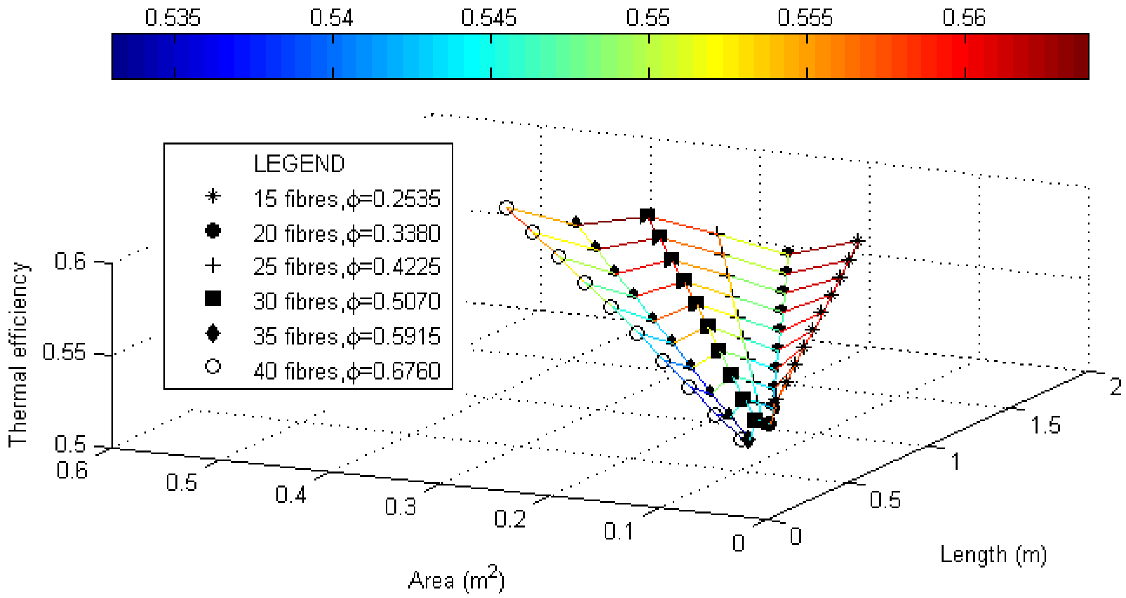

Figure 5-7 Influence of packing density (d_f=1.8mm) and module size on module transmembrane under HICO operating mode. ($\dot{m}_f = \dot{m}_p = 0.055\ kg\ s^{-1}$; $T_{f,in}$ = 343K and $T_{p,in}$=298K, NaCl concentration=2 w/w %)

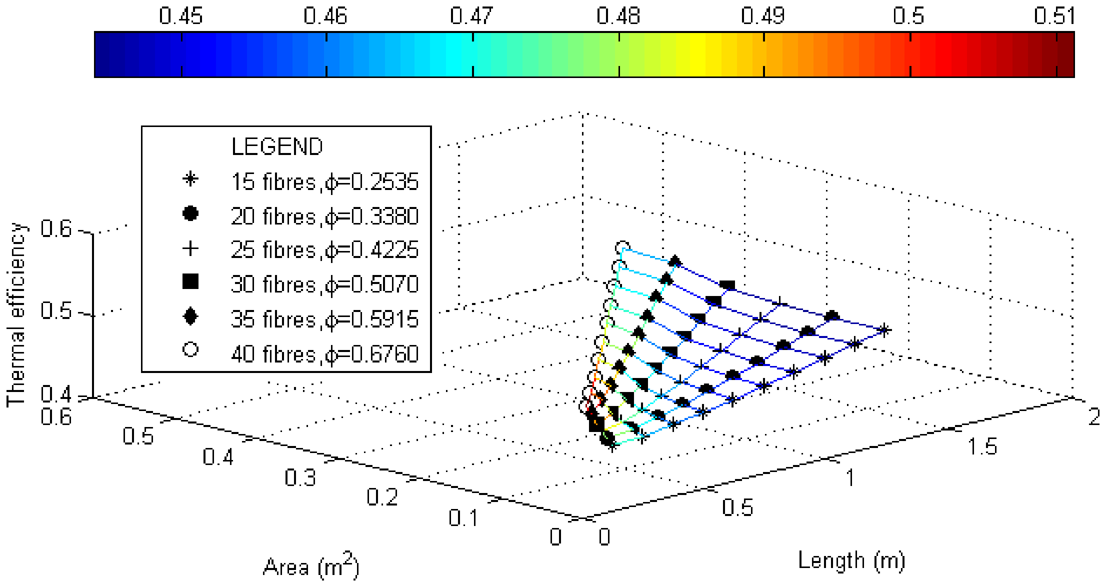

Figure 5-8 Influence of packing density (d_f=1.8mm) and module size on module transmembrane under HOCI operating mode. ($\dot{m}_f = \dot{m}_p = 0.055\ kg\ s^{-1}$; $T_{f,in}$ = 343K and $T_{p,in}$=298K, NaCl concentration=2 w/w %)

With the same one to one ratio of feed and permeate applied to both operation mode, HICO demonstrates better performance due to better heat transfer being established. As discussed in the previous chapter and reported in the literature survey, h_f

has a more dominant role in mass transfer in MD systems than h_p. As a result, having the hot saline feed inside the lumen of the fibre favours a higher h_f which enhances the module performance. Moreover, the resultant flow maldistribution caused by the random packing has undermined the mass transfer in the shell side. Thus having the hot saline flowing in the shell side would result in less effective heat and mass transfer.

Without the use of any turbulence enhancing devices, observations suggest that HICO deliver better performance, the following investigations focus on the HICO configuration. However it is important to highlight that improved shell-side mixing and enhanced flow distribution can be achieved by structured shell packing or winding, adding spacers or using bubbling. While the heat transfer coefficient of the flow within the lumen is primarily governed by the flowrate, when one of these approaches is adopted, HOCI becomes more attractive as the heat transfer of the fluid flowing through the shell is improved.

5.4.2. The influence of packing density and fibre size on DCMD-HFM performance

For a module with fixed outer module size, its packing density depends on the fibre size and the number of fibres within the module. From Figure 5-5, it is observed that in HICO mode, while higher fluxes are observed when the module size is shorter, packing density does not seem to play a significant role on transmembrane flux. To investigate this further, Figure 5-9 is presented. As our simulations generate data between module length 0.2-2m long (which is the typical range for HFM), each curve in Figure 5-9 ends with a different X-axis value. From Figure 5-9, it is observed that while there is a general trend which suggests the transmembrane flux monotonically increases with packing density up to 0.5 (light blue line). Above this there is a dip at a packing density of approximately 0.6 (green solid line). A dip has been mentioned because at a value of 0.67 the fluxes are greater than at 0.5. This dip is probably due to the combined (feed and permeate) hydrodynamic and/or thermodynamic conditions. For a typical HFM which only involves mass transfer, both experimentally and through their model, Wu and Chen (2000) showed that the mass transfer coefficient in the shell side is at its minimum when the packing is around 0.5, and Ding et al. (2003) has predicted similar behaviour.

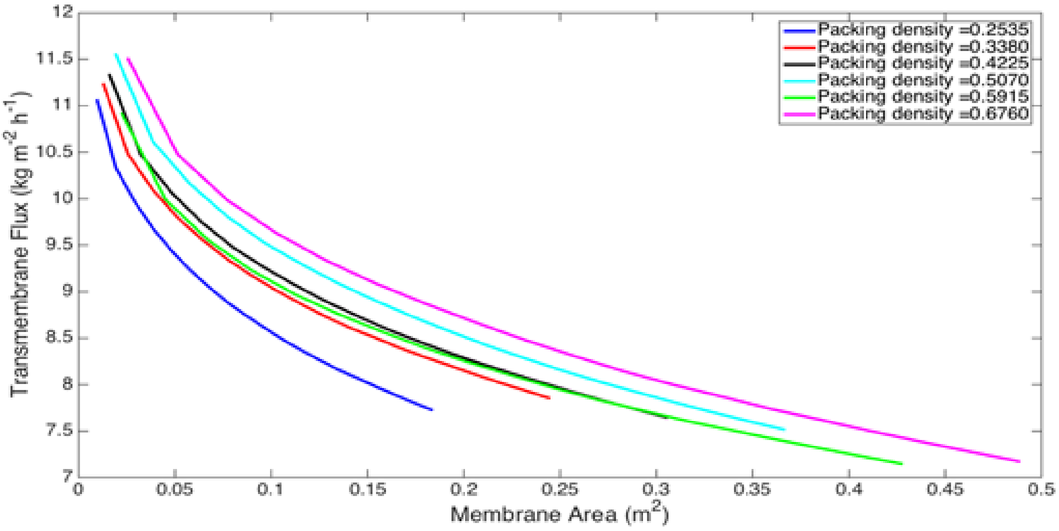

Figure 5-9 A 2-D plot showing the effect of packing density (d_f=1.8mm) and membrane area on module transmembrane for HICO mode ($\dot{m}_f = \dot{m}_p = 0.055\ kg\ s^{-1}$; $T_{f,in}$ = 343K and $T_{p,in}$=298K, NaCl concentration=2 w/w %)

While packing density does not seem to play a significant role in HICO configuration, it is interesting to point out that according to Figure 5-6, in HOCI operational mode, transmembrane flux is highly dependent on the packing density of the module. This could again be explained by the importance and impact of a higher h_f in MD systems.

Figure 5-8 shows that in HOCI operation mode, the thermal efficiency is also at its highest in the densest arrangement in HOCI operation mode. It is important to point out that the colour bar in each figure corresponds to a different scale, and for the figures showing thermal and energy efficiency, the value obtained for the same operation mode with different packing density is relatively small, typically within a range of 0.03. In contrast to HOCI mode, when one examines the thermal efficiency in HICO operation, there is not a clear trend from Figure 5-7.

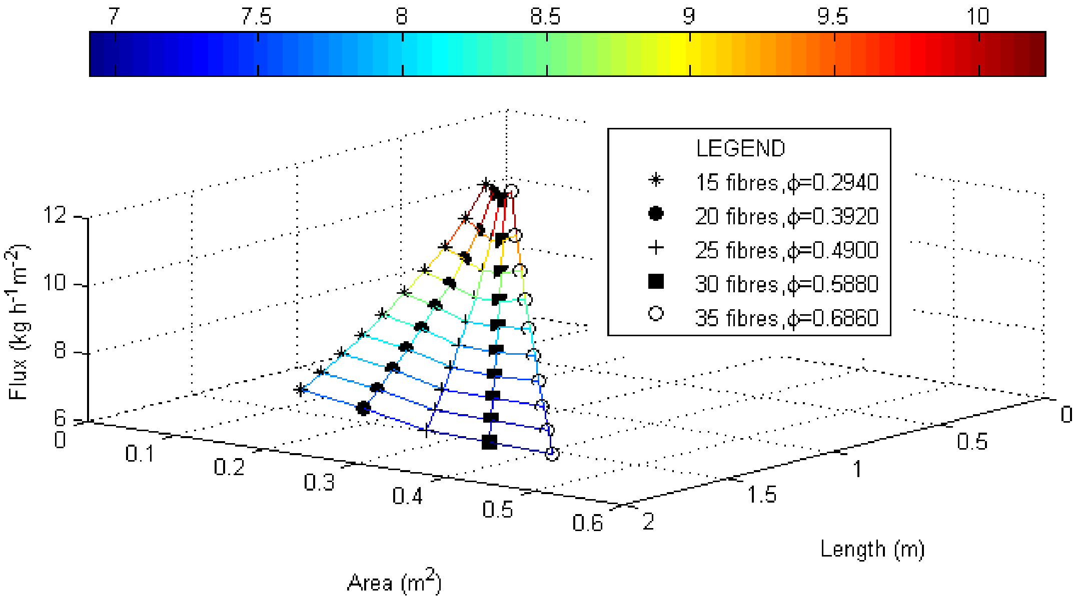

Figure 5-10 Influence of packing density (d_f=2mm) and module size on module transmembrane under HICO operating mode. ($\dot{m}_f = \dot{m}_p = 0.055\ kg\ s^{-1}$; $T_{f,in}$ = 343K and $T_{p,in}$=298K, NaCl concentration=2 w/w %)

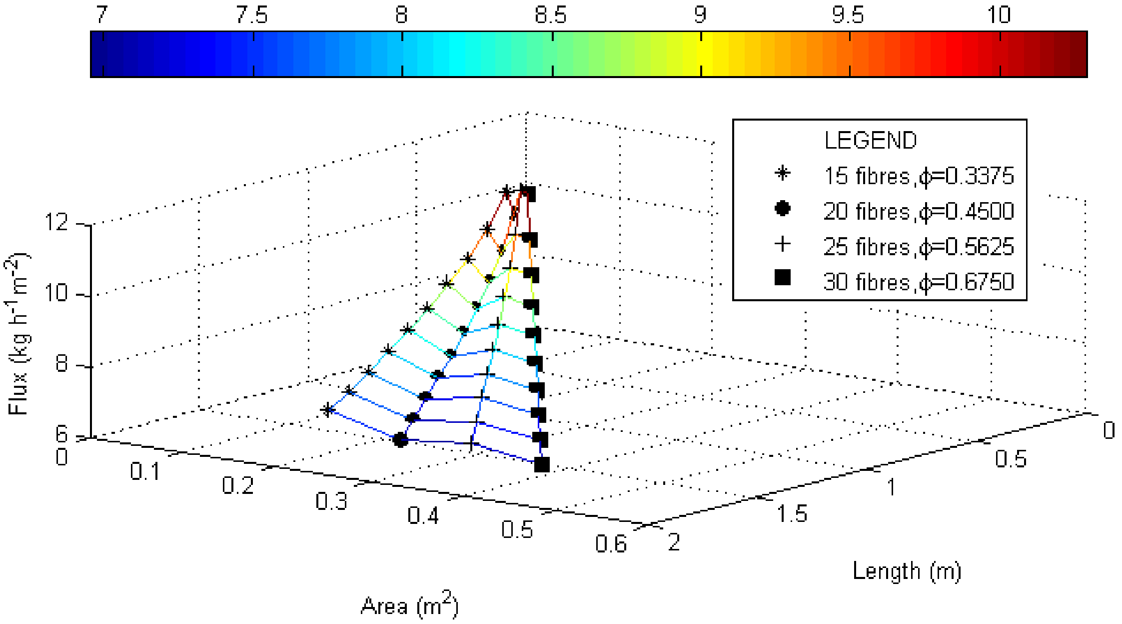

Figure 5-11 Influence of packing density (d_f=2.2 mm) and module size on module transmembrane under HICO operating mode. ($\dot{m}_f = \dot{m}_p = 0.055\ kg\ s^{-1}$; $T_{f,in}$ = 343K and $T_{p,in}$=298K, NaCl concentration=2 w/w %)

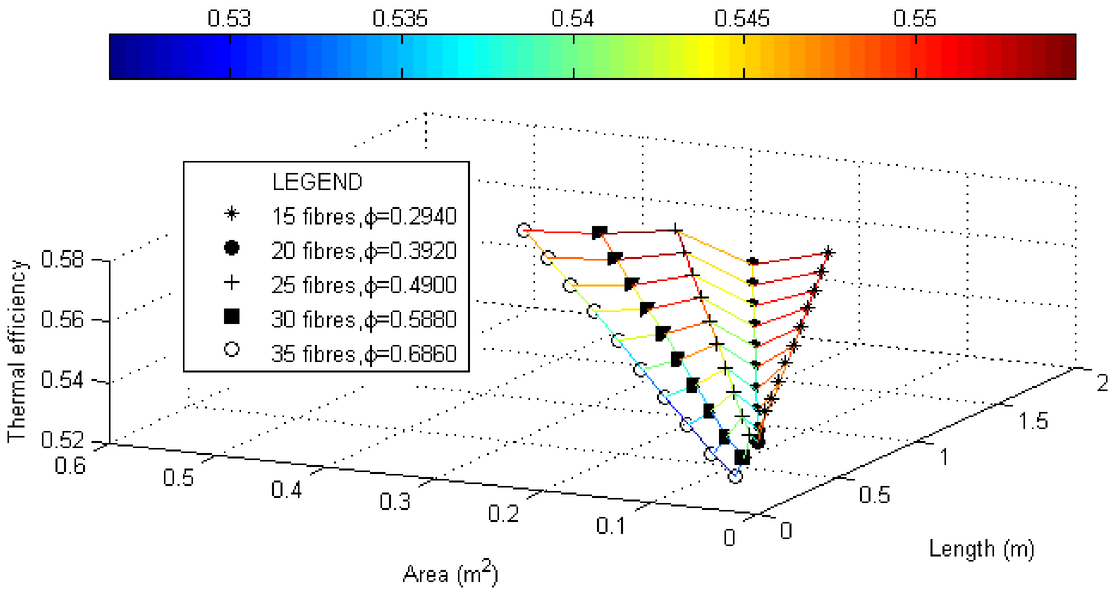

Figure 5-12 Influence of packing density (d_f=2mm) and module size on module transmembrane under HICO operating mode. ($\dot{m}_f = \dot{m}_p = 0.055\ kg\ s^{-1}$; $T_{f,in}$ = 343K and $T_{p,in}$=298K, NaCl concentration=2 w/w %)

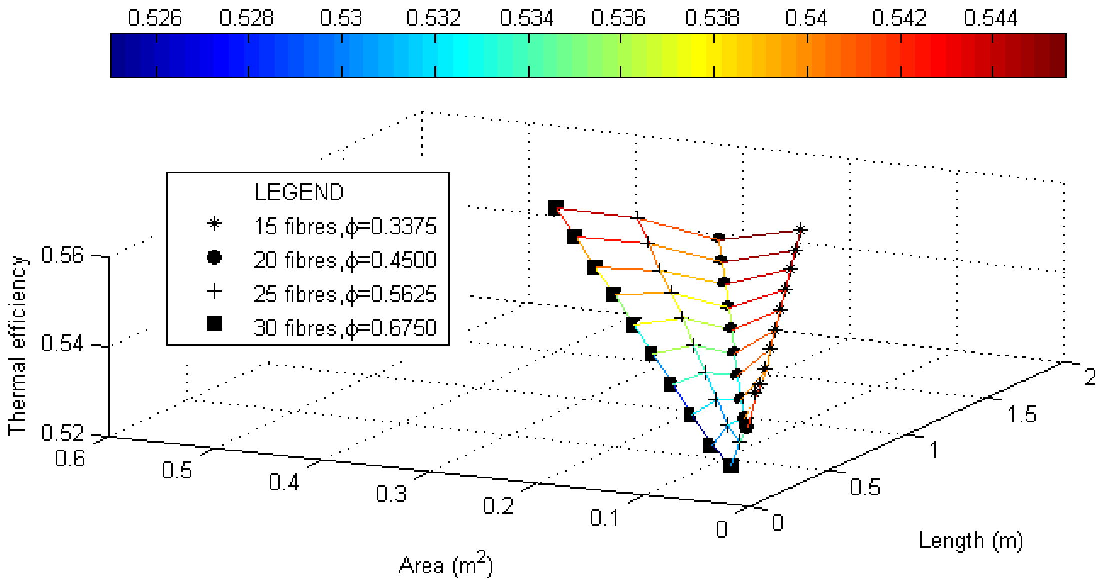

Figure 5-13 Influence of packing density (d_f=2.2 mm) and module size on module transmembrane under HICO operating mode. ($\dot{m}_f = \dot{m}_p = 0.055\ kg\ s^{-1}$; $T_{f,in}$ = 343K and $T_{p,in}$=298K, NaCl concentration=2 w/w %)

Figure 5-10 -Figure 5-13 display the results obtained when different fibre sizes were used, and the packing density was kept between 0.25-0.7. According to these figures, the module with different fibre size behave in a similar manner as the one with the smallest fibre size (d_f=1.8mm). From the inspection of Figure 5-7, Figure 5-12 and Figure 5-13, the simulation results suggest that there is only a slight improvement of thermal efficiency with smaller fibres.

One of the key considerations for designing and sizing a DCMD-HFM is the pressure drop along across the module. Figure 5-14 shows the change in pressure drop due to changes in packing density. Both Figure 5-14A and B suggest that with the same packing density, the smaller fibres result in higher pressure not only along the fibres but also axially in the shell side. Considering Eq. 5-3, with the same packing density the flow velocity within the fibre should be the same, yet due to the smaller hydraulic diameter, a higher pressure drop is to be expected; for laminar flow $\Delta p \propto u_p/d^2$.

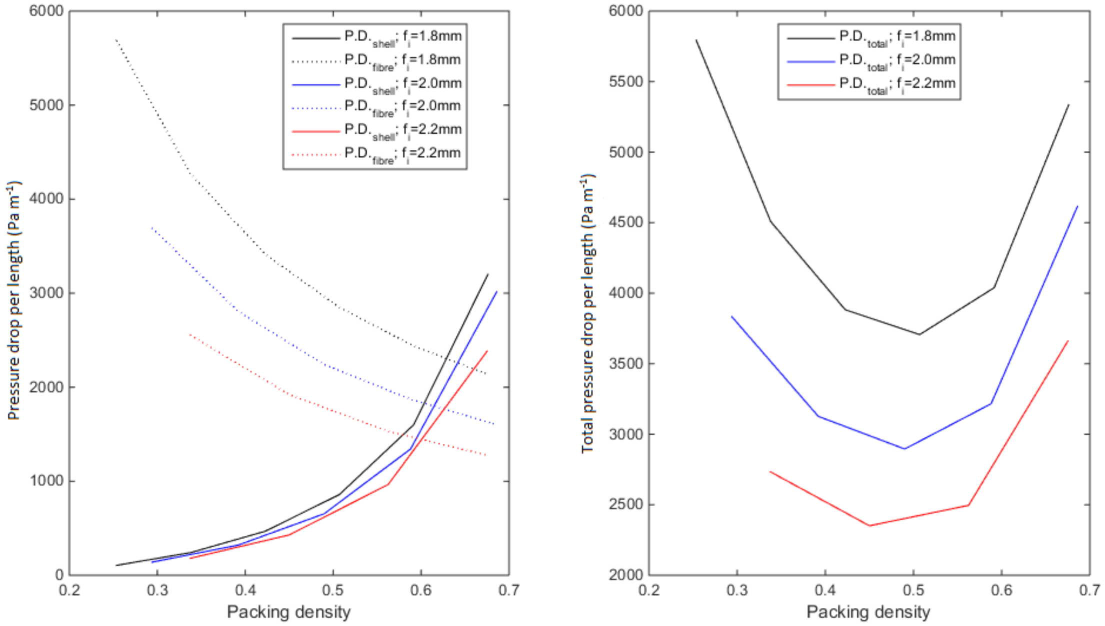

Figure 5-14 Pressure drop inside the module shell and the fibres; (B-right) Total pressure drop in module per meter length with respect to packing density and fibre size. ($\dot{m}_f = \dot{m}_p = 0.055$ kg s^{-1}; $T_{f,in}$ = 343K and $T_{p,in}$=298K)

It is evidenced from Figure 5-14 that as packing density increases (the number of fibre increases), the pressure drop in the shell side increases significantly. On the other hand due to lower flowrate per fibre, the pressure drop in the fibres decreases. When considering the total pressure drop of the module (there will typically be equal flows on each side). Figure 5-14B suggests that a minimum value is found when the packing density is about 0.5. As larger membrane area is packed in denser module with small fibres, Figure 5-15 is plotted for a more representative comparison. It shows that with respect to packing area within the range of 0.45-0.65, the difference in pressure drop per unit area is relatively insignificant. Moreover, the difference in pressure drop corresponding to different fibre sizes is within 10000Pa, which is a relatively small value.

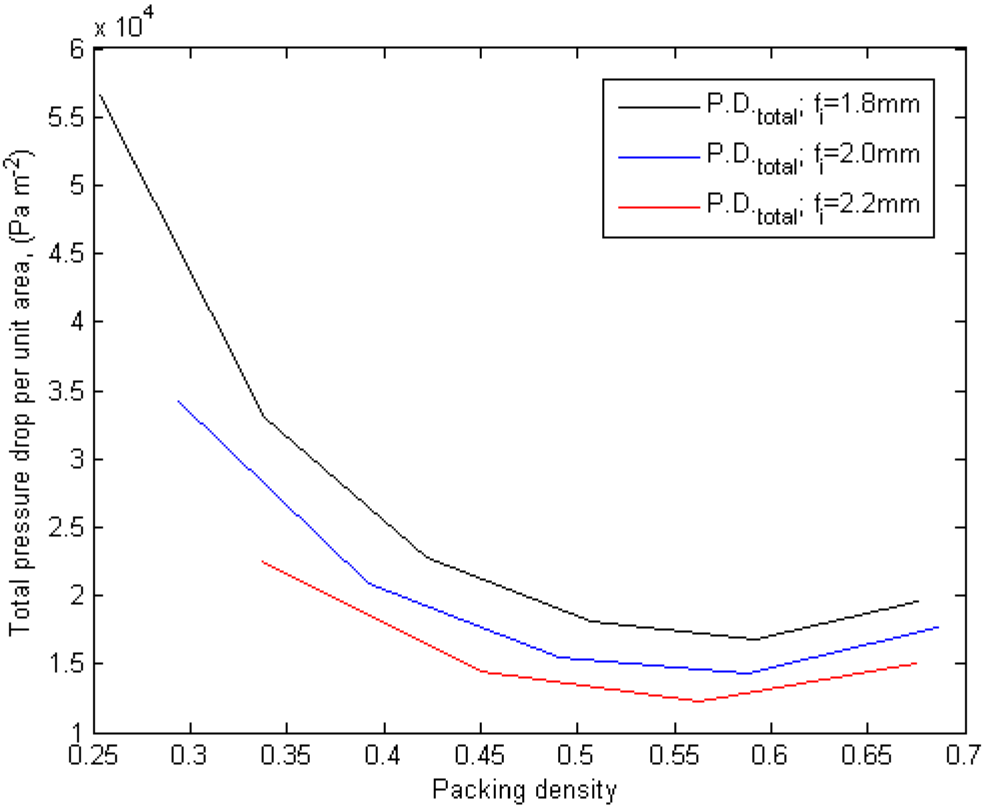

Figure 5-15 Total pressure drop in module per unit area with respect to packing density and fibre size. ($\dot{m}_f = \dot{m}_p = 0.055$ kg s^{-1}; $T_{f,in}$ = 343K and $T_{p,in}$=298K)

Accounting for the heat loss via conduction and the energy required for pumping, using Eq. 5-17 the energy efficiency of the modules is given in Figure 5-16.

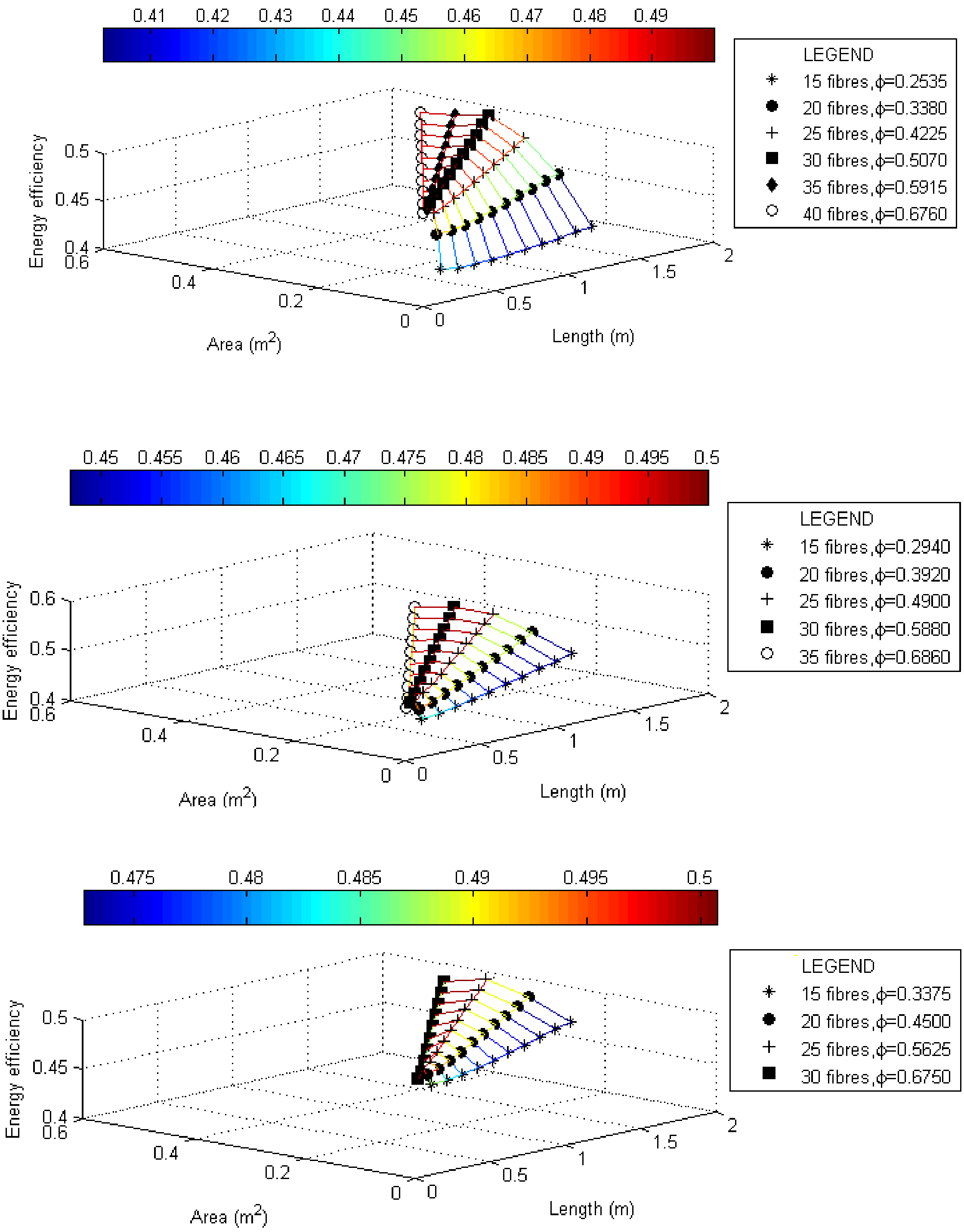

Figure 5-16 Influence of packing density and module size on module energy efficiency under HICO operating mode; A - Top, d$_f$ =1.8mm; B - Middle d$_f$ =2.0mm; C –Bottom d$_f$ =2.2 mm; ($\dot{m}_f = \dot{m}_p = 0.055\ kg\ s^{-1}$; T$_{f,in}$ = 343K and T$_{p,in}$=298K, NaCl concentration=2 w/w %)

Examining Figure 5-16, the variation in energy efficiency obtained for the specified operating conditions lies between 0.4-0.5. In all Figure 5-16A-C, it is evidenced that the energy efficiency is at its highest at packing density of about 0.5.

5.4.3. The influence of length and module area on DCMD-HFM performance

The influence of length and module area can be observed in most of the figures given in Section 5.4. From Figure 5-5 to Figure 5-6 and Figure 5-9 to Figure 5-11, it is evidenced that transmembrane flux decreases significantly as the module is made longer. As the feed cools down further along a longer module, due to the non-linearity between water vapour pressure and temperature, the driving force across the membrane decreases significantly, resulting in lower flux. Examining other figures, it is found that module length does not have a huge impact on a module’s thermal efficiency or energy efficiency.

Figure 5-17 examines production rate. As expected, modules with a higher packing density or of great length, have a higher production rate, due of course to the increase in membrane area. Although the curves start to flatten there was no approach to a plateau for the range of conditions investigated. Smaller fibres also favour a higher module production rate.

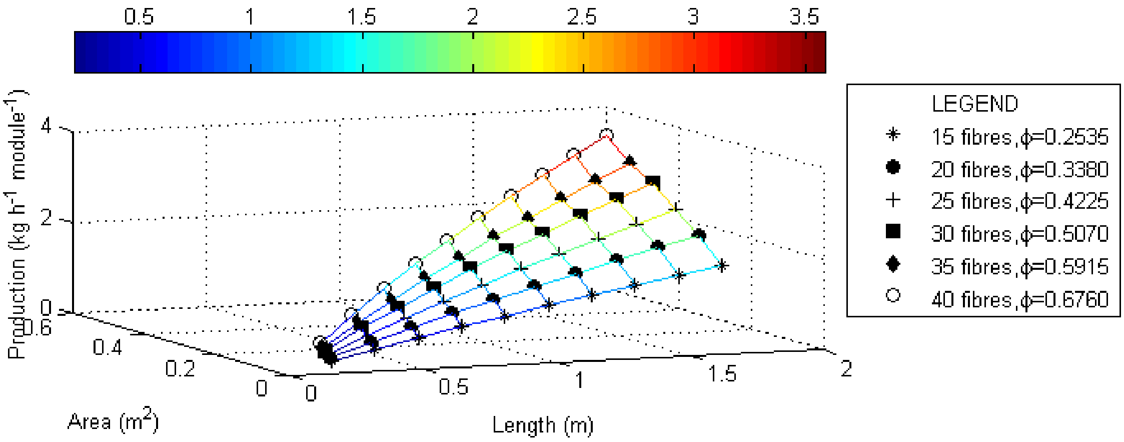

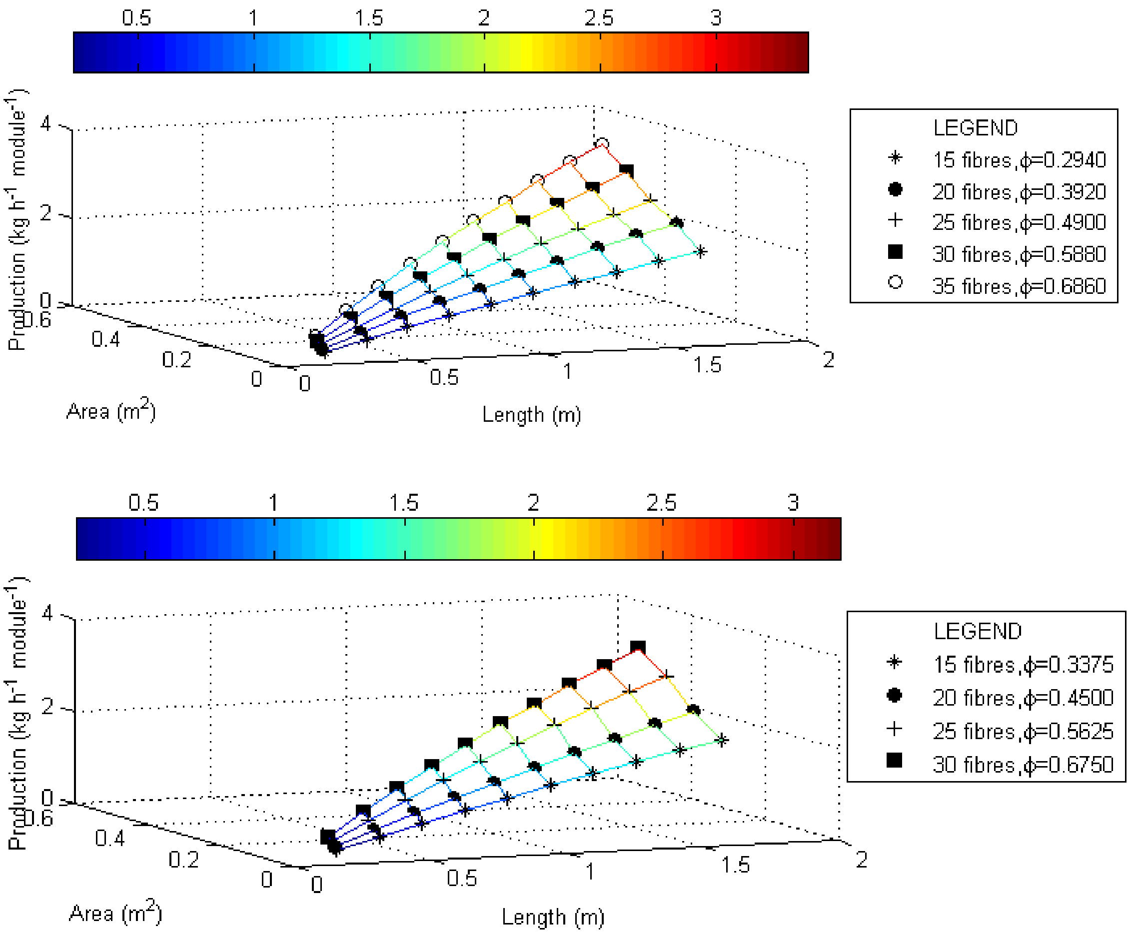

Figure 5-17 Influence of packing density and module size on module production rate under HICO operating mode; A - Top, d_f =1.8mm; B - Middle d_f =2.0mm; C –Bottom d_f =2.2 mm; ($\dot{m}_f = \dot{m}_p = 0.055\ kg\ s^{-1}$; $T_{f,in}$ = 343K and $T_{p,in}$=298K, NaCl concentration=2 w/w %)

The feed outlet temperature with respect to module length and various packing density is plotted as shown in Figure 5-18. It shows that more heat is carried to the permeate side as the membrane area increase. It is important to point out that the lines on the plot are relatively straight, which suggests a very small rate of change of curvature. Moreover, the overlapping of the lines suggests that the downward gradient of each curve is similar. Recalling heat exchanger design and the E-NTU method which was described in Chapter 4, this observation suggests that the overall heat transfer coefficient in this case remains approximately constant, regardless of module length and packing density is only a weak function of module length and packing density. In this case, the overall heat transfer coefficient is found to be 280 W m^{-2} K^{-1} for the flow conditions investigated. This realization is very helpful with system design as demonstrated in the next Chapter.

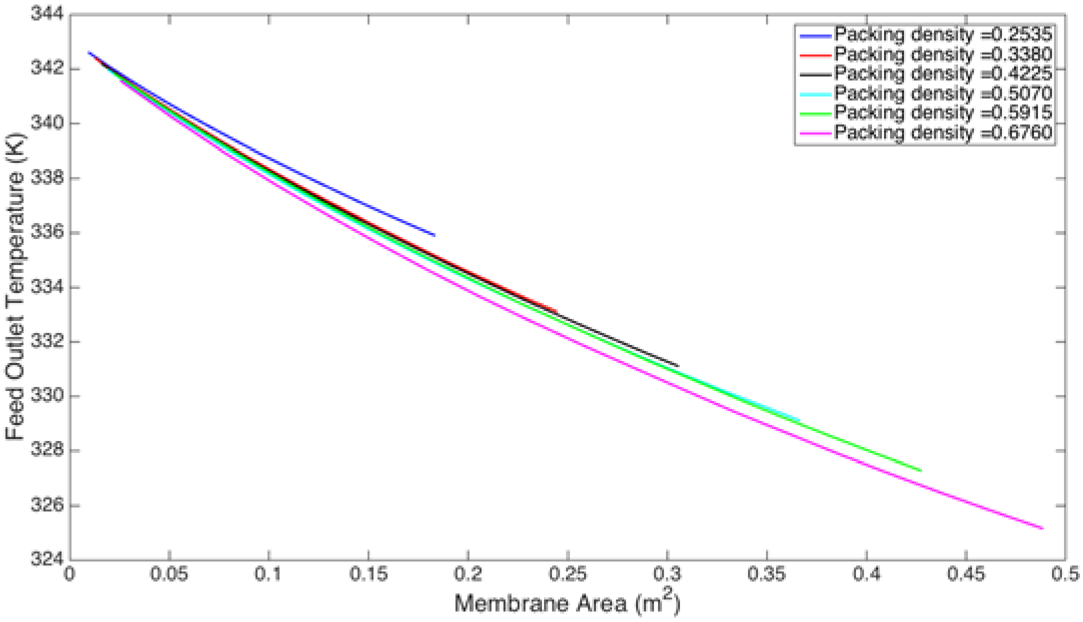

Figure 5-18 Effects of membrane area and packing density on the temperature of the feed outlet. (d$_f$=1.8mm, $\dot{m}_f = \dot{m}_p = 0.055\ kg\ s^{-1}$; T$_{f,in}$ = 343K and T$_{p,in}$=298K)

5.5. Chapter summary

This chapter provides a thorough investigation of various design features and specifications on DCMD-HFM module performance. With a validated model that considers maldistribution introduced by random packing, our simulation results show that:

(i) Both transmembrane flux and thermal efficiency improve with the hot feed flowing on the lumen side of the fibres (HICO flow configuration);

(ii) With HICO mode, both transmembrane flux and thermal efficiency show very little variation with respect to packing density;

(iii) At the same packing density, small fibres result in a moderately higher pressure drop;

(iv) A packing density of around 0.5 results in the lowest pressure drop (per unit length) and subsequently the highest energy efficiency;

(v) Apart from transmembrane flux which decreases significantly as the module gets longer, both thermal efficiency and energy efficiency are insensitive to the variation in module length;

(vi) Since module production rate increases with membrane area, modules with a smaller fibre diameter have a higher production rate;

(vii) According to our examination on the effect of module length and packing density on feed outlet temperature, it is suggested that overall heat transfer coefficient of our module remains approximately at 280 W m^{-2} K^{-1} for the operating conditions investigated.

6. Implementation of DCMD in rural arid regions requiring desalination

6.1. Introduction

"According to World Health Organization (WHO), between 50 and 100 litres of water per person per day are needed to ensure that most basic needs are met and few health concerns arise" (UN, 2014).

With the scenario of aiming to provide a family's daily need of potable water, this chapter proposes a DCMD system flowsheet that would deliver 500L of water per day, assuming the use of solar energy with planned operation restricted to 8 hours per day. Additionally in view of the lack of reports in the literature on Aspen Plus process simulation with customized MATLAB models, a second emphasis in this chapter is dedicated to introducing methods that allow one to combine the simulated result obtained from our DCMD-HMF MATLAB model (as described in the previous chapter) with an Aspen Plus flowsheet.

6.2. Approach and considerations

Opting for a simple and robust design that fits the application, this work investigates a basic single stage (no cascading) DCMD process that considers only the necessary elements required for any MD processes. This work does not have an emphasis on solar power incorporation and steady supplies of heat and electricity supplies during the hours of operation are assumed.

To achieve our objective, the hierarchical design procedure summarized in Table 6-1 is proposed. The design specifications were firstly identified, followed by the design of the MD unit. The module specifications used were based on the results obtained from our rigorous DCMD-HMF model developed in the previous chapter. The module size and flowrates across the modules were estimated and a flowsheet is simulated using Aspen Plus.

Regarding brine disposal, to keep the system simple and to reduce the energy consumption, no crystallizer is included in the proposed flowsheet. Typically for remote RO systems, due to the concentration of the brine, direct brine discharge of brine to the soils is infeasible due to salinization resulting in soil degradation. The discharged brine could be used for fish farming, spirulina cultivation and irrigation of forage shrub and crops (Sánchez, et al., 2015). For rural regions where land is plentiful, leaving brine in evaporation ponds is another favourable option as they are relatively easy to construct and require low maintenance and little operator attention (Morillo, et al., 2014).

Table 6-1 Hierarchical design levels in an DCMD process

Design stage	Descriptions
0	**Initial design specifications**
I	**Design of MD unit**
II	**Flowsheet design and simulation**
III	**Feed stream, recycle stream considerations**

6.3. Initial design specifications

Table 6-2 contains all the fixed design specifications. It is assumed that the brackish groundwater supplied to the system only requires desalination, without any other treatments.

Table 6-2 Initial design specifications for the overall process

Fixed input parameter	
Brackish water concentration	**1% (w/w%)**
Brackish water temperature	**291 (K)**
Fixed output demand	
Permeate production rate[5]	**62.5 kg h^{-1}**

6.4. DCMD units specifications

The module specifications are calculated based on the DCMD-HMF model developed in Chapter 5, adopting the same membrane parameters and hydrodynamics conditions. Table 6-3 below lists the basic parameters and design features adopted:

Table 6-3 Membrane module parameter adopted from previous chapter

Membrane module characteristic	
Packing density	0.5
Fibre inner diameter	1.8 mm
Fibre and module length	1.7 m

According to Figure 5-17A, a module with 30 fibres, each of 1.7 meter long, could produce approximately 2.6 kg of pure water per hour. Hence for a throughput of 62.5 kg h^{-1}, a module size which is 24 times bigger (i.e. with 720 fibres) is required. Scaling up the flowrates and module size accordingly using dimensionless analysis and keeping all

---

[5] Calculated using by dividing the required throughput, 500L day^{-1}, by operational time, 8 h day^{-1}

the dimensionless numbers constant, the design and operational specifications of the required DCMD unit is presented in Table 6-4. To validate the calculations, the specifications listed in Table 6-4 were inputted into the MATLAB model, and the simulated results are given in Table 6-5.

Table 6-4 DCMD unit specification

Number of fibres	720
Module inner diamter	98 mm
Mass flowrates	1.32 kg s^{-1}
$T_{f,in}$	343 K
$T_{p, in}$	298 K

Table 6-5 DCMD unit simulated output

Packing density	0.5068
Total membrane area	8.33 m^2
Production rate	62.56 kg h^{-1}
Permeate flux	7.52 kg m^{-2} h^{-1}
$T_{f,out}$	312 K
$T_{p, out}$	328 K
Thermal efficiency	0.56
Energy efficiency	0.49

6.5. Flowsheet design and simulation

6.5.1. Overview of the flowsheet

The desalination scheme proposed was simulated using ASPEN plus and presented in Figure 6-1. The key features and components included in the flowsheet were:

(i) One DCMD-HFM in which the hot saline stream (sent to the upper side of the module) and the cold stream (sent to the lower side of the module) flow counter-currently;

(ii) One heater for the recycle stream on the feed side;

(iii) One heat recovery device (heat exchanger HX), used to exchange heat between the warmed permeate stream and the brackish water feed from the ground; and three splitters and two mixers. These are simple components such as mixing tees and overflow devices.

While the pumping loss and cost were estimated in the previous chapters, opting for a simpler flowsheet, pumps were not included in the ASPEN simulation.

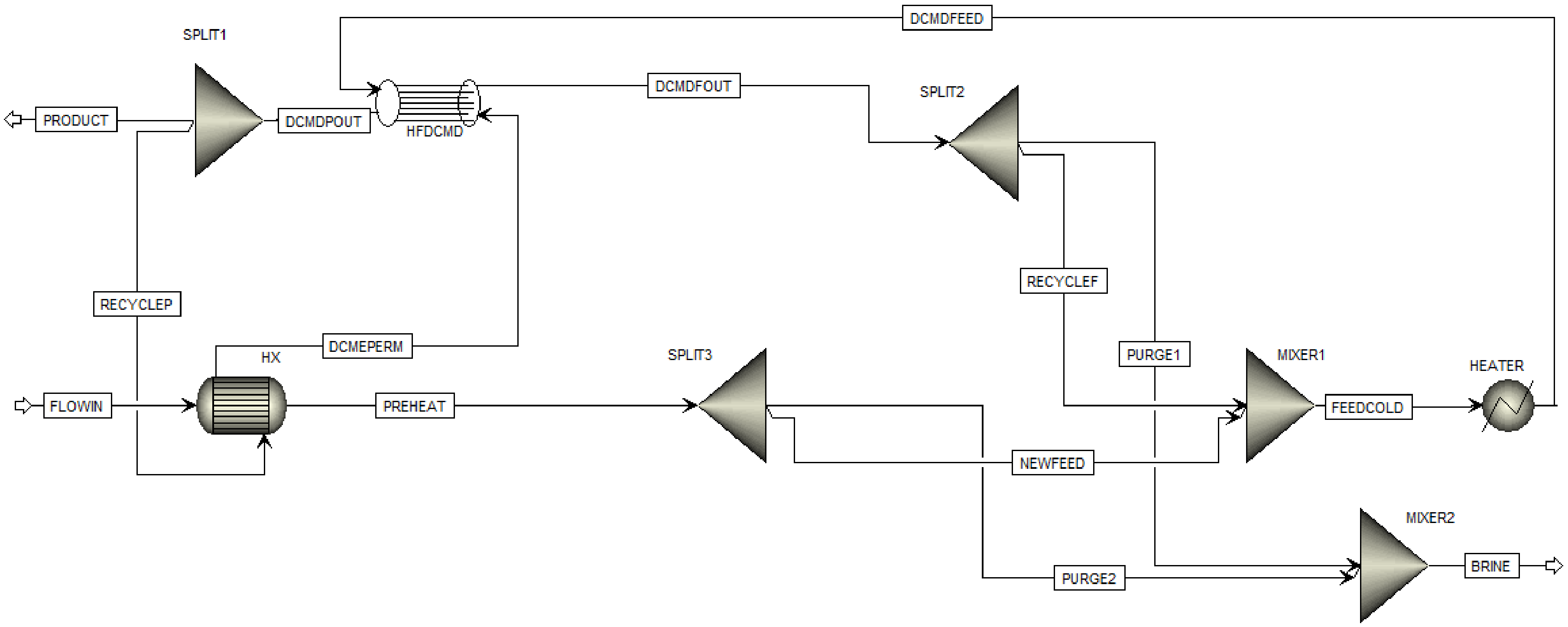

Figure 6-1 Flowsheet for DCMD desalination system, constructed using Aspen Plus.

6.5.2. Constructing a DCMD-HFM module for Aspen Plus simulation

While there are many preinstalled operational blocks and models in Aspen Plus Model Palette, including most of the commonly used flowsheet components, in order to simulate a DCMD process in Aspen Plus, a customised DCMD module is required. So far, all the literature reporting the use of Aspen Plus for MD process simulation use a customized MD model built using Fortran. Adopting another approach, we have explored three ways, with different rigorousness and versatility, to incorporate the simulation results from our DCMD-HFM MATLAB model, described in the previous chapter, into Aspen Plus.

6.5.2.1. Method 1: Aspen Plus – MATLAB interface

Out of the three methods, Method 1, depicted in Figure 6-2, is the most rigorous and versatile one. An interface is created via Microsoft Excel Visual Basic Application (VBA) to directly bridge the MATLAB model with the Aspen Plus. The interface allows variables defined in Aspen to be imported to MATLAB and once the simulation from MATLAB is completed, the interface exports the simulated results back to Aspen. Details of the programming of this customized model and the interface, including the User Array Data and Setting up of the model in Excel Workbook, are provided in Appendix B. The data that are exchanged between Aspen Plus and MATLAB are listed in Table 6-6.

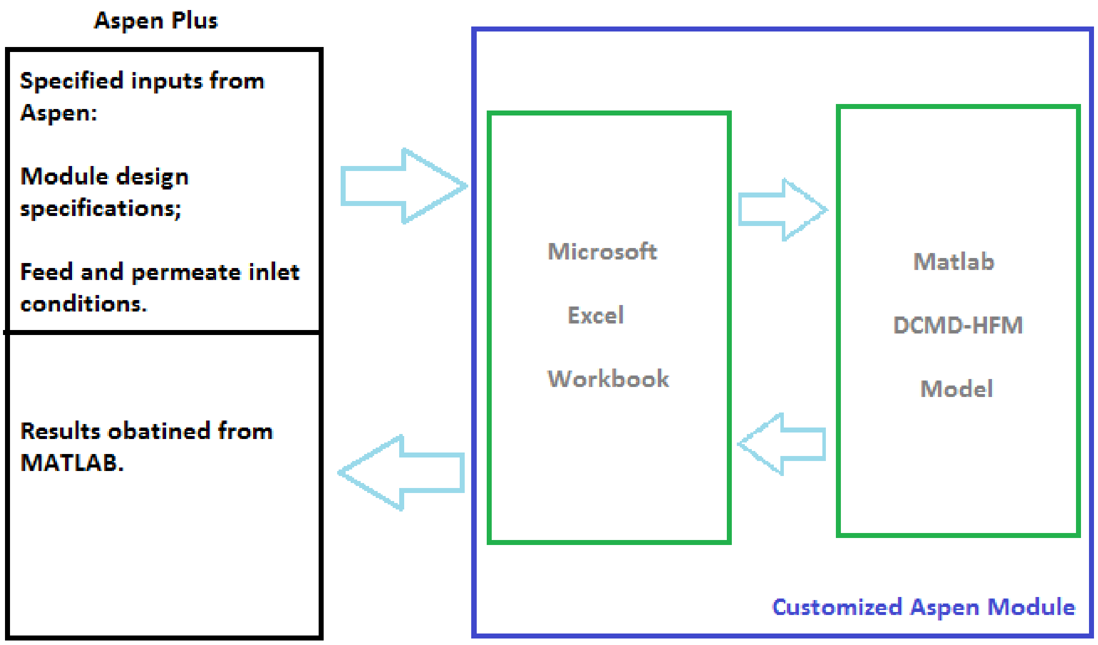

Figure 6-2 Simulation framework of Aspen Plus and MATLAB interface

Table 6-6 Variables imported and exported between Aspen Plus and MATLAB

Aspen to MATLAB	MATLAB to Aspen
Number of Fibres	Feed flowrate at outlet (kg s^{-1})
Module length (m)	Feed outlet temperature (K)
Module packing density	Permeate flowrate at outlet (kg s^{-1})
Fibre inner diameter (m)	Permeate outlet temperature (K)
Feed mass flowrate (kg s^{-1})	Updated fluid thermodynamic conditions
Feed inlet temperature (K)	
Feed salinity (w/w%)	
Permeate mass flowrate (kg s^{-1})	
Permeate outlet temperature (K)	
Thermodynamics condition calculated by Aspen Plus	

While this method is relatively versatile as a range of inputs can be defined in Aspen and simulated rigorously with MATLAB, due to the multiple interface communications and computational demand, as documented in Appendix B, each simulation takes a relatively long running time. The long simulation time is especially undesirable when tear streams or recycled streams are included in the flowsheet simulation (see Section 6.5.3). Multiple iterations are needed for converged solutions. Hence Method 2 and Method 3 are introduced which provide quicker estimations in considerably shorter simulation time.

6.5.2.2. Method 2: Customized model using Microsoft Excel with pre-run results from MATLAB

Aiming to reduce simulation time, an alternative method is introduced in this section which allows the results produced from the MATLAB model to be incorporated into the process flowsheet while eliminating the interface computational time between the Excel Workbook and MATLAB.

This can be achieved by preparing an extensive look-up table, containing the results simulated from MATLAB with various combinations of possible values as input parameters, in Microsoft Excel prior to Aspen Simulation. Once Aspen passed the defined variables onto Excel, including the module design specifications and the thermodynamic properties of the fluids, Excel would ‘look up’ the corresponding result stored in the look-up table in an Excel workbook. More details on the features and coding regarding Method 2 are included in Appendix C. It is worth pointing out that sometimes it is impossible to have pre-run result readily stored with the exact input values (input valuables between Aspen iterations is corrected to 4 d. p.); as a result the minimum difference between each Aspen defined input values and their corresponding MATLAB input values are evaluated and matched.

Compared to Method 1, Method 2 is less rigorous as sometimes the exact values of the parameters could not be matched. Method 2 is also less versatile since the MATLAB model has to be pre-run prior to Aspen Plus flowsheet simulation. However the overall simulation time is significantly reduced.

6.5.2.3. Method 3: DCMD performance estimation without a customized model

Both Method 1 and 2 incorporates a customized DCMD-HFM model into the flowsheet, exporting the results obtained from the rigorous MATLAB model to Aspen. By contrast Method 3 gives a good performance estimation without the need to create a customized model. Instead the behaviour of a DCMD module is mimicked or estimated by a network of a few pre-installed model blocks from Aspen Model Palette, as shown in Figure 6-3.

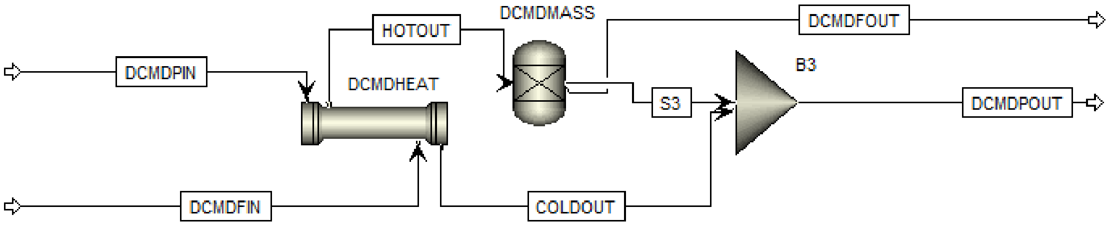

Figure 6-3 Network of pre-installed model blocks in Aspen Plus for estimating DCMD-HFM performance

In Figure 6-3, there are three operational blocks which are labelled as: DCMDHEAT; DCMDMASS and B3. DCMDHEAT is a countercurrent flow heat exchanger which delivers the heat exchange from the hot feed to the cool permeate in the DCMD module; DCMDMASS is a separator which separates the transmembrane permeate from the hot stream; and finally B3, which is a mixer, mixes the abstracted transmembrane permeate with the cold permeate stream that has been estimated to pass through DCMDHEAT. In order to simulate the flowsheet depicted in Figure 6-3, apart from specifying the inlet streams, the basic design requirements of each operational block have to be specified, as reported in Table 6-7.

Table 6-7 Specifications of the Aspen blocks used in modelling DCMD-HFM

BLOCK ID: DCMDHEAT (heat exchanger)	
Specifications	**Selection or Value (unit, as defined in Aspen Plus)**
Calculation	Shortcut
Flow direction	Countercurrent
Exchanger area	8.33 (sqm)
Minimum temperature approach	5 (K)
U Methods [6]	U value: 280 (Watt/sqm-K) (adopted from section 5.4.2)
BLOCK ID: DCMDMASS (separator)	
Outlet stream	S3
Substream	MIXED
Component: WATER	Flow; Mass; 0.0028 (kg/sec) #
Component: NaCl	Flow; Mass; 0 (kg/sec)
BLOCK ID: S3 (mixer)	
Pressure	1 (bar)
Valid phases	Liquid-Only
# Selection is explained in the following paragraphs.	

While an initial value is inputted for the water flowrate in stream S3, it is only an initial estimation. To model the heat and mass transfer co-dependency in MD system which varies according to the module size, a design specification (under Flowsheeting

---

[6] U refers to the overall heat transfer coefficient

Options) is specified for the mass flow rate of S3. Recalling the E-NTU method introduced Chapter 4 of this thesis, the transmembrane mass flowrate can be estimated when the overall heat transfer coefficient of the DCMD system is given or evaluated; the heat duty of the module is known; and the thermal efficiency can be determined. Figure 5-7 in the previous chapter shows that the variation in the overall thermal efficiency of the DCMD-HFM is very small, and can be approximated to 0.55. Consequently, a design specification is defined for the water flowrate in stream S3 which varies according to heat duty of DCMDHEAT. More details regarding design specification are described in Section 6.5.3 and summarised in Table 6-9.

To validate the model presented in Figure 6-3, the result obtained is plotted against the simulation result generated from out MATLAB model, as presented in Figure 6-4. Good alignment between the results is observed which suggests that with the design specifications and operational conditions used, this Aspen model is a suitable to be used for Aspen DCMD process simulation. Since Method 3 does not require any interface with other software packages, compared to Method 1 and 2 the computational time required for each simulation is much shorter.

It is important to note that this model should always be used with cautions and validated prior to use especially when the operational conditions are changed. The value of 0.55 was determined for countercurrent HICO mode. For other arrangements moderately different values should be used.

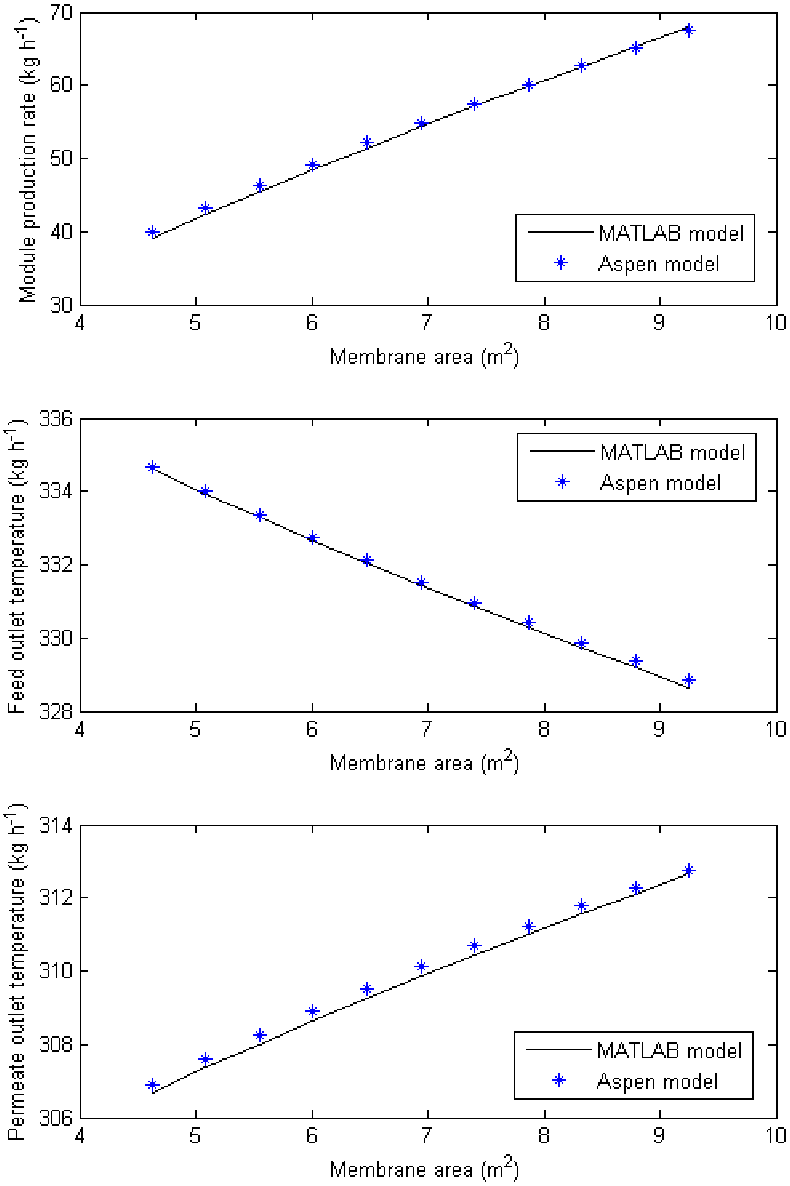

Figure 6-4 Results obtained from DCMD-HFM simulation using MATLAB and Aspen.

6.5.3. Model and design specifications for the flowsheet

Figure 6-5 shows the DCMD flowsheet created without employing a customized module but built only with the pre-installed model from Aspen, as described in the previous section.

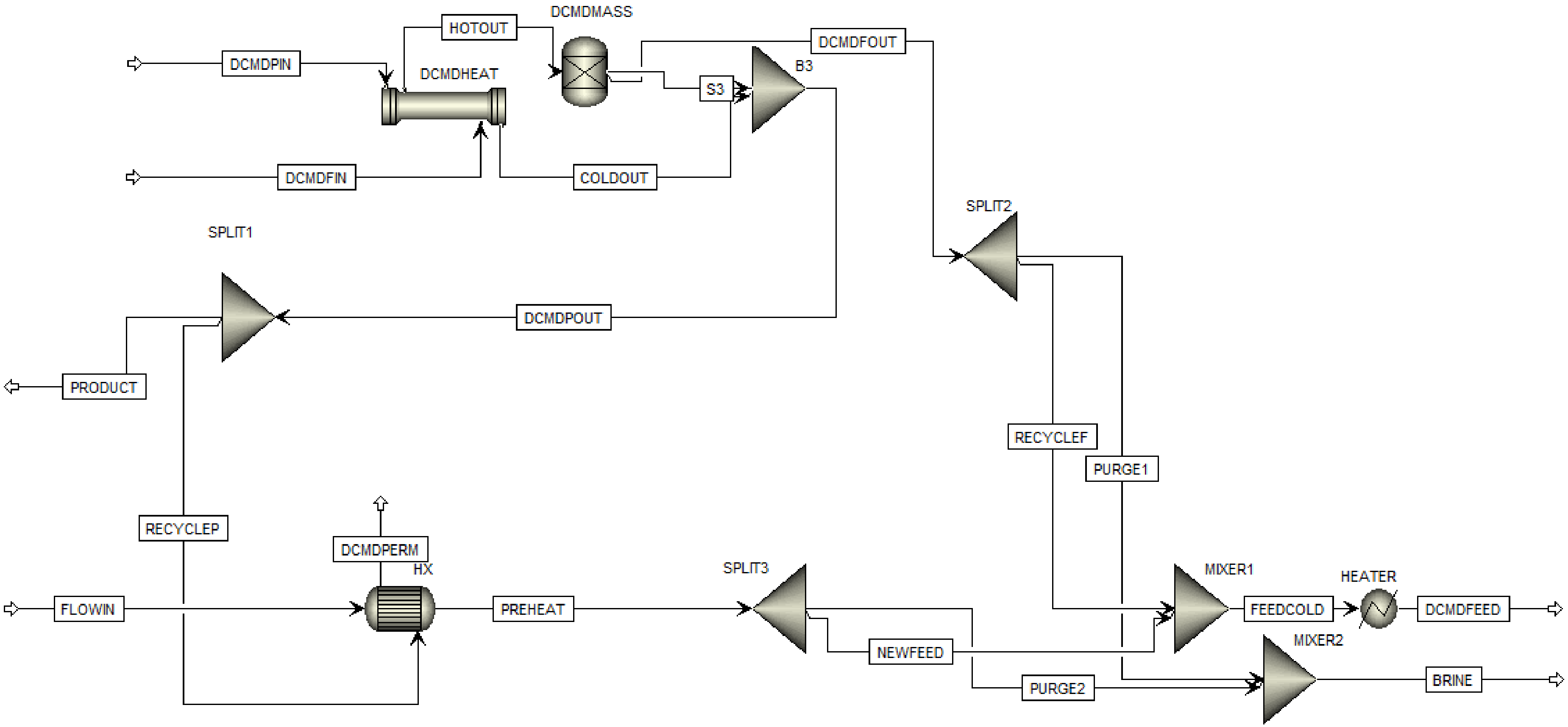

Figure 6-5 Flowsheet for DCMD desalination system, showing the Aspen model for DCMD and the tear streams for simulations. See text for comments on DCMDPIN, DCMDFIN, DCMDPERM and DCMDFEED

Compared to Figure 6-1, the recycle streams observed in the flow sheet in Figure 6-1 are removed. Instead another two streams, namely DCMDPIN and DCMDFIN are used to supply the hot saline feed and cool permeate into the DCMD module, which are supposed to have identical properties as DCMDPERM and DCMDFEED respectively. Typically, Aspen Plus handles recycle streams using a feature called ‘tear streams’. The ‘tear’ replaces a recycle stream by estimating initial values for the stream where it enters a block, then allows the solver to progress through the flowsheet until the results converge. Instead of using the ‘tear streams’ feature installed in Aspen, the compositions of the two pairs of tear streams were specified using a design specification (another Aspen Plus feature) in this case of feed circulation, and controlled by the heat exchanger for permeate circulation. This feature enables one to specify demands/ requirements for a specific block or stream with Aspen Plus altering a user-specified variable to satisfy that demand.

While only NaCl and water are presented in the system, prior to simulation Aspen Plus requires the user to specify a modelling method. IDEAL is selected in this case for there are no reactions are involved in our simulation.

Moreover apart from the blocks included for modelling the DCMD-HFM model described in the previous section, the function and specification of the other blocks are included in Table 6-8. Furthermore, all design specifications used are listed in Table 6-9 below. Unless an error is presented, Aspen would perform multiple iterations until all the design specifications are met for every simulation.

Table 6-8 Aspen blocks model specifications

BLOCK ID: SPLIT 1 (splitter)	
Purpose: Separating the product from the permeate stream	
Specifications	**Selection or Value (unit, as defined in Aspen Plus)**
Stream: RECYCLEP	Flow: Mass = 1.32 kg s^{-1}
BLOCK ID: SPLIT 2 (splitter)	
Purpose: Splitting the feed stream into recycle stream and purge stream	
Stream: PURGE 1	Split ratio: 0.1 #1
BLOCK ID: SPLIT 3 (splitter)	
Purpose: Splitting the stream into two streams: (a) NEWFEED, to replace the flow being purged ; (b) PURGE2, which is mixed with the excess brine and disposed of.	
Stream: NEWFEED	Flow: Mass = 0.1 kg s^{-1} #2
BLOCK ID: HEATER (heater)	
Purpose:	
Temperature	343.15 (K)
Pressure	1 bar
Valid phases	Liquid Only
BLOCK ID: HX (heat exchanger)	
Purpose: Remove the heat from feed stream, preheat the newcoming feed	
Calculation	Shortcut
Flow direction	Countercurrent
Type	Design
Specification	Hot stream outlet temperature: 298K
Minimum temperature approach	5 (K)
U Methods	Phase specific values
BLOCK ID: MIXER 1 (mixer)	
Purpose: Simple mixing of the 2 incoming streams	
-	
BLOCK ID: MIXER 2 (mixer)	
Purpose: Simple mixing of the 2 incoming streams	
-	
#1 Initial selections, more considerations are provided in the following section. #2 Initial selections, it is varied according to Design specification 2 (see Table 6-9).	

Table 6-9 Design specifications used in the flowsheet.

Design specification 1: Calculating the DCMD-HMF module production according to the heat duty of the heat exchanger DCMDHEAT
Specification: The split ratio of DCMDMASS
Specification target: 0.55*heat duty of DCMDHEAT (in J kg^{-1}) /2380000[7]
User defined variable to achieve target: Controlling the mass flowrate of stream S3 with DCMDMASS
Design specification 2: Ensure the mass flowrate of DCMDFEED is approximately 1.32 kg s^{-1} (as specified for DCMDFIN initially)
Specification: Mass flowrate of DCMDFEED
Specification target: 1.32 kg s^{-1}
User defined variable to achieve target: Vary SPLIT3 block variable- changing mass flowrate of NEWFEED
Design specification 3: Ensure the amount of NaCl is the same in DCMDFIN and DCMDFEED (Recycle stream in reality)
Specification: Mass of salt in DCMDFIN
Specification target: Mass of salt in DCMDFFEED
User defined variable to achieve target: Mass of salt presented in DCMDFIN

---

[7] 2380000 is the heat of vaporisation of water in J kg^{-1} at 323K. ((Howatson, et al., 1973)

6.6. Sensitivity analysis on feed flowrate and recycle ratio

According to Figure 6-1, FLOWIN is the only feed stream in the system. Its properties are given in Table 6-2. It is observed that the mass flowrate of FLOWIN is determined by the heat that needs to be removed from RECYCLYP and the amount of new feed to the DCMD loop, which is dependent on the recycle to purge ratio determined by SPLIT2.

To assess the minimum flowrate required for the heat exchanger, HX, to operate as specified, a sensitivity analysis is carried out using Aspen and the result is presented in Figure 6-7. As pointed out in the figure, an error message was presented when the flowrate was suggested to be below 1.2kg s^{-1}, which is the minimum flow necessary for the required heat duty. As suggested from the plot, it is clear that excess mass flow reduce the preheating effect on stream, PREHEAT, while a higher flowrate would also incur a higher pumping cost (which is not reflected in the plot). Thus, for operation a flow rate of 1.2kg s^{-1} should be chosen.

Figure 6-6 shows the influence of changing purge flowrate (determined by SPLIT 2). It is observed that the heating requirement is directly proportional to the purge quantity while a plateau is suggested for salt concentration in the circulation feed. As the recovery rate of a DCMD module is very small, the salt concentration remain fairly low. Thus according to the figure, an energy efficient system should aim to have as high recycle rate as possible. A purge stream is not necessary as batch system could be adopted with purging and filling up the tank manually at the end of the operation time. For a continuous system, recycling 95% of the flow, the information for each stream is displayed in Table 6-10.

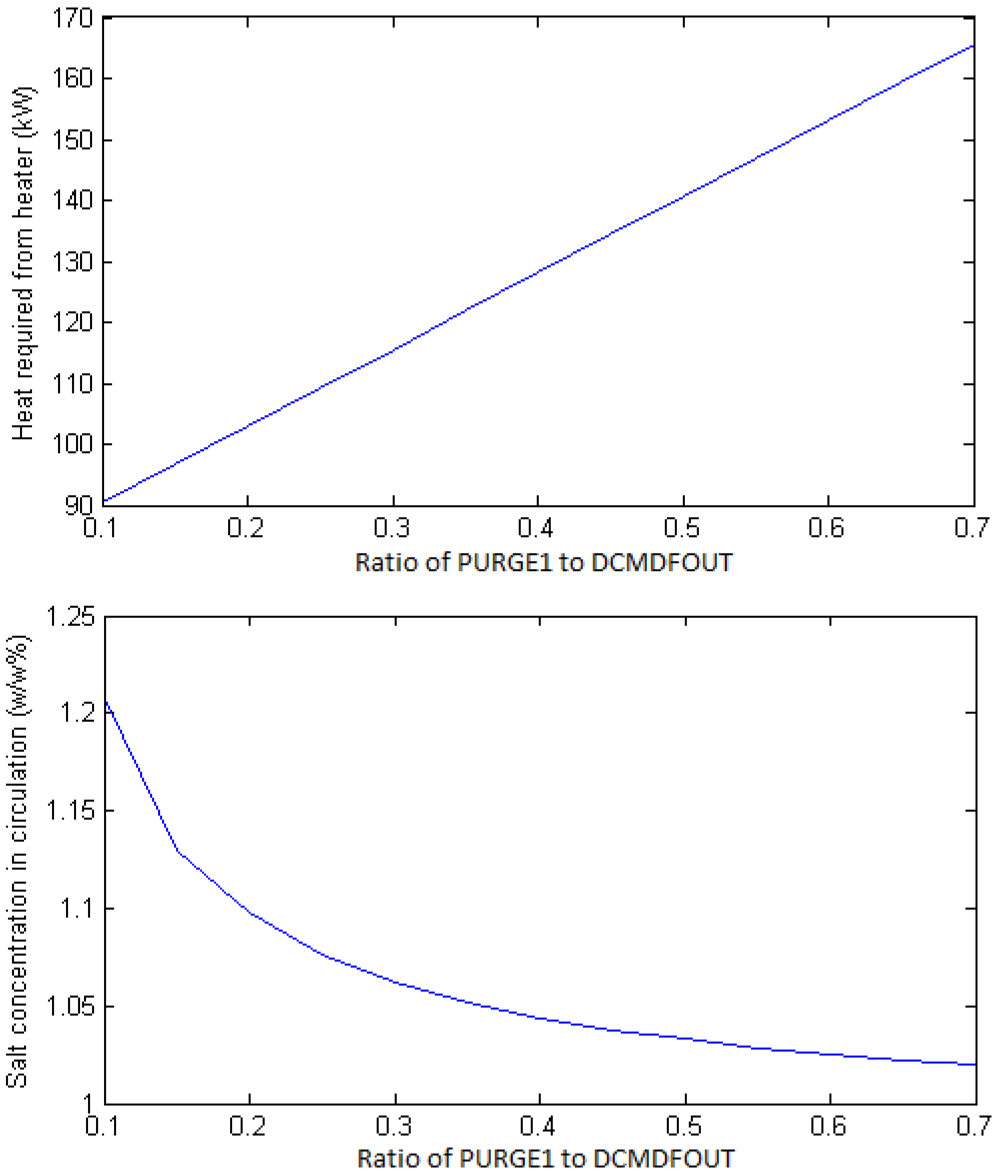

Figure 6-6 The influence of ratio of PURGE1 to DCMDOUT to: (top) heat required from the heater, and salt concentration in circulation

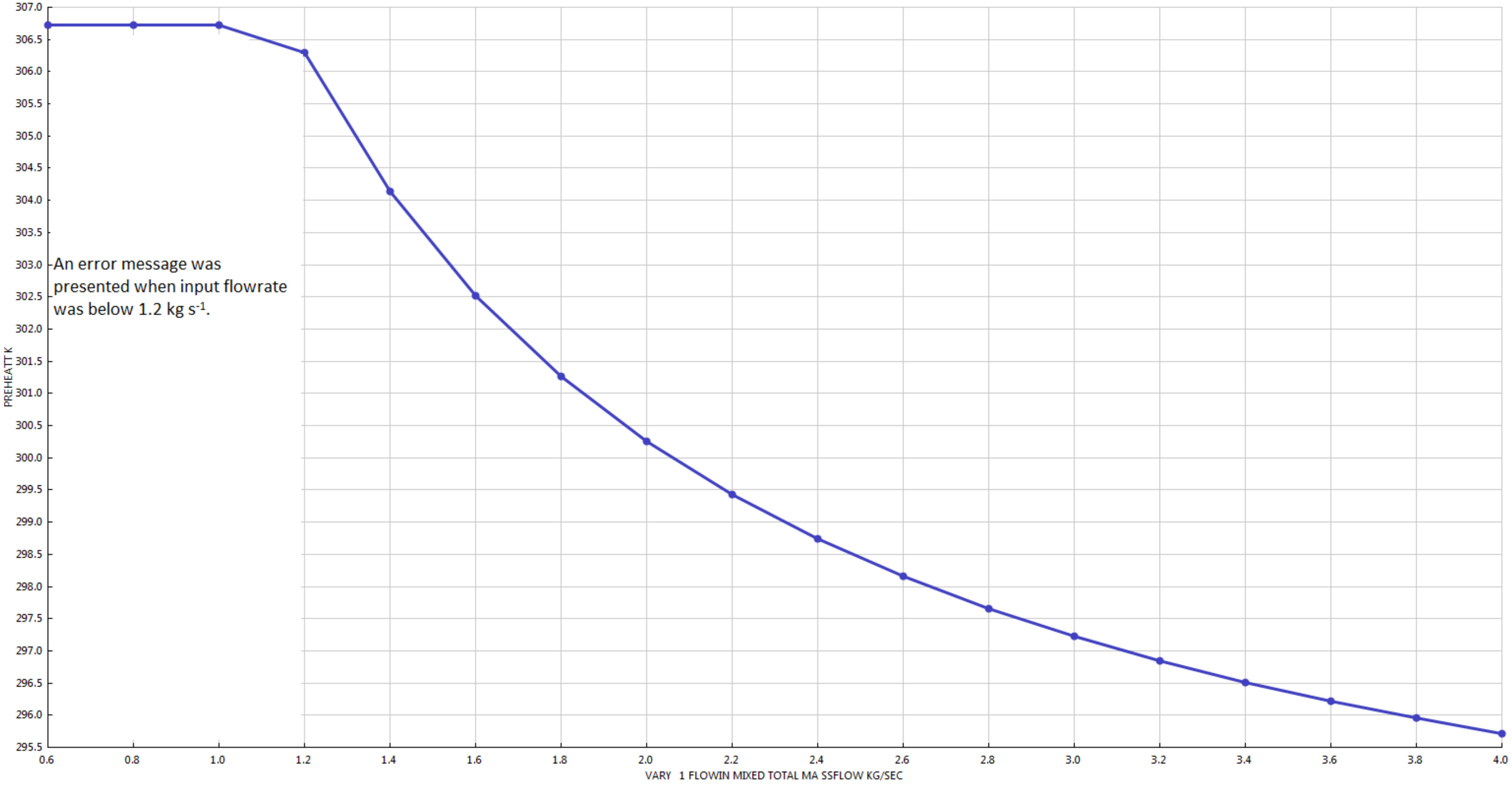
An error message was presented when input flowrate was below 1.2 kg s^{-1}.

Figure 6-7 Sensitivity results curve: the corresponding temperature change in stream PREHEAT with the flowrate of FLOWIN

Table 6-10 Simplied stream table obtained from Aspen flowsheet simulation.

Stream	BRINE	COLDOUT	DCMDFEED	DCMDFIN	DCMDFOUT	DCMDPERM	DCMDPIN
Temperature K	307.6	311.5	343.1	343	329.7	298.1	298
Mass Flow kg/sec	1.165	1.32	1.331	1.314	1.296	1.32	1.32
WATER	1.153	1.32	1.311	1.294	1.276	1.32	1.32
NACL	0.012	0	0.02	0.02	0.02	0	0
Stream	DCMDPOUT	FEEDCOLD	FLOWIN	HOTOUT	NEWFEED	PREHEAT	PRODUCT
Temperature K	311.7	327.9	291.1	329.7	306.3	306.3	311.7
Mass Flow kg/sec	1.337	1.331	1.2	1.314	0.1	1.2	0.017
WATER	1.337	1.311	1.188	1.294	0.099	1.188	0.017
NACL	0	0.02	0.012	0.02	0.001	0.012	0
Stream	PURGE1	PURGE2	RECYCLEF	RECYCLEP	S3		
Temperature K	329.7	306.3	329.7	311.7	329.7		
Mass Flow kg/sec	0.065	1.1	1.231	1.32	0.017		
WATER	0.064	1.089	1.212	1.32	0.017		
NACL	0.001	0.011	0.019	0	0		

According to Table 6-10, upon mixing with stream FLOWIN, the brine for disposal has a concentration of 1.03%. This is merely above the original salt concentration of the brackish groundwater. This reflects the low recovery rate across the DCMD-HMF module which is the major drawback of DCMD. Although there are rapid developments in MD technologies in recent years, especially in membrane design and fabrication, the transmembrane flux in DCMD remains low, yielding a much lower recovery ratio compared to RO. The transmembrane flux can be increased significantly by raising the operating temperature; however this will increase the heating load and cooling demand. While it is not shown in the stream table, the heating requirement for the heater is 85.2 kW according to our ASPEN simulation. This determines the solar heating requirement and the value is relatively high considering the water production rate. The overall thermal efficiency of the system could be improved in the expense of an improved heat recovery system, involving a more complicated network heat exchangers and DCMD modules. According to the chosen operation conditions, the circulating feed has a concentration of 1.52% and with the brine concentration being low and close to the original groundwater concentration, special brine treatment could be avoided. It could be used as household cleaning water or be discharged back to the reservoir/well.

6.7. Chapter summary

Based on the hollow fibre module design evaluated in Chapter 5, with appropriate scale-up, a desalination process using DCMD was presented in this Chapter. This system can supply enough potable for a family. A process flowsheet was created and simulated using Aspen Plus process simulation software. Three methods were introduced in the chapter for incorporating MATLAB result into the Aspen Plus flowsheet. According to the sensitivity analysis performed, a higher recycle rate reduces energy input required. The thermal balance dictated that 1.2 kg s^{-1} of cooling water is required to remove the heat from the circulating permeate. Finally, as the brine produced has a concentration only 0.03% higher than the original groundwater feed, it is suggested that no special treatment is required.

7. Concluding remarks and recommendation of future work

7.1. Summary and conclusions from the current work

While technologically sound and has attracted a lot of interest in research, along with numerous publications showing promising results, DCMD or MD has yet to be applied at a scale comparable to other conventional technology commercially or industrially.

All the key issues identified in Section 2.5 were addressed in other chapters of this thesis. Both experimental and analytical investigations have been carried out in order to gain a better understanding on the role of membrane thickness upon transmembrane flux. A thicker membrane increases the membrane resistance on vapour diffusion while the driving force for the transmembrane vapour flux also increases with the temperature difference across the membrane. These opposing effects give rise to an optimal membrane thickness which would yield the highest transmembrane flux as shown in the analytical investigation presented in Chapter 3.

Membranes of various thicknesses, between 28μm to 58μm, were fabricated using electrospinning with spinning time of 4-10 hours followed by heat post-treatment. A structural deviation factor is introduced to account for the structure differences between the thinner and thicker membranes. The experimental observations show that higher fluxes were obtained using thinner membranes. It had been hoped to produce sufficiently thin membranes for the investigation of optimal membrane thickness. Although thinner membranes could be fabricated using the same method, their DCMD performance could not be tested due to the weak mechanical strength. Instead, using a validated MATLAB discretization DCMD model, an excellent fit was achieved between the model and our experimental data, and the model suggests a maximum flux with a membrane thickness of around 10 µm. This is in good agreement with the analytical model.

Analytically, an expression for the theoretical optimal membrane thickness was derived algebraically and solved graphically. The analytical model shows that the value of optimal thickness varies with salinity. When the salinity was at 10% w/w, the optimal value of membrane thickness was found to be around 13µm. Moreover it was found from our analytical analysis that when pure water is used as feed, the optimal membrane thickness obtained is around 0.4µm, which is an unrealistic value regarding practical interest.

The evaluation on optimal membrane thickness along with the reassessment on dusty gas model for the mass transfer in DCMD in Chapter 4 satisfy the scientific and academic interest, the E-NTU method modified DCMD modules presented in Chapter 4 provides a simplified and effective way of designing DCMD modules. The algorithms introduced and the set of equations that were derived in the same manner as those derived for the use of heat exchanger systems enable good performance or sizing estimations to be obtained for DCMD modules. With the introduction of a correction function that accounts for the unequal contribution to performance by the two heat transfer coefficients, estimations obtained are within 6% of our MATLAB discretization model.

Chapter 5 in this thesis provides a thorough investigation of various design features and specifications on DCMF-HFM module performance using a validated MATLAB model. Compared to most published literature that has assumed uniform flow, flow maldistribution due to random packing has been accounted in our model. The effects of flow configuration, length, fibre size and the number of fibres in the module on module performance, including transmembrane flux, thermal efficiency, module production rate and energy consumption, were investigated. Our results suggest that without using any flow enhancement devices, both transmembrane flux and thermal efficiency improve with hot feed flowing on the lumen side of the fibres (HICO flow configuration and with HICO mode, both transmembrane flux and thermal efficiency show very little variation with respect to packing density. Moreover, a packing density of around 0.5 results in the lowest pressure drop (per unit length), subsequently the highest energy efficiency whilst with the same packing density, small fibres result in a moderately higher pressure drop. Furthermore, apart from transmembrane flux which decreases significantly as the module gets longer, both thermal efficiency and energy efficiency seem insensitive to the variation in module length.

The flowsheet design included in Chapter 6 can serve as a design tool and be used as a base model for the implementation of DCMD in rural arid region. Based on the hollow fibre module design evaluated in Chapter 5, with appropriate scale-up, a desalination process using DCMD was presented. This system can supply enough potable for a family. The flowsheet was constructed using Aspen Plus and multiple ways were explored for incorporating the MATLAB simulated DCMDHFM into ASPEN. According to the sensitivity analysis, a higher recycle rate reduces energy input required. The thermal balance dictated that 1.2 kg s-1 of cooling water is required to remove the heat from the circulating permeate. The brine produced has a concentration only 0.03% higher than the original groundwater feed, it is suggested that no special treatment is required.

7.2. Recommendations of future work

Building upon the analysis on optimal thickness using electrospun membranes, further work could be done to investigate if a more generalised structural deviation factor, possibility with respect to fibre size, porosity and fibre size, could be identified for electrospun membranes. This would contribute to a better understanding and hence improved modelling of heat and mass transfer across electrospun membranes. Experimentally, similar experiments could be repeated if thinner membranes with higher mechanical strength become available. This would allow experimental observation and validation of optimal membrane thickness. Alternatively, to reduce the mechanical stress exerted onto the membrane, spacers or other support could be used for the experiment. However considerations are needed to account for the new 'apparent' membrane thickness if spacers or other mechanical support devices are to be used. As practical application are likely to involve hollow fibre modules, similar analysis on optimal membrane thickness could be extended to hollow fibres and/or dual layered membranes which provides better thermal insulation.

Secondly, as the dusty gas model has been applied to many different porous mass transfer systems, a more thorough derivation and study on the combination or each component is a scientific interest worth of deeper investigations. Moreover, proceeding on the promising results demonstrated with the proposed modified E-NTU method for the design of DCMD, the use of this modified E-NTU method for other MD configurations may be explored for future work. Additionally, as the analysis in the current work has assumed uniform flow on both sides of the membrane, for future work, a detailed assessment could be extended to crossflow modules and randomly packed hollow fibre modules.

Besides, similar investigations undertaken for countercurrent DCMDHFM could be carried out for crossflow modules in the future. Moreover, while HICO configuration demonstrates better performance, HOCI configuration is sometimes preferred depending as improved shell-side mixing and flowing distribution can be achieved by structured shell packing or winding and shell-side bubbling. A reassessment should be undertaken for HOCI configuration when any of these techniques is to be employed.

Furthermore, having successfully established the Aspen flowsheet, a more detailed and thorough system analysis including pumps and the incorporation of solar energy could be performed for future work. When solar thermal or photovoltaic equipment are taken into consideration, the operating temperature has an important role in the system efficiency, which could be explored. When adopting solar thermal energy, thermal storage should be considered for a stable and constant supply of heated feed.

Finally, water production cost (WPC) is not considered for module design assessment in this work. This is due to the lack of reported data on the cost of established system, including MD module production cost, maintenance and lifetime. Recently in a review paper that focuses on MD energy consumption and WPC (Khayet, 2013), considering the dispersion in WPC reported in literature, which varies from \$0.3 m-3 to \$130 m-3, Khayet indicated a warning, “For the benefit of MD process, one should be cautious when reporting simulated, non-realistic and non-contrasted WPC.” Hence, one should include WPC for DCMD module and system design once when more data on MD cost and longer term performance become available. As a reference and out of academic interest, a brief economic analysis using data mostly based on the economic analysis of the MD units developed through SMADES EC-funded project (Banat & Jwaied, 2008) was reported in Appendix D. A cost estimation and comparison with a solar-PV RO system of similar size is also included in the appendix. According to the calculations, it is observed that the WPC of a solar driven DCMD module are nearly 30% more than the cost of a PV driven RO, mainly due to the cost of solar panels which currently is expensive. Depending on the development of solar thermal technology, the cost of DCMD can be expected to reduce as the technology improves. Besides, depending on brine concentration and disposal method, the cost of brine disposal could offset the WPC significantly.

It is anticipated that pretreatment costs for MD will be less than those for RO and that the level of maintenance for MD might be lower than RO. While current evidence and calculations suggest that RO is superior to DCMD in the application of small-scale desalination, with the ongoing research and rapid advancement in MD technologies, it is hopeful that soon DCMD would be able to compete with RO. A more thorough analysis, including feed water pretreatments and ways of brine disposal, should be undertaken when more prolonged studies on DCMD and more reliable data on the associated manufacturing and running cost of MD systems are available in the future.

8. Bibliography

Abu-Zeid , M. A. E.-R., Y. Zhang, H. Dong, L. Zhang, H.-L. Chen, and L. Hou. “A comprehensive review of vacuum membrane distillation technique.” *Desalination* 356, no. 15 (2015): 1-14.

Alkhudhiri, A., N. Darwish, and N. Hilal. “Membrane distillation: A comprehensive review.” *Desalination* 287 (2012): 2-18.

Alklaibi, A. M., and N. Lior. “Heat and mass transfer resistance analysis of membrane distillation.” *Journal of Membrane Science* 282, no. 1-2 (2006): 362-369.

Alklaibi, A. M., and N. Lior. “Membrane-distillation desalination: Status and potential.” *Desalination* 171, no. 2 (2005): 111-131.

Al-Karaghouli, A., and L. L. Kazmerski. “Comparison of technical and economic performance of the main desalination processes with and without renewable energy coupling.” Denver, 2012.

Al-Obaidani, S., E. Curcio, F. Macedonio, G. Di Profio, H. Al-Hinai, and E. Drioli. “Potential of membrane distillation in seawater desalination: Thermal efficiency, sensitivity study and cost estimation.” *Journal of Membrane Science* 323, no. 1 (2008): 85-98.

Aspen Technology, Inc. “aspentech.” 12 2012. http://support.aspentech.com/Public%5CDocuments%5CEngineering%5CAspen%20Plus%5CV8.0/AspenPlusCustomizingV8_0-Start.pdf (accessed 4 24, 2015).

Aspentech. *Aspentech.* 2015. http://www.aspentech.com/products/aspenone-engineering/ (accessed 5 7, 2015).

Ayoub, J., and R. Alward. “Water requirements and remote arid areas: the need for small-scale desalination.” *Desalination* 107 (1996): 131-147.

Banat, F., and N. Jwaied. “Economic evaluation of desalination by small-scale autonomous solar-powered membrane distillation units.” *Desalination* 220 (2008): 566-573.

Banat, F., N. Jwaied, M. Rommel, J. Koschikowski, and M. Wieghaus. “Performance evaluation of the “large SMADES” autonomous desalination solar-driven membrane distillation plant in Aqaba, Jordan.” *Desalination* 217, no. 1-3 (2007): 17-28.

Banat, F., R. Jumah, and M. Garaibeh. “Exploitation of solar energy collected by solar stills for desalination by membrane distillation.” *Renewable Energy* 25, no. 2 (2002): 293-305.

Banchik , L. D., M. H. Sharqawy, and J. H. Lienhard V. “Effectiveness-mass transfer units (ε-MTU) model of a reverse osmosis membrane mass exchanger.” *Journal of Membrane Science* 458 (2014): 189-198.

Beeckman, J. W. “Mathematical description of heterogeneous materials.” *Chemical Engineering Science* 45, no. 8 (1990): 2603-2610.

Bilton, A. M., R. Wiesman, A. F. M. Arif, S. M Zubair, and S. Dubowsky. “On the feasibility of community-scale photovoltaic-powered reverse osmosis desalination systems for remote locations.” *Renewable Energy* 36, no. 12 (2011): 3246-3256.

Bui, V. A., L. T. T. Vu, and M. H. Nguyen. “Simulation and optimisation of direct contact membrane distillation for energy efficiency.” *Desalination* 259 (2010): 29-37.

Burn, S., M. Hoang, D. Zarzo, F. Olewniak, E. Campos, B. Bolto, O. Barron. "Desalination techniques — A review of the opportunities for desalination in agriculture." *Desalination* 364 (2015): 2-16.

Camacho, L. M., L. Dumée, J. Zhang, J.-d. Li, M. Duke, J. Gomez, S. Gray. "Advances in membrane distillation for water desalination and purification." *Water* 5 (2013): 94-196.

Chang, H., J.-S. Liau, C.-D. Ho, and W.-H. Wang. "Simulation of membrane distillation modules for desalination by developing user's model on Aspen Plus platform." *Desalination* 249, no. 1 (2009): 380-387.

Chen, V., and M. Hlavacek. "Applications of voronoi tessellation for modeling randomly packed fibre hollow bifer bundles." *AIChE Journal* 40 (1994): 606.

Chen, Y.-H., Y.-W. Li, and H. Chang. "Optimal design and control of solar driven air gap membrane distillation desalination systems." *Applied Energy* 100 (2012): 193-204.

Cheng, L.-H., P.-C. Wu, and J. Chen. "Modeling and optimization of hollow fibre DCMD module for desalination." *Journal of Membrane Science* 318 (2008): 154-166.

Costello, M. J., A. G. Fane, P. A. Hogan, and R. W. Schofield. "The effect of shell side hydrodynamics on the performance of axial flow hollow fibre modules." *Journal of Membrane Science* 80, no. 1 (1993): 1-11.

Ding, W., D. Gao, Z. Wang, and L. He. "Theoretical estimation of shell-siode mass transfer coefficient in randomly packed hollow fiber modules with polydisperse hollow fober outer radii." *Journal of Membrane Science* 284 (2006): 95-101.

Ding, Z., L. Liu, and R. Ma. “Study on the effect of flow maldistribution on the performance of the hollow fiber modules used in membrane distillation.” *Journal of Membrane Science* 215, no. 1-2 (2003): 11-23.

Ding, Z., L. Liu, M. S. El-Bourawi, and R. Ma. “Analysis of a solar-powered membrane distillation system.” *Desalination* 172 (2005): 27-40.

Drioli, E., A. Ali, and F. Macedonio. “Membrane distillation: Recent developments and perspectives.” *Desalination* 356 (2015): 56-84.

Drioli, E., A. Criscuoli, and L.P. Molero. *Membrane Distillation.* EOLSS Encycl., 2000.

El-Bourawi, M. S., Z. Ding, R. Ma and M. Khayet. “A framework for better understanding membrane distillation separation process.” *Journal of Membrane Science* 285 (2006): 4-29.

Essalhi, M., and M. Khayet. “Fabrication and characterization of electro-spun nano-fibrous membranes for desalination by membrane distillation.” London: Euromembrane Conference 2012. 235-237.

Essalhi, M., and M. Khayet. “Self-sustained webs of polyvinylidene fluoride electrospun nanofibers at different electrospinning times: 1. Desalination by direct contact membrane distillation.” *Journal of Membrane Science* 433 (2013): 167-179.

Essalhi, M., and M. Khayet. “Self-sustained webs of polyvinylidene fluoride electrospun nanofibers at different electrospinning times: 2. Theoretical analysis, polarization effects and thermal efficiency.” *Journal of Membrane Science* 433 (2013): 180-191.

Essalhi, M., and M. Khayet. “Self-sustained webs of polyvinylidene fluoride electrospun nano-fibers: Effects of polymer concentration and desalination by direct contact membrane distillation.” *Journal of Membrane Science* 454 (2014): 133-143.

Etoumi, A. *Hybrid membrane-distillation separation for ethylene cracking*. D.Phil. thesis. Manchester: University of Manchester, 2014.

Fakheri, A. “Efficiency analysis of heat exchangers and heat exchanger networks.” *International Journal of Heat and Mass Transfer*, 2014: 99-104.

Fernández-Pineda, C., M. A. Izquierdo-Gil, and M. C. García-Payo . “Gas permeation and direct contact membrane distillation experiments and their analysis using different models.” *Journal of Membrane Science* 198 (2002): 33-49.

Field, R. W. “A theoretical viscosity correction factor for heat transfer and friction in pipe flow.” *Chemical Engineering Science* 45, no. 5 (1990): 1343-1347.

Field, R. W., H. Y. Wu, and J. J. Wu. “Multiscale modeling of membrane distillation: some theoretical considersations.” *Industrial & Engineering Chemistry Research* 52, no. 26 (2013): 8822-8828.

Förch, R., H. Schönherr, and A. T. A. Jenkins. *Surface design: applications in bioscience and nanotechnology* . John Wiley & Sons, 2009.

García-Rodríguez, L. “Renewable energy applications in desalination: state of the art.” *Solar Energy* 75 (2003): 381-393.

Ghaffour, N., J. Bundschuh, H. Mahmoudi, and M. F. A. Goosen. “Renewable energy-driven desalination technologies: A comprehensive review on challenges and potential applications of integrated systems.” *Desalination* 356 (2015): 94-114.

Goosen, M. F. A., S. S. Sablani, W. H. Shayya, C. Paton, and H. Al-Hinai. “Thermodynamic and economic considerations in solar desalination.” *Desalination* 129, no. 1 (2000): 63-89.

Gostoli, C., G. C. Sarti, and S. Matulli. “Low temperature distillation through hydrophobic membranes.” *Seperation science and Technology* 22 (1987): 855.

Govindan, P. N. *Thermal design of humidification dehumidification systems for affordable and small-scale desalination (PhD Thesis).* Massachusetts Institute of Technology , 2012.

Gröhn, H. G. “Influence of the yaw angle on heat transfer and pressure drop of tube bundle heat exchangers.” *Heat Transfer* 6 (1982): 203-209.

Gryta, M. “Effectiveness of water desalination by membrane .” *membranes* 2 (2012): 415-429.

Guan, G., X. Yang, R. Wang, R. Field, and A. G. Fane. “Evaluation of hollow fiber-based direct contact and vacuum membrane distillation systems using aspen process simulation.” *Journal of Membrane Science* 464 (2014): 127-139.

He, F., J. Gilron, and K. K. Sirkar. “High water recovery in direct contact membrane distillation using a series of cascades.” *Desalination* 323 (2013): 48-54.

Hitsov, I., T. Maere, K. De Sitter, C. Dortremont, and I. Nopens. “Modelling approaches in membrane distillation: A critical review.” *Separation and Purification Technology* 142 (2015): 48-64.

Hogan, P. A., Sudjito, A. G. Fane, and G. L. Morrison. “Desalination by solar heated membrane distillation.” *Desalination* 81, no. 1-3 (1991): 81-90.

Howatson, A. M., P. G. Lund, and J. D. Todd. *Engineering tables and data.* Oxford: Oxford Engineering Department, 1973.

IDA. *IDA.* 2014. http://idadesal.org/desalination-101/desalination-by-the-numbers/ (accessed 04 10, 2015).

Imdakm, A. O., and T. Matsuura. “A Monte Carlo simulation model for membrane distillation processes: direct contact (MD).” *Journal of Membrane Science* 237, no. 1-2 (2004): 51-59.

Imdakm, A. O., and T. Matsuura. “Simulation of heat and mass transfer in direct contact membrane distillation (MD): The effect of membrane physical properties.” *Journal of Membrane Science* 262, no. 1-2 (2005): 117-128.

Izquierdo-Gila, M. A., C. Fernández-Pinedaa, and M. G. Lornez. “Flow rate influence on direct contact membrane distillation experiments: Different empirical correlations for Nusselt number.” *Journal of Membrane Science* 321, no. 2 (2008): 356-363.

Jensen, M. B., K. V. Christensen, R. Andrésen , L. F. Søtoft , and B. Norddahl. “A model of direct contact membrane distillation for black currant juice.” *Journal of Food Engineering* 107, no. 3-4 (2011): 405-414.

Kalogirou, S. A. “Seawater desalination using renewable energy sources.” *Progress in Energy and Combustion Science* 31, no. 3 (2005): 242-281.

Karagiannis, I. C., and P. G. Soldatos. “Water desalination cost literature: review and assessment.” *Desalination* 223 (2008): 448-456.

Kays, W. M., and A. L. London. *Compact Heat Exchangers.* New York: McGraw-Hill, 1984.

Khayet, M. “Membranes and theoretical modelling of membrane distillation: A review.” *Advances in Colloid and Interface Science* 164, no. 1-2 (2011): 56-88.

Khayet, M. “Solar desalination by membrane distillation: Dispersion in energy consumption and water production costs (a review).” *Desalination* 308 (2013): 89-101.

Khayet, M., A. Velázquez, and J. I. Mengual. “Modelling mass transport through a porous partition: Effect of pore size distribution.” *Journal of Non-Equilibrium Thermodynamics* 29, no. 3 (2004): 279-299.

Khayet, M., A. O. Imdakm, and T. Matsuura. “Monte Carlo simulation and experimental heat and mass transfer in direct contact membrane distillation.” *International Journal of Heat and Mass Transfer* 53, no. 7-8 (2010): 1249-1259.

Khayet, M., and T. Matsuura. *Membrane Distillation: Principles and Applications.* Elsevier, 2011.

Khayet, M., M. P. Godino, and J. I. Mengual. “Modelling Transport Mechanism Through A Porous Partition.” *Journal of Non-Equilibrium Thermodynamics* 26, no. 1 (2001): 1-14.

Ki , S. J., H.-J. Kim, and A. S. Kim. “Big data analysis of hollow fiber direct contact membrane distillation (HFDCMD) for simulation-based empirical analysis.” *Desalination* 355 (2015): 56-67.

Kim, A. S. “Cylindrical cell model for direct contact membrane distillation (DCMD) of densely packed hollow fibers.” *Journal of Membrane Science* 455 (2014): 168-186.

Kim, Y.-D., K. Thu, N. Ghaffour, and K. C. Ng. “Performance investigation of a solar-assisted direct contact membrane distillation system.” *Journal of Membrane Science* 427 (2013): 345-364.

Kitic, D., D. C. Jardim, G. J. Favetto, S. L. Resnik, and J. Chirife. “Theoretical prediction of the water activity of standard saturated salt solutions at various temperatures.” *Journal of Food Science* 51, no. 4 (1986): 1037-1041.

Kohav, T. E., and S. Moshe. “Steady-state diffusion and reactions in catalytic fractal porous media.” *Chemical Engineering Science* 46, no. 11 (1991): 2787-2798.

Koschikowski, J., M. Wieghaus, and M. Rommel. “Solar thermal-driven desalination plants based on membrane distillation.” *Desalination* 156 (2003): 295-304.

Laganà, F., G. Barbieri, and E. Drioli. “Direct contact membrane distillation: modelling and concentration experiments.” *Journal of Membrane Science* 166 (2000): 1-11.

Lawson, K. W., and D. R. Lloryd. “Membrane distillation.” *Journal of Membrane Science* 124, no. 1 (1997): 1-25.

Lawson, K. W., and D. R. Lloyd. “Membrane distillation. II. Direct contact MD.” *Journal of Membrane Science* 120, no. 1 (1996): 123-133.

Lee, J.-G., and W.-S. Kim. “Numerical study on multi-stage vacuum membrane distillation with economic evaluation.” *Desalination* 339 (2014): 54-67.

Lévêque, J. A. “Les lois de la tranmission de chaleur par convection.” *Ann. Mines* 13 (1928): 201, 305, 381.

Liao, Y. *Design and fabrication of syperhydrophobic membranes by electrospinning for direct contact membrane distillation.* Singapore: PhD Thesis, School of civil and environmental engineering, Nanyang Technological University, 2014.

Liao, Y., R. Wang, and A. G. Fane. “Engineering superhydrophobic surface on poly(vinylidene fluoride) nanofiber membranes for direct contact membrane distillation.” *Journal of Membrane Science* 440 (2013): 77-87.

Liao, Y., R. Wang, M. Tian, C. Qiu, and A. G. Fane. “Fabrication of polyvinylidene fluoride (PVDF) nanofiber membranes by electro-spinning for direct contact membrane distillation.” *Journ. Mem. Sci.* 425-426 (2013): 30-39.

Liu, J. *Predicting the products of crude oil distillation columns.* M. Phil. thesis. Manchester: University of Manchester, 2012.

Macedonio, A. A., E. Drioli, S. Aljlil, and O. A. Alharbi. “Experimental and theoretical evaluation of temperature polarization phenomenon in direct contact membrane distillation.” *Chemical Engineering Research and Design* 91, no. 10 (2013): 1966-1977.

Mahmoud , S., M. Worall, and R. Saffa . “Opportunities for solar water desalination worldwide: Review.” *Sustainable Cities and Society* 9 (2013): 67-80.

Manawi, Y. M., M. A. M. M. Khraisheh, A. K. Fard, F. Benyahia, and S. Adham. “A predictive model for the assessment of the temperature polarization effect in direct contact membrane distillation desalination of high salinity feed.” *Desalination* 341 (2014): 38-49.

Martínez-Díez, L., and M. I. Vázquez-González . “Temperature and concentration polarization in membrane distillation of aqueous salt solutions.” *Journal of Membrane Science* 156, no. 2 (1999): 265-273.

Mason, E. A., and A. P. Malinauskas. *Gas transport in porous media: The Dusty-Gas Model.* Elsevier Science Ltd, 1983.

Mathew, B., and H. Hegab. “Application of effectiveness-NTU relationship to parallel flow microchannel heat exchangers subjected to external heat transfer.” *Internation Journal of Thermal Sciences* 49, no. 1 (2010): 76-85.

Mathioulakis, E., V. Belessiotis, and E. Delyannis. “Desalination by using alternative energy: Review and state-of-the-art.” *Desalination* 203, no. 1-3 (2007): 346-365.

Mericq, J. P., S. Laborie, and C. Cabassud. “Vacuum membrane distillation for an integrated seawater desalination process.” *Desalination and Water Treatment* (Desalination and Water Treatment) 9 (2009): 287-296.

“Microdyn Nadir Produce Catalogue.” n.d. http://www.microdyn-nadir.com/en/Products/MICRODYN/ (accessed March 25, 2015).

Mills, A. F. *Mass transfer, 2nd Edition.* New Jersey: Prestice-Hall, 2001.

Mokheimer, E. M. A., A. Z. Sahin, A. Al-sharafi, and A. I. Ali. “Modeling and optimization of hybrid wind–solar-powered reverse osmosis water desalination system in Saudi Arabia.” *Energy Conversion and Management* 75 (2013): 86-97.

Morillo, J., J. Usero, D. Rosado, H. El Bakouri, A. Riaza, and F.-J. Bernaola. “Comparative study of brine management technologies for desalination plants.” *Desalination* 336 (2014): 32-49.

Mulvaney, D., and P. Robbins. *Green technology.* California: SAGE Publications, 2011.

Newton, Isaac. *Letter to Robert Hooke.* 1676.

Pantoja, C. E., Y. N. Nariyoshi, and M. M. Seckler. “Membrane Distillation Crystallization Applied to Brine Desalination: A Hierarchical Design Procedure.” *Ind. Eng. Chem. Res.* 54, no. 10 (2015): 2776-2793.

Pearce, G. K. *UF/MF Mebrane Water Treatment: Principles and Design.* Water Treatment Academy, 2012.

Phattaranawik, J. , R. Jiraratananon, and A. G. Fane. "Effect of pore size distribution and air flux on mass transport in direct contact membrane distillation." *Journal of Membrane Science* 215 (2003): 75.

Qtaishat, M. R., and F. Banat. "Desalination by solar powered membrane distillation systems." *Desalination* 308 (2013): 186-197.

Qtaishat, M., M. Khayet, and T. Matsuura. "Guidelines for preparation of higher flux hydrophobic/hydrophilic composite membranes for membrane distillation." *Journal of Membrane Science* 329, no. 1-2 (2009): 193-200.

Rathore, M. M., and R. R. A. Kapuno, Jr. *Engineering heat transfer, 2nd edition.* Jones and Bartlett Publishers, 2009.

Ren, C. Q., M. Tu, and H. H. Wang. "An analytical model for heat and mass transfer processes in internally cooled or heated liquid desiccant-air contact units." *International Journal of Heat and Mass Transfer* 50 (2007): 3545-3555.

Royal Embassay of Saudi Arabia. *Royal Embassay of Saudi Arabia.* 2015. http://www.saudiembassy.net/about/country-information/agriculture_water/Water_Resources.aspx (accessed Apr 30, 2015).

Sadhukhan, H. K., and P. K. Tewari. "Small Desalination Plants (SDPs)." In *Thermal desalination processes, vol. II.* Encyclopedia of Desalination and Water Resources (DESWARE), n.d.

Saffarini, R. B., E. K. Summers, H. A. Aradat, and J. H. Lienhard V. “Economic evaluation of stand-alone solar powered membrane distillation systems.” *Desalination* 299 (2012): 55-62.

Sánchez, A. S., I. B. R. Nogueira, and R. A. Kalid. “Uses of the reject brine from inland desalination for fish farming, Spirulina cultivation, and irrigation of forage shrub and crops.” *Desalination* 364 (2015): 96-107.

Schofield, R. W., A. G. Fane, and C. J. D. Fell. “Gas and vapour transport through microporous membranes. I. Knudsen-Poiseuille transition.” *Journal of Membrane Science* 53, no. 1-2 (1990): 159-171.

Schofield, R. W., A. G. Fane, and C. J. D. Fell. “Gas and vapour transport through microporous membranes. II. Membrane distillation.” *Journal of Membrane Science* 53 (1990): 173-185.

Schofield, R. W., A. G. Fane, and C. J. D. Fell. “Heat and mass transfer in membrane distillation.” *Journal of Membrane Science* 33 (1987): 299-313.

ScienceDirect. 2015. http://www.sciencedirect.com/science?_ob=ArticleListURL&_method=list&_ArticleListID=-776033578&_sort=r&_st=13&view=c&md5=96eababcb28b7838c9bcd80d2bfd929a&searchtype=a (accessed 4 21, 2015).

Selvi, S. R., and R. Baskaran. “Desalination of well water by solar power membrane distillation and reverse osmosis and its efficiency analysis.” *International Journal of ChemTech Research* 6, no. 5 (2014): 2628-2636.

Serth, R. W., and T. G. Lestina. *Process Heat Transfer (Second Edition) Principles, Applications and Rules of Thumb.* Oxford: Elsevier Inc., 2014.

Sharqawy, M. H., L. D. Banchik, and J. H. Lienhard V. "Effectiveness–mass transfer units (ε–MTU) model of an ideal pressure retarded osmosis membrane mass exchange." *Journal of Membrane Science* 445 (2013): 211-219.

Shenzhen Youber Technology Co., Ltd. *Alibaba.* n.d. http://www.alibaba.com/product-detail/Reverse-osmosis-desalinator-for-drinking-water_1748971885.html (accessed 5 25, 2015).

Singh, D., and K. K. Sirkar. "High temperature direct contact membrane distillation based desalination using PTFE hollow fibers." *Chemical Engineering Science* 116 (2014): 824-833.

Song, L., B. Li, K. K. Sirkar, and J. L. Gilron. "Direct Contact Membrane Distillation-Based Desalination: Novel Membranes, Devices, Larger-Scale Studies, and a Model." *Ind. Eng. Chem. Res.* 46, no. 8 (2007): 2307-2323.

Song, L., Z. Ma, X. Liao, P. B. Kosaraju, J. R. Irish, and K. K. Sirkar. "Pilot plant studies of novel membranes and devices for direct contact membrane distillation-based desalination." *Journal of Membrane Science* 323, no. 2 (2008): 257-270.

Sparrow, E. M., and A. L. Loeffler JR. "Longitudinal laminar flow between cyliners arranged in regular array." *AIChE Journal*, 1959.

Sugiyama, K. , Y. Ukita, and Y. Takamura. "Development of on-chip vacuum generation by gas–liquid phase transition." *Sensors and Actuators A: Physical* 176 (2012): 138-142.

Sultan, H. *History, development and management of water resources.* Vol. II. DESWARE, 2010.

—. *History, development and management of water resources.* Vol. II. DESWARE, n.d.

Summers, E. K. *Development of energy efficiency membrane distillation systems, PhD Thesis.* Cambridge: MIT, 2013.

Suri, R. K., A. M. R. Al-Marafie, A. A. Al-Homoud, and G. P. Maheshwari. “Cost-effectiveness of solar water production.” *Desalination* 71, no. 2 (1989): 165-175.

Susanto, H. “Towards practical implementations of membrane distillation.” *Chemical Engineering and Processing:* 50 (2011): 139-150.

Tabor, D. *Gases, liquids and solids and other states of matter, 3rd edition.* Cambridge: Cambridge University Press, 1991.

Takagi, M., Karseno, and T. Yoshida. “Effect of salt concentration on intracellular accumulation of lipids and triacylglyceride in marine microalgae Dunaliella cells.” *Journal of Bioscience and Bioengineering* 101, no. 3 (2006): 223-226.

Tan, J. O., and C. Y. Liu. “Predicting the performance of a heat-pipe heat exchanger, using the effectiveness- NTUmethod.” *International Journal of Heat and Fluid Flow* 11, no. 4 (1990): 376-379.

Tomaszewska, M. “Membrane distillation - Examples of applications in technology and environmental protection.” *Polish Journal of Environmental Studies* 9, no. 1 (2000): 27-36.

Turel, T. *Gas transmission through microporous membranes.* ProQuest, 2008.

Tzen, E., G. Zaragoza, and D. C. Alarcón Padilla. *3.16 - Solar Desalination.* Vol. 3, in *Reference Module in Earth Systems and Environmental Sciences, from Comprehensive Renewable Energy*, 529-565. 2012.

UN. *The human right to water and sanitation.* Zaragoza: UN-Water Decade Programme on Advocacy and Communication and Water Supply and Sanitation Collaborative Council, 2014.

Wang, L. K., J. P. Chen, Y.-T. Hung, and N. K. Shammas. *Membrane and Desalination Technologies.* Humana Press, 2010.

Wang, P., and T.-S. Chung. "Recent advances in membrane distillation processes: Membrane." *Journal of Membrane Science,* 474 (2015): 39-56.

Wang, Y., F. Chen, Y. Wang, G. Luo, and Y. Dai. "Effect of random packing on shell-side flow and mass transfer in hollow fiber module described by normal distribution function." *Journal of Membrane Science* 216 (2003): 81-93.

WHO/UNICEF, Joint Monitoring Programme. "Progress on sanitation and drinking-water, 2014 update." 2014.

WHO/UNICEF, WHO/UNICEF Joint Monitoring Programme. "Meeting the MDG drinking water and sanitation target: The urban and rural challenge of the decade." 2006.

Wu, H. Y., J. Hu, and R. Field. "Membranes for drinking water production: The role of membrane processes in localised small scale desalination systems coupled directly with solar energy." *Euromembrane 2012.* London, 2012.

Wu, J., and V. Chen. "Shell-side mass transfer performance of randomly packed hollow fiber modules." *Journal of Membrane Science* 172 (2000): 59-74.

Xu, X., J. Liu, and L. Cao. “Optimization and analysis of mixed refrigerant composition for the PRICO natural gas liquefaction process.” *Cryogenics* 59 (2014): 60-69.

Yang, X., H. Yu, R. Wang, and A. G. Fane. “Analysis of the effect of turbulence promoters in hollow fiber membrane distillation modules by computational fluid dynamic (CFD) simulations.” *Journal of Membrane Science* 415-416 (2012): 758-769.

Yang, X., H. Yu, R. Wang, and A. G. Fane. “Optimization of microstructured hollow fiber design for membrane distillation applications using CFD modeling.” *Journal of Membrane Science,* 2012: 421-422.

Yu, H., X. Yang, R. Wang, and A. G. Fane. “Analysis of heat and mass transfer by CFD for performance enhancement in direct contact membrane distillation.” *Journal of Membrane Science* 405-406 (2012): 38-47.

Yun, Y., R. Ma, W. Zhang, A. G. Fane, and J. Li. “Direct contact membrane distillation mechanism for high concentration NaCl solutions.” *Desalination* 188, no. 1-3 (2006): 251-262.

Zaragoza, G., A. Ruiz-Aguirre, and E. Guillén-Burrieza. “Efficiency in the use of solar thermal energy of small membrane.” *Applied Energy* 130 (2014): 491-499.

Zhang, L-Z.. “Heat and mass transfer in a quasi-counter flow membrane-based total heat exchanger.” *Internation Journal of Heat and Mass Transfer* 53, no. 23-24 (2010): 5478-5486.

Zhu, C., and G. Liu. “Modeling of ultrasonic enhancement on membrane distillation.” *Journal of Membrane Science* 176, no. 1 (2000): 31-41.

Zhuang, J., N. Dow, M. Duke, E. Ostarcevic, J.-D. Li, and S. Gray. "Identification of material and physical features of membrane distillation." n.d. http://core.kmi.open.ac.uk/download/pdf/10834414.pdf (accessed January 21, 2015).

Zisman, W.A. *Contact Angle, Wettability, and Adhesion.* Edited by F.M. Fowkes. Vol. 43. AMERICAN CHEMICAL SOCIETY, 1964.

Zuo, G., R. Wang, R. Field, and A. G. Fane. "Energy efficiency evaluation and economic analyses of direct contact membrane distillation system using Aspen Plus." *Desalination* 283 (2011): 237-244.

Appendix A: Heatpress machine

A picture of the custom-ordered heatproof machine that is identical to the one used for the heat treatment in Chapter 3

Appendix B: Customized Aspen Model – Method 1

This appendix describes a way to incorporate MATLAB model to Aspen Plus flowsheet directly, using a interface created by Microsoft Excel. Apart from the interface between MATLAB and Microsoft Excel Workbook, the customised Aspen DCMD-HFM module is constructed based on the instructions given in the menu provided by Aspentech (Apsentech; 2012). Parts of the model, including the Aspen Plus to Excel interface, were adopted from (with modifications to suit our DCMD model and process) support files (computer files that come with the teaching license) provided by Aspentech, which is also described in the menu. The key features of the customized DCMD Aspen model, including (i) User array data; (ii) Setting up the Microsoft Excel Workbook; and (iii) MATLAB interface, are documented below.

(i) User array data in Aspen Plus

The user array data, shown in Figure B-1, is where the design variables and parameters of the model are specified. For our model, the number of fibres,module length, packing density and the fibre size are defined and pass into the MATLAB model.

Figure B-8 User array data the customized DCMD-HMF

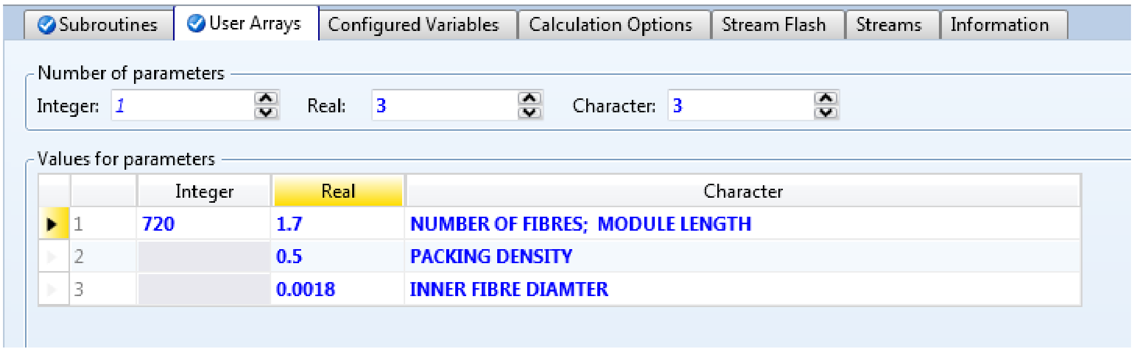

Number of parameters

Integer: 1 Real: 3 Character: 3

Values for parameters

	Integer	Real	Character
1	720	1.7	NUMBER OF FIBRES; MODULE LENGTH
2		0.5	PACKING DENSITY
3		0.0018	INNER FIBRE DIAMTER

(ii) Setting up the Microsoft Excel Workbook

The Aspen Plus and Microsoft Excel Workbook interface, built using Microsoft Marcros, is documented in the following 2 pages. The backbone of the code is adopted from the supporting file provided by Aspentech in which the green lines are the comments and the rests are the commands.

```
'Global to hold the current block id.  Set in AspenStartIteration, and
'cleared in AspenEndIteration.
Dim g blockId As String
Public Function AspenCalculate() As String
'Called to solve the model for the given inputs.  Called after writing out all of the input data.
'By default we just call Calculate.  If you are writing VBA code to solve your model call it from here.

AspenCalculate = ""

'AspenCalculate = "This is an error in calc"
End Function
Public Function AspenStartIteration(blockId As String) As String
'Called at the start of each iteration of the model, before the model
'gets calculated.
g_blockId = blockId
AspenStartIteration = ""
End Function
Public Function AspenEndIteration() As String
'Called at the end of each iteration of the model, after the model has been calculated.

'If you want to save the last table of data to a uniquely named sheet, this would be the place to do it
'The following line will create a sheet called Aspen_Output_B2, if the block id is B2, and copy all of
'the data currently held in the Aspen_Output sheet.
CopySheetForBlock "Output", g_blockId
AspenEndIteration = ""
End Function
Public Function AspenEndRun(runid As String)
'Called when the Aspen Plus engine is quitting, after all blocks have been processed.  The runid is
'passed from the engine.  You may want to use the runid as part of the filename if saving the sheet at
'end of a run.

'To save at the end of a run comment out the following
ThisWorkbook.Save
AspenEndRun = ""
End Function

Private Function GetSheet(sheetName As String) As Worksheet
'Create the sheet if it is not already there.
On Error Resume Next
Set GetSheet = Nothing
Set GetSheet = Worksheets(sheetName)
If Err = 9 Then 'subscript out of range
    Err.Clear
    On Error GoTo 0
    Set GetSheet = Worksheets.Add
    GetSheet.Name = sheetName
End If
End Function

Private Sub CopySheetForBlock(sheetNameToCopy As String, blockName As String)
Dim sheetNameForBlock As String
Dim sheetToCopy As Worksheet
Dim sheetForBlock As Worksheet

Set sheetToCopy = Worksheets("Aspen_" & sheetNameToCopy)
sheetNameForBlock = "Aspen_" & sheetNameToCopy & "_" & blockName
Set sheetForBlock = GetSheet(sheetNameForBlock)
sheetToCopy.UsedRange.Copy
sheetForBlock.Range("A1").PasteSpecial Paste:=xlPasteValues
End Sub
Public Function ahtest() As Integer
Dim testSheet As Worksheet

Set testSheet = GetSheet("Aspen_TestMacros")
testSheet.Cells.Clear

' Write out all the counts
testSheet.Cells(1, 1).Value = "Number of Input Streams:"
testSheet.Cells(1, 2).Value = ahNumStreams([aspen_input])

testSheet.Cells(2, 1).Value = "Number of Ouput Streams:"
testSheet.Cells(2, 2).Value = ahNumStreams([Aspen_Output])

testSheet.Cells(3, 1).Value = "Number of Components:"
testSheet.Cells(3, 2).Value = ahNumComps([aspen_input])

testSheet.Cells(4, 1).Value = "Number of Integer Parameters:"
testSheet.Cells(4, 2).Value = ahNumParams([Aspen_IntParams])

testSheet.Cells(5, 1).Value = "Number of Real Parameters:"
testSheet.Cells(5, 2).Value = ahNumParams([Aspen RealParams])
```

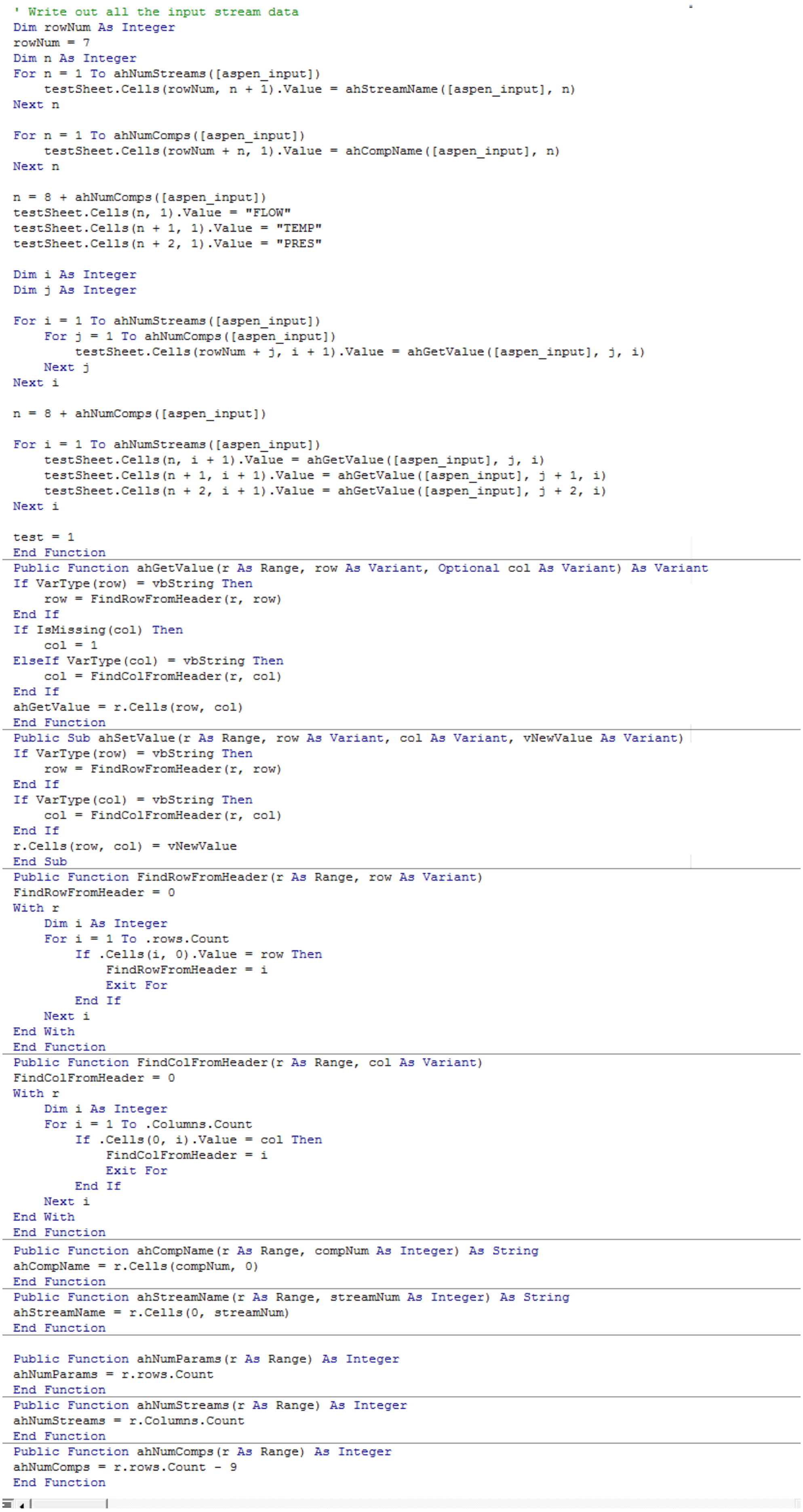

```
' Write out all the input stream data
Dim rowNum As Integer
rowNum = 7
Dim n As Integer
For n = 1 To ahNumStreams([aspen_input])
    testSheet.Cells(rowNum, n + 1).Value = ahStreamName([aspen_input], n)
Next n

For n = 1 To ahNumComps([aspen_input])
    testSheet.Cells(rowNum + n, 1).Value = ahCompName([aspen_input], n)
Next n

n = 8 + ahNumComps([aspen_input])
testSheet.Cells(n, 1).Value = "FLOW"
testSheet.Cells(n + 1, 1).Value = "TEMP"
testSheet.Cells(n + 2, 1).Value = "PRES"

Dim i As Integer
Dim j As Integer

For i = 1 To ahNumStreams([aspen_input])
    For j = 1 To ahNumComps([aspen_input])
        testSheet.Cells(rowNum + j, i + 1).Value = ahGetValue([aspen_input], j, i)
    Next j
Next i

n = 8 + ahNumComps([aspen_input])

For i = 1 To ahNumStreams([aspen_input])
    testSheet.Cells(n, i + 1).Value = ahGetValue([aspen_input], j, i)
    testSheet.Cells(n + 1, i + 1).Value = ahGetValue([aspen_input], j + 1, i)
    testSheet.Cells(n + 2, i + 1).Value = ahGetValue([aspen_input], j + 2, i)
Next i

test = 1
End Function
Public Function ahGetValue(r As Range, row As Variant, Optional col As Variant) As Variant
If VarType(row) = vbString Then
    row = FindRowFromHeader(r, row)
End If
If IsMissing(col) Then
    col = 1
ElseIf VarType(col) = vbString Then
    col = FindColFromHeader(r, col)
End If
ahGetValue = r.Cells(row, col)
End Function
Public Sub ahSetValue(r As Range, row As Variant, col As Variant, vNewValue As Variant)
If VarType(row) = vbString Then
    row = FindRowFromHeader(r, row)
End If
If VarType(col) = vbString Then
    col = FindColFromHeader(r, col)
End If
r.Cells(row, col) = vNewValue
End Sub
Public Function FindRowFromHeader(r As Range, row As Variant)
FindRowFromHeader = 0
With r
    Dim i As Integer
    For i = 1 To .rows.Count
        If .Cells(i, 0).Value = row Then
            FindRowFromHeader = i
            Exit For
        End If
    Next i
End With
End Function
Public Function FindColFromHeader(r As Range, col As Variant)
FindColFromHeader = 0
With r
    Dim i As Integer
    For i = 1 To .Columns.Count
        If .Cells(0, i).Value = col Then
            FindColFromHeader = i
            Exit For
        End If
    Next i
End With
End Function
Public Function ahCompName(r As Range, compNum As Integer) As String
ahCompName = r.Cells(compNum, 0)
End Function
Public Function ahStreamName(r As Range, streamNum As Integer) As String
ahStreamName = r.Cells(0, streamNum)
End Function

Public Function ahNumParams(r As Range) As Integer
ahNumParams = r.rows.Count
End Function
Public Function ahNumStreams(r As Range) As Integer
ahNumStreams = r.Columns.Count
End Function
Public Function ahNumComps(r As Range) As Integer
ahNumComps = r.rows.Count - 9
End Function
```

Inside the Excel Workbook, there are four customized worksheets: one contains integer parameters defined and passed on by Aspen (Figure B-9), one contains the real parameter (Figure B-10), one contains the operational conditions (Figure B-11) and the forth one stores the outputs (Figure B-12).

Figure B-9 Worksheet containing the integer parameters defined in Aspen

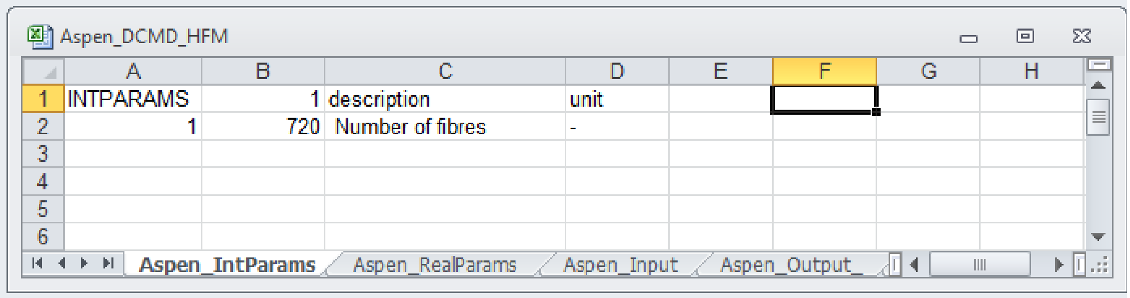

	A	B	C	D	E	F	G	H
1	INTPARAMS	1	description	unit				
2	1	720	Number of fibres	-				
3								
4								
5								
6								

Figure B-10 Worksheet containing the real parameters defined in Aspen

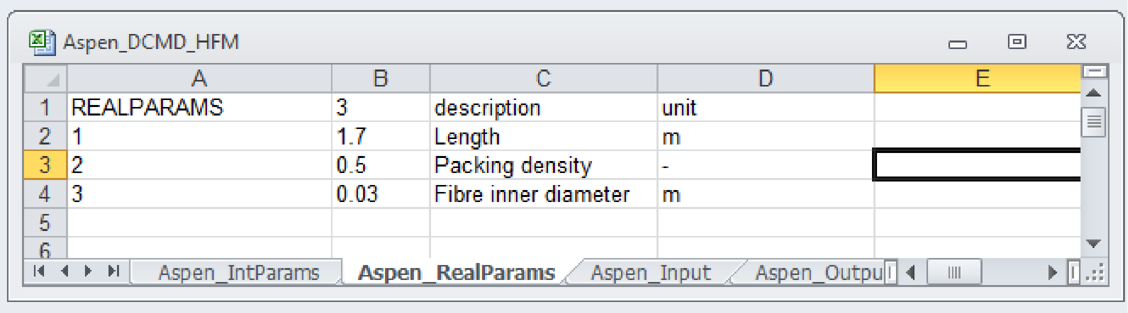

	A	B	C	D	E
1	REALPARAMS	3	description	unit	
2	1	1.7	Length	m	
3	2	0.5	Packing density	-	
4	3	0.03	Fibre inner diameter	m	
5					
6					

Figure B-11 Worksheet containing the operational conditions defined in Aspen

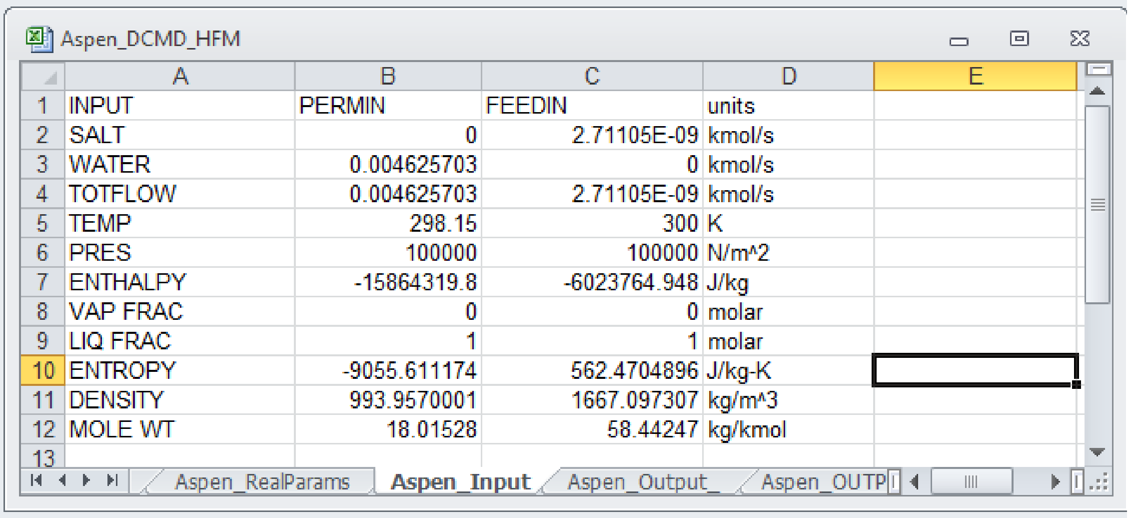

	A	B	C	D	E
1	INPUT	PERMIN	FEEDIN	units	
2	SALT	0	2.71105E-09	kmol/s	
3	WATER	0.004625703	0	kmol/s	
4	TOTFLOW	0.004625703	2.71105E-09	kmol/s	
5	TEMP	298.15	300	K	
6	PRES	100000	100000	N/m^2	
7	ENTHALPY	-15864319.8	-6023764.948	J/kg	
8	VAP FRAC	0	0	molar	
9	LIQ FRAC	1	1	molar	
10	ENTROPY	-9055.611174	562.4704896	J/kg-K	
11	DENSITY	993.9570001	1667.097307	kg/m^3	
12	MOLE WT	18.01528	58.44247	kg/kmol	
13					

Figure B-12 Worksheet for storing the outputs received from MATLAB model

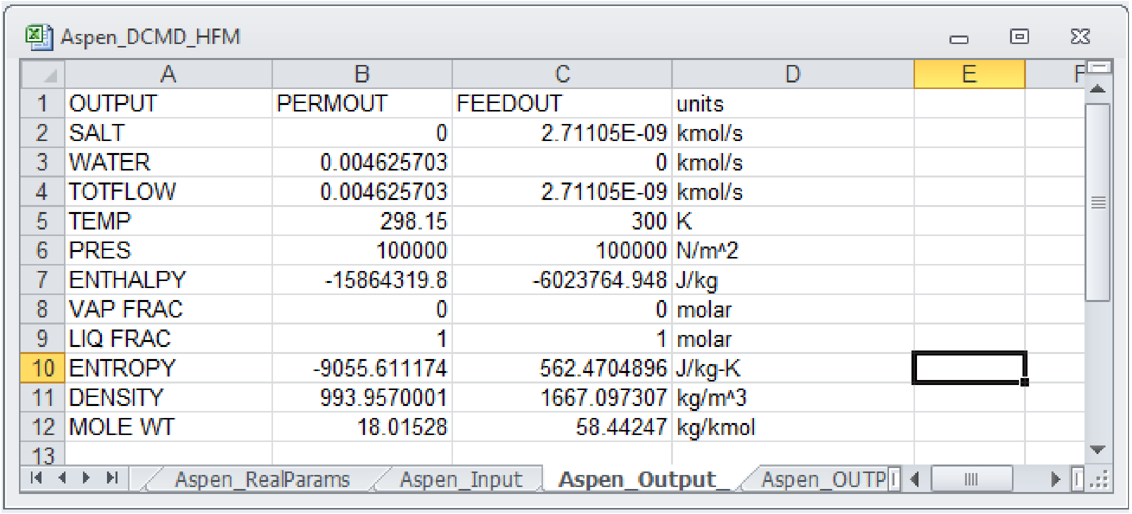

OUTPUT	PERMOUT	FEEDOUT	units
SALT	0	2.71105E-09	kmol/s
WATER	0.004625703	0	kmol/s
TOTFLOW	0.004625703	2.71105E-09	kmol/s
TEMP	298.15	300	K
PRES	100000	100000	N/m^2
ENTHALPY	-15864319.8	-6023764.948	J/kg
VAP FRAC	0	0	molar
LIQ FRAC	1	1	molar
ENTROPY	-9055.611174	562.4704896	J/kg-K
DENSITY	993.9570001	1667.097307	kg/m^3
MOLE WT	18.01528	58.44247	kg/kmol

(iii) Interface with MATLAB

The interface with MATLAB is established in both the Excel VBA Developer and in MATLAB. Upon being requested by Aspen Plus to initiate the DCMD-HFM simulation, Microsoft Excel passed on the request and initiates the MATLAB simulation according to the VBA codes shown in Figure B-13.

Figure B-13 Microsoft Excel – MATLAB interface; in Excel Code Module

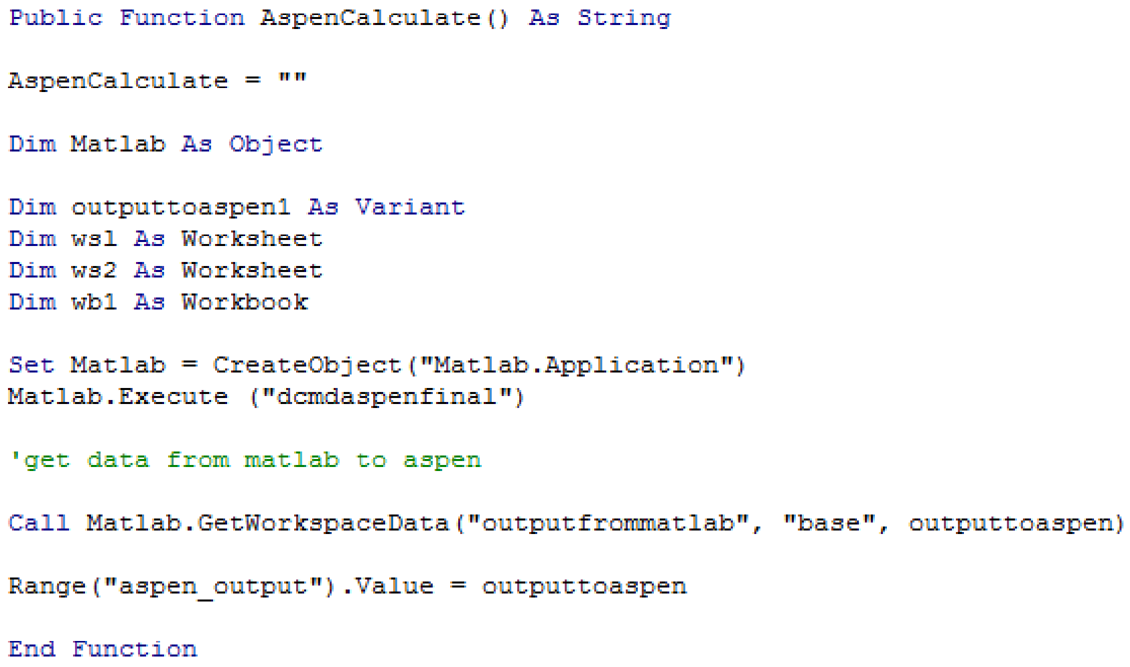

```
Public Function AspenCalculate() As String

AspenCalculate = ""

Dim Matlab As Object

Dim outputtoaspen1 As Variant
Dim ws1 As Worksheet
Dim ws2 As Worksheet
Dim wb1 As Workbook

Set Matlab = CreateObject("Matlab.Application")
Matlab.Execute ("dcmdaspenfinal")

'get data from matlab to aspen

Call Matlab.GetWorkspaceData("outputfrommatlab", "base", outputtoaspen)

Range("aspen_output").Value = outputtoaspen

End Function
```

The code in Figure B-13 initiates MATLAB to execute the file called “dcmdaspenfinal” which using MATLAB fuctions “xlsread” (shown in Figure B-14), MATLAB could import the variables and parameters defined in Aspen and stored in the corresponding worksheets. Once the simulation is completed, MATLAB would pass the simulated data to a computer storage place called ‘base’ where Excel could fetch the values available in ‘outputfrommatlab’.

Figure B-14 Microsoft Excel – MATLAB interface; in MATLAB

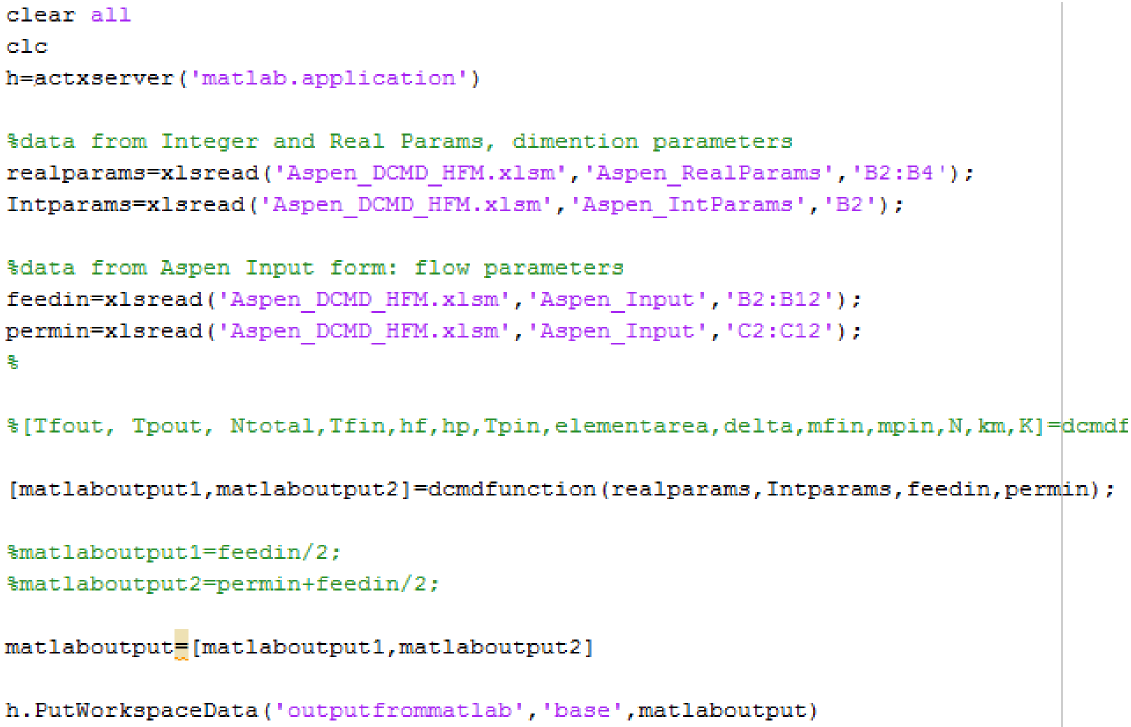

```
clear all
clc
h=actxserver('matlab.application')

%data from Integer and Real Params, dimention parameters
realparams=xlsread('Aspen_DCMD_HFM.xlsm','Aspen_RealParams','B2:B4');
Intparams=xlsread('Aspen_DCMD_HFM.xlsm','Aspen_IntParams','B2');

%data from Aspen Input form: flow parameters
feedin=xlsread('Aspen_DCMD_HFM.xlsm','Aspen_Input','B2:B12');
permin=xlsread('Aspen_DCMD_HFM.xlsm','Aspen_Input','C2:C12');
%

%[Tfout, Tpout, Ntotal,Tfin,hf,hp,Tpin,elementarea,delta,mfin,mpin,N,km,K]=dcmdf

[matlaboutput1,matlaboutput2]=dcmdfunction(realparams,Intparams,feedin,permin);

%matlaboutput1=feedin/2;
%matlaboutput2=permin+feedin/2;

matlaboutput=[matlaboutput1,matlaboutput2]

h.PutWorkspaceData('outputfrommatlab','base',matlaboutput)
```

Finally, the values are exported to Aspen_Output worksheet in Excel which is then passed onto Aspen.

Appendix C: Customized Aspen Model – Method 2

This appendix documents the Method2 described in Chapter 6 in the thesis, which a look-up table is created using results obtained from the MATLAB model.

The user array data and the interface between Aspen Plus and Microsoft Excel, described in Appendix B (i) and (ii) are identical in both Method 1 and Method 2. In addition to the four worksheets described in Appendix B(ii), an extra worksheet (labelled as MatLab_Result_bank in Figure) which store all the MATLAB pre-run data is established, as shown in Figure B-15.

Figure B-15 Worksheet used as look-up table, which contains all the pre-run result obtained from MATLAB simulations

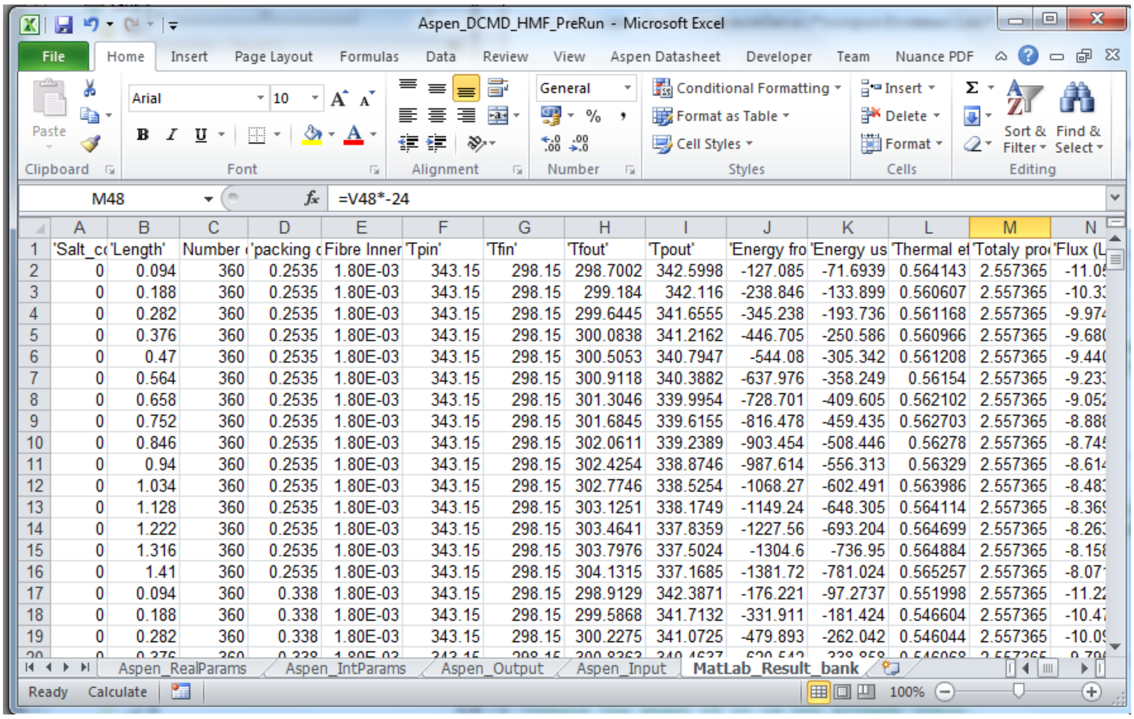

M48 =V48*-24

	A	B	C	D	E	F	G	H	I	J	K	L	M	N
1	'Salt_c	'Length'	Number	'packing	Fibre Inner	'Tpin'	'Tfin'	'Tfout'	'Tpout'	'Energy fro	'Energy us	'Thermal e	'Totaly pro	'Flux (L
2	0	0.094	360	0.2535	1.80E-03	343.15	298.15	298.7002	342.5998	-127.085	-71.6939	0.564143	2.557365	-11.0
3	0	0.188	360	0.2535	1.80E-03	343.15	298.15	299.184	342.116	-238.846	-133.899	0.560607	2.557365	-10.3
4	0	0.282	360	0.2535	1.80E-03	343.15	298.15	299.6445	341.6555	-345.238	-193.736	0.561168	2.557365	-9.97
5	0	0.376	360	0.2535	1.80E-03	343.15	298.15	300.0838	341.2162	-446.705	-250.586	0.560966	2.557365	-9.68
6	0	0.47	360	0.2535	1.80E-03	343.15	298.15	300.5053	340.7947	-544.08	-305.342	0.561208	2.557365	-9.44
7	0	0.564	360	0.2535	1.80E-03	343.15	298.15	300.9118	340.3882	-637.976	-358.249	0.56154	2.557365	-9.23
8	0	0.658	360	0.2535	1.80E-03	343.15	298.15	301.3046	339.9954	-728.701	-409.605	0.562102	2.557365	-9.05
9	0	0.752	360	0.2535	1.80E-03	343.15	298.15	301.6845	339.6155	-816.478	-459.435	0.562703	2.557365	-8.88
10	0	0.846	360	0.2535	1.80E-03	343.15	298.15	302.0611	339.2389	-903.454	-508.446	0.56278	2.557365	-8.74
11	0	0.94	360	0.2535	1.80E-03	343.15	298.15	302.4254	338.8746	-987.614	-556.313	0.56329	2.557365	-8.61
12	0	1.034	360	0.2535	1.80E-03	343.15	298.15	302.7746	338.5254	-1068.27	-602.491	0.563986	2.557365	-8.48
13	0	1.128	360	0.2535	1.80E-03	343.15	298.15	303.1251	338.1749	-1149.24	-648.305	0.564114	2.557365	-8.36
14	0	1.222	360	0.2535	1.80E-03	343.15	298.15	303.4641	337.8359	-1227.56	-693.204	0.564699	2.557365	-8.26
15	0	1.316	360	0.2535	1.80E-03	343.15	298.15	303.7976	337.5024	-1304.6	-736.95	0.564884	2.557365	-8.15
16	0	1.41	360	0.2535	1.80E-03	343.15	298.15	304.1315	337.1685	-1381.72	-781.024	0.565257	2.557365	-8.07
17	0	0.094	360	0.338	1.80E-03	343.15	298.15	298.9129	342.3871	-176.221	-97.2737	0.551998	2.557365	-11.2
18	0	0.188	360	0.338	1.80E-03	343.15	298.15	299.5868	341.7132	-331.911	-181.424	0.546604	2.557365	-10.4
19	0	0.282	360	0.338	1.80E-03	343.15	298.15	300.2275	341.0725	-479.893	-262.042	0.546044	2.557365	-10.0

While it is impossible to have pre-run result the exact input variables (input valuables between Aspen iterations is corrected to 4 d. p.); the minimum difference between each input parameters and their corresponding pre-run values are evaluated and matched, using the code shown in Figure B-16. Once the correct row is identified, Excel would transfer the output values reported in the row to Aspen_Output worksheet, which the results are then exported to Aspen.

Figure B-16 Worksheet used as look-up table, which contains all the pre-run result obtained from MATLAB simulations

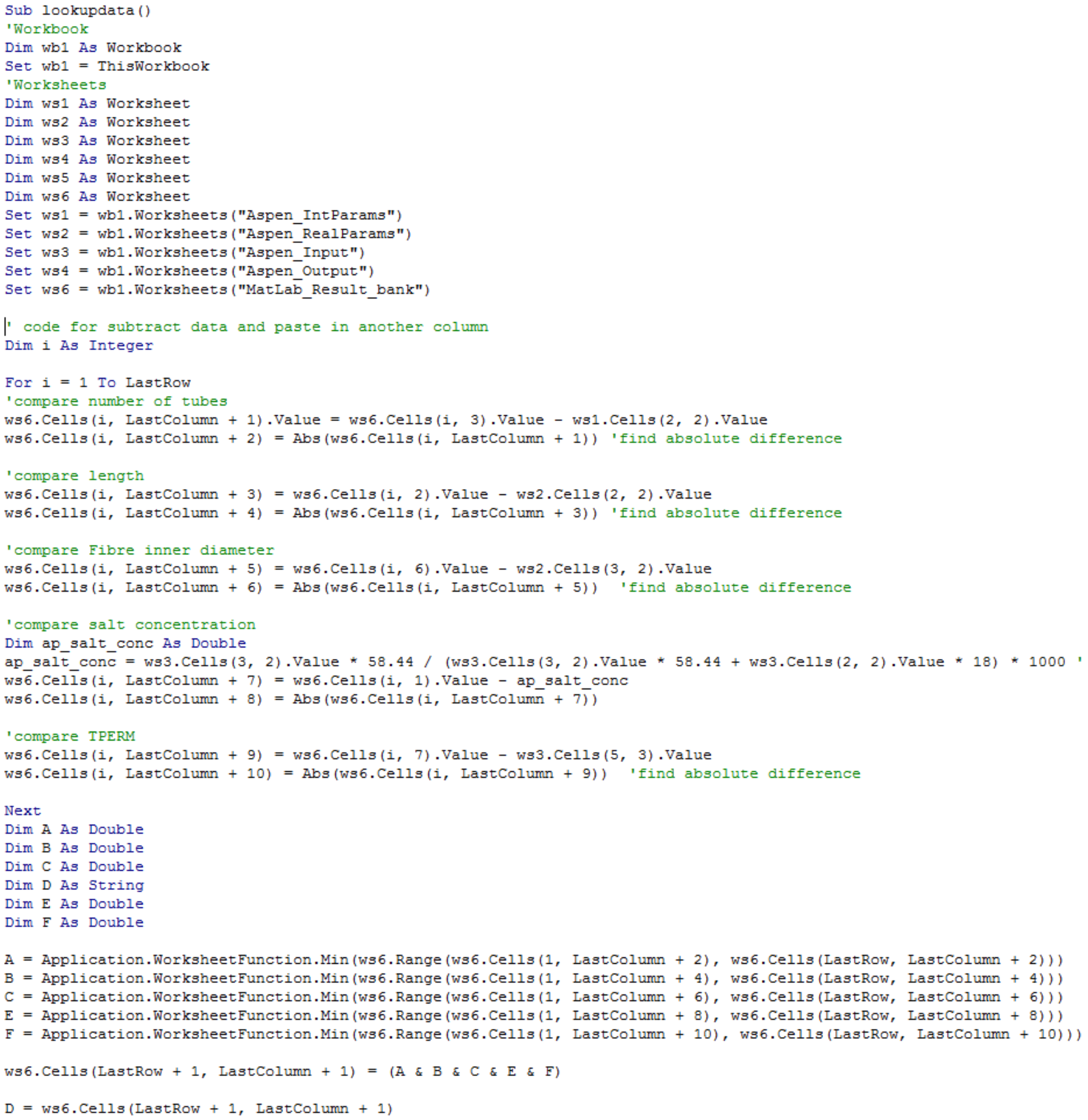

```
Sub lookupdata()
'Workbook
Dim wb1 As Workbook
Set wb1 = ThisWorkbook
'Worksheets
Dim ws1 As Worksheet
Dim ws2 As Worksheet
Dim ws3 As Worksheet
Dim ws4 As Worksheet
Dim ws5 As Worksheet
Dim ws6 As Worksheet
Set ws1 = wb1.Worksheets("Aspen_IntParams")
Set ws2 = wb1.Worksheets("Aspen_RealParams")
Set ws3 = wb1.Worksheets("Aspen_Input")
Set ws4 = wb1.Worksheets("Aspen_Output")
Set ws6 = wb1.Worksheets("MatLab_Result_bank")

' code for subtract data and paste in another column
Dim i As Integer

For i = 1 To LastRow
'compare number of tubes
ws6.Cells(i, LastColumn + 1).Value = ws6.Cells(i, 3).Value - ws1.Cells(2, 2).Value
ws6.Cells(i, LastColumn + 2) = Abs(ws6.Cells(i, LastColumn + 1)) 'find absolute difference

'compare length
ws6.Cells(i, LastColumn + 3) = ws6.Cells(i, 2).Value - ws2.Cells(2, 2).Value
ws6.Cells(i, LastColumn + 4) = Abs(ws6.Cells(i, LastColumn + 3)) 'find absolute difference

'compare Fibre inner diameter
ws6.Cells(i, LastColumn + 5) = ws6.Cells(i, 6).Value - ws2.Cells(3, 2).Value
ws6.Cells(i, LastColumn + 6) = Abs(ws6.Cells(i, LastColumn + 5))  'find absolute difference

'compare salt concentration
Dim ap_salt_conc As Double
ap_salt_conc = ws3.Cells(3, 2).Value * 58.44 / (ws3.Cells(3, 2).Value * 58.44 + ws3.Cells(2, 2).Value * 18) * 1000 '
ws6.Cells(i, LastColumn + 7) = ws6.Cells(i, 1).Value - ap_salt_conc
ws6.Cells(i, LastColumn + 8) = Abs(ws6.Cells(i, LastColumn + 7))

'compare TPERM
ws6.Cells(i, LastColumn + 9) = ws6.Cells(i, 7).Value - ws3.Cells(5, 3).Value
ws6.Cells(i, LastColumn + 10) = Abs(ws6.Cells(i, LastColumn + 9))  'find absolute difference

Next
Dim A As Double
Dim B As Double
Dim C As Double
Dim D As String
Dim E As Double
Dim F As Double

A = Application.WorksheetFunction.Min(ws6.Range(ws6.Cells(1, LastColumn + 2), ws6.Cells(LastRow, LastColumn + 2)))
B = Application.WorksheetFunction.Min(ws6.Range(ws6.Cells(1, LastColumn + 4), ws6.Cells(LastRow, LastColumn + 4)))
C = Application.WorksheetFunction.Min(ws6.Range(ws6.Cells(1, LastColumn + 6), ws6.Cells(LastRow, LastColumn + 6)))
E = Application.WorksheetFunction.Min(ws6.Range(ws6.Cells(1, LastColumn + 8), ws6.Cells(LastRow, LastColumn + 8)))
F = Application.WorksheetFunction.Min(ws6.Range(ws6.Cells(1, LastColumn + 10), ws6.Cells(LastRow, LastColumn + 10)))

ws6.Cells(LastRow + 1, LastColumn + 1) = (A & B & C & E & F)

D = ws6.Cells(LastRow + 1, LastColumn + 1)
```

Appendix D: DCMD and RO Economic Anlaysis

Estimation of water production cost (WPC) using solar driven RO or a solar drive

This appendix presents simple economic analysis and the comparison of a solar driven DCMD system and a RO system. Due to the lack of established reports on the cost of DCMD system, both manufacture and long-term running cost, the cost estimation are mostly based on the cost provided in (Banat & Jwaired, 2008). Both the RO system and the DCMD system are expected to produce 500L of potable water per day.

(i) Systems used for study

The direct contact membrane distillation (DCMD) and reverse osmosis (RO) are compared one to the other. DCMD, known as an emerging membrane distillation technology, can use solar thermal energy and other waste heat as the driving force. Reverse osmosis (RO) is a traditional and widely used water purification technique that uses a semi-permeable layer and an applied pressure to let water molecules pass through. RO uses electricity to drive the plant, and can be coupled with the photovoltaic system to drive the pump.

For the comparison, solar thermal energy is used as the main energy source for DCMD. This also implies there are certain assumptions for the comparison of the two water desalination techniques. For the reverse osmosis analysis, it has been assumed that the solar-powered reverse osmosis systems do not include any energy storage equipment and hence would only operate when the solar power is available. Moreover, high-pressure pumps are used for the reverse osmosis process.

(ii) RO system modelling

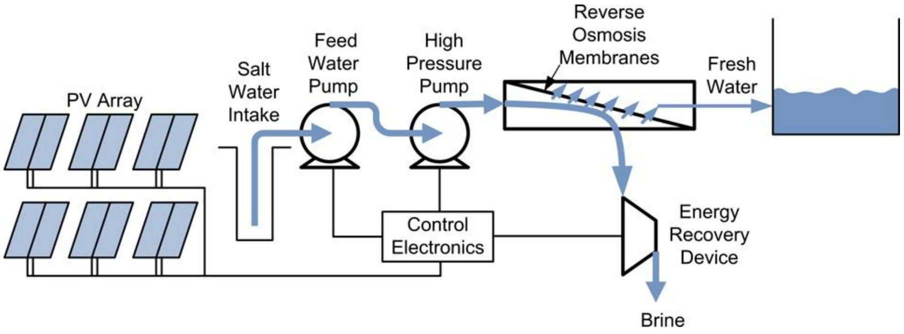

Figure D1 An outline of the reverse osmosis system, adopted from (Bilton, et al., 2011)

For the reverse osmosis (RO) system, Figure D1 shows schematically the whole process. The photovoltaic cells are used as the running power and incur cost to the system. The solar energy powers the feed pumps to process the reverse osmosis (RO). While fresh water is collected on one side of the membrane, concentrated salt is left on the other side. Then the concentrated brine is passed through a turbine to recover some of its energy before it leaves the system. In this case, the concentrated brine passes through the system only once.

Cost Calculation of RO

The permeate collection rate is expected to be 62.5L/hr for an eight-hour working per day to achieve 500L/day. In order to calculate the total cost of the system over three given operation period: 10-year, 5-year and 2-year, the cost of production has been divided into three parts including the capital, operating and the maintenance cost. The cost of desalination is then presented in Tables 3.1 to 3.4, listing as a function of facilities, energy cost on top of the salvage value, interest rate and payback period, which is the method used in (Goosen, et al., 2000), as shown below. The final measure is per unit price of water per m^3.

Actual annual cost

The total cost of desalination system, a function of actual annual cost and can be expressed as:

Actual annual cost (AC) = the first annual cost (M) - Salvage value (N) + operating cost (AMC)

If P is the capital cost of the system and CRF is the capital recovery factor, the first annual cost of system, M can be determined as

M = P x CRF

With,

$$\text{CRF} = \frac{r(1+r)^n}{(1+r)^n - 1}$$

Where r is the interest rate of the lending bank and n is the life of the system (in years), assumed there is no loss of efficiency.

Salvage value

The salvage value (S) of the system is the market value at the end of the lifetime of the plant. This was assumed to be 20% of the usable material cost. Hence the annual salvage value (N) can be expressed as

N = S x SFF

Where SFF is the sinking funding factor

$$\text{SFF} = \frac{r}{(1+r)^n - 1}$$

Operational costs

In order to maintain a smooth and continuous progress of the desalination system, a certain amount needs to be allocated into the replacement of the worn out parts. The annual operating and maintenance cost (AMC), known as the total yearly costs of owning and operating the desalination unit, also include the amortization or fixed charges, operation and maintenance and parts replacement cost. Thus, a fixed percentage of the first annual cost (M) has been considered. *For this analysis, the operational and maintenance cost has been assumed to be 5% of the initial capital costs for DCMD and 10% of the initial capital cost for RO (due to membrane module replacements required).*

Cost of photovoltaic power system

The cost of the photovoltaic power system including the control electronics, wiring, supporting structure and installations can be estimated by its historical pricing of £6.00 per watt. Therefore for our system running at 1.5kW, the capital cost of the solar panels can be estimated as £9,000.

Cost of reverse osmosis unit

For this cost analysis, a commercial available reverse osmosis unit that is able to produce drinking water at a small scale has been considered. The unit cost of this rig is estimated at £1,980, which has an average deliverance of 500L per day (Shenzhen Youber Technology Co., Ltd, 無日期), and according to the production information the system operates at 60 bar. Table D1-3 presents the annual cost estimated based on different length period of operation time.

Table D1 Annual cost of reverse osmosis based on a 10-year operation

Parameter	Value

Plant capacity	500L day^{-1}
Operating pressure	60 bar
Plant lifetime	10 years
Interest rate, r (Average bank rate)	5%
Capital recovery factor (CRF)	0.1295
The first annual cost, M	£1400
Sinking funding factor (SFF)	0.0795
Annual salvage value, N	£180
Operating costs, AMC	£140
Actual annual cost, AC	£**1400**
Cost of water/m^3	£**8 m^{-3}**

Table D2 Annual cost of reverse osmosis based on a 5-year operation

Parameter	Value
Plant capacity	500L day^{-1}
Operating pressure	60 bar
Plant lifetime	5 years
Interest rate, r (Average bank rate)	5%
Capital recovery factor (CRF)	0.2310
The first annual cost, M	£2500
Sinking funding factor (SFF)	0.1810
Annual salvage value, N	£400
Operating costs, AMC	£250
Actual annual cost, AC	£**2300**
Cost of water/m^3	£**13 m^{-3}**

Table D3 Annual cost of reverse osmosis based on a 2-year operation

Parameter	Value
Plant capacity	500L day^{-1}
Operating pressure	60 bar
Plant lifetime	2 years
Interest rate, r (Average bank rate)	5%
Capital recovery factor (CRF)	0.5378
The first annual cost, M	£6000
Sinking funding factor (SFF)	0.4878
Annual salvage value, N	£1100
Operating costs, AMC	£600
Actual annual cost, AC	£**5400**
Cost of water/m^3	£**30 m^{-3}**

(iii) WPC using a solar driven DCMD

As depicted in chart shown in Figure D2, the WPC of a DCMD system encompassed three major areas.

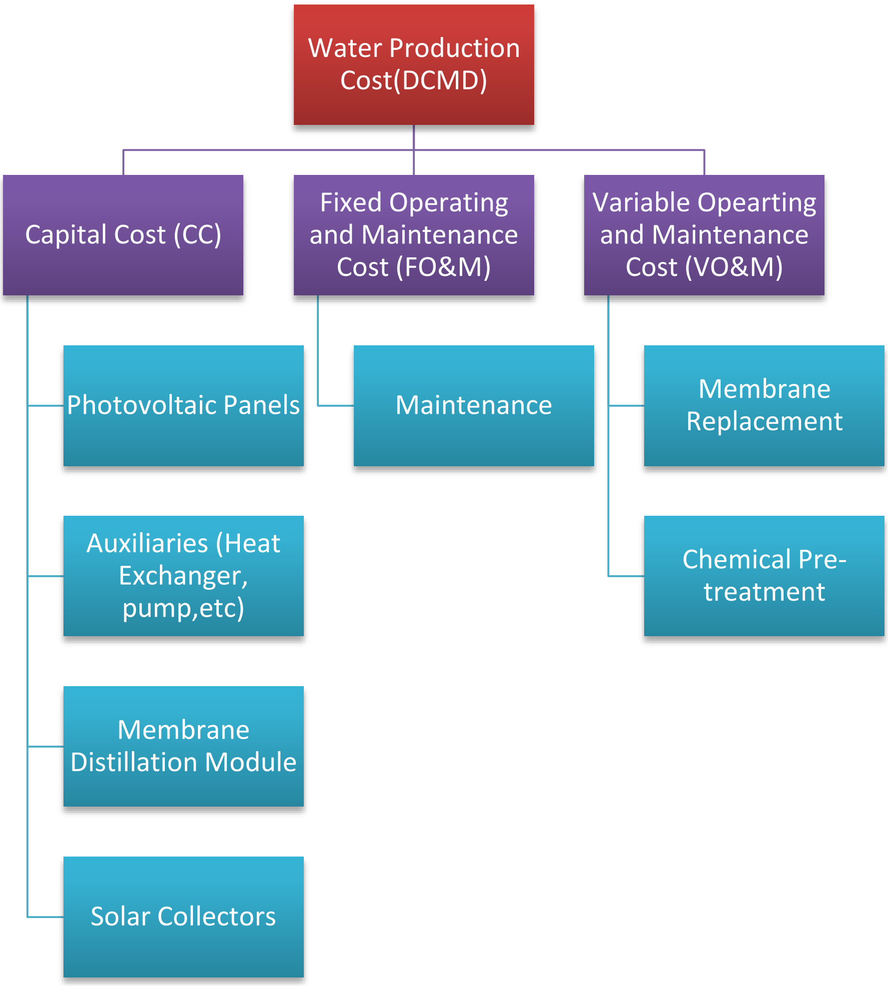

Figure D2 Chart showing the WPC breakdown of a DCMD system, adopted from (Saffarini, et al., 2012).

The capital cost included purchasing equipment and installation. Using the cost reported in (Banat & Jwaired, 2008), the equipment included the flat plate solar collector, which has a basic cost estimated at 18.5W/m^2 with an additional cost for the solar racks. The photovoltaic cell has a cost of approximately £3.2 per Watts of energy required. The membrane module cost is estimated at £23/m^2 of membrane area[8]. For this study of the membrane distillation, the membrane area evaluated in Chapter 6 is used.

Table D4: Cost requirement for DCMD unit

Equipment	**Requirement**	**Unit Price (£)**	**Total Cost (£)[9]**
Membrane module	8.33 m^2	23/m^2	200
Solar collector	30 m^2	67/m^2	2,000
PV modules	530 W	3.2/W	1,700
Pumps		200	950
Piping and tank		130	650
Membrane assembly	Estimated need and cost according to (Banat & Jwaired, 2008)		400
Solar collector rack			950
Heat exchangers			950
Sensors and controls			1,300
Total equipment costs			8,000
Instrumentation and control cost	25% of the total equipment costs		2,000
Installation cost			2,000
Total investment			12,000

The total investment is approximately £12,000, as shown in Table D4. The actual annual cost and the cost per m^3 are used as the measure of the cost and then calculated and presents in Tables D5-7 with respect to three operating periods.

---

[8] **In Banat and Jwaied's study, spiral air gap membrane module was used. For our analysis, we have made the assumption that the membrane cost is similar for hollow fibre and spiral membrane module.**

[9] **It is estimated to the closest £50.**

And the actual annual cost is given by:

Actual annual cost (AC) = the first annual cost (M) + Membrane replacement cost (MRC)- Salvage value (N) + operating cost (AMC); which MRC is approximates to 20% of the membrane cost.

Table D5: Annual cost of DCMD module based on a 10-year operation.

Parameter	Value
Plant capacity	500 L day^{-1}
Plant lifetime	10 years
Interest rate, r (Average bank rate)	5%
Capital recovery factor (CRF)	0.1295
The first annual cost, M	£1,600
Membrane replacement cost, MRC	£40.43
Sinking funding factor (SFF)	0.0795
Annual salvage value, N	£200
Annual operating costs, AMC	£300
Actual annual cost, AC	£2,800
Cost of water	£10 m^{-3}

Table D6: Annual cost of DCMD module based on a 5-year operation.

Parameter	Value
Plant capacity	500 L day^{-1}
Plant lifetime	5 years
Capital recovery factor (CRF)	0.2310
Interest rate, r (Average bank rate)	5%
Sinking funding factor (SFF)	0.1810
The first annual cost, M	£2,800
Membrane replacement cost	£40
Annual salvage value, N	£450
Annual operating costs, AMC	£550
Actual annual cost, AC	£3000
Cost of water	£18 m^{-3}

Table D7: Annual cost of DCMD module based on a 2-year operation.

Parameter	Value
Plant capacity	500 L day^{-1}
Plant lifetime	2 years
Interest rate, r (Average bank rate)	5%
Capital recovery factor (CRF)	0.5378
Sinking funding factor (SFF)	0.4878
The first annual cost, M	£6,500
Membrane replacement cost	£40
Annual salvage value, N	£1,200
Annual operating costs, AMC	£1300
Actual annual cost, AC	£6,500
Cost of water	£40 m^{-3}

(iv) Discussion

According to the calculations, it can be observed that the water costs of DCMD module are nearly 30% more than the cost of PV driven reverse osmosis (RO) for each operation period, mainly due to the cost of solar panels which currently is still relatively expensive. Depending on the development of solar energy technology, both the cost of PV-RO and solar thermal DCMD can be expected to reduce as the technology improves. Moreover, the cost of brine disposal is not included for the cost estimations of both systems. Depending on the brine concentration and disposal method, the cost of disposal could offset the WPC calculated considerably.

Appendix E: Publications from this work

Published Journal Articles:

Field, R. W., **Wu, H. Y**. & Wu, J. J., 2013. Multiscale modeling of membrane distillation: some theoretical considersations. *Industrial & Engineering Chemistry Research,* 52(26), pp. 8822-8828.

Wu, H. Y ., Wang R. & Field, R. W., 2014. Direct contact membrane distillation: An experimental and analytical investigation of the effect of membrane thickness upon transmembrane flux. *Journ. Mem. Sci,450,* pp. 257-265.

Wu, H. Y ., Tay M. & Field, R. W., Novel method for the design and assessment of direct contact membrane. *Journ. Mem. Sci, 514, pp. 260-269.*

Pending Publications:

Wu, H. Y .& Field, R. W., 2014. Modelling and implementation of DCMD for small-scale desalination in arid region [To be submitted]

Conference presentations:

Poster:

Wu, H. Y., Hu, J. & Field, R., 2012. Membranes for drinking water production: The role of membrane processes in localised small scale desalination systems coupled directly with solar energy. London, Euromembrane 2012.

Wu, H. Y., & Field, R., 2013. The effect of membrane thickness and salinity upon membrane flux and thermal efficiency for sinple co-current and counter-current flows: a comparison of a theoretical analysis with modelling results, Sitges, 1st Conference in membrane desalination.

Wu, H. Y., Field, R. & Hu J., 2014. Cost and energy comparison of reverse osmosis and direct contact membrane distillation for small scale localized desalination. Suzhou, ICOM2014.

Oral:

Wu, H. Y., & Field, R., 2013. The influence of module layout upon performance: a comparison of counter and cross flow designs for various lengths of modules, Sitges, 1st Conference in membrane desalination.

Wu, H. Y., & Field, R., 2014. Optimized hollow fibre membrane module design for direct contact membrane distillation. Suzhou, ICOM2014.